Technische Universität München
Physik Department
Theoretische Physik T37

Dissertation

Water: Structure, Dynamics and Solvation

Felix Sedlmeier

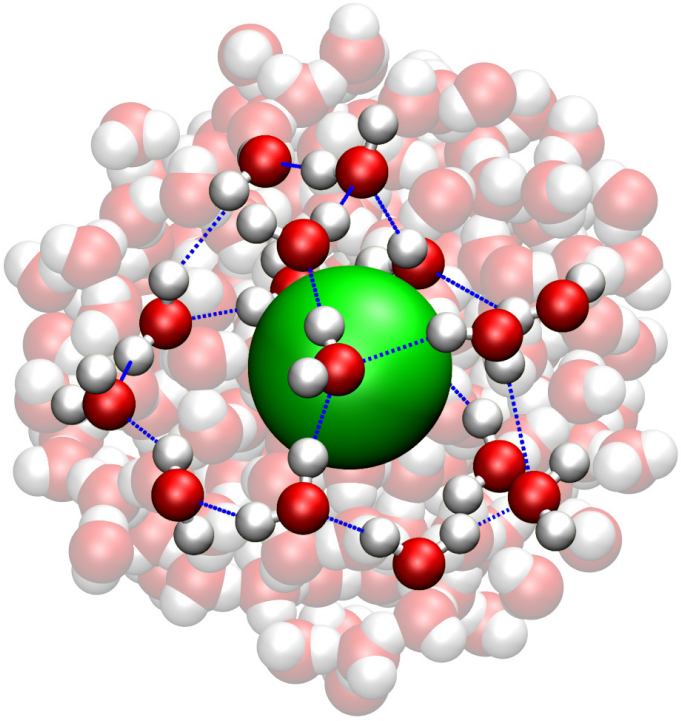

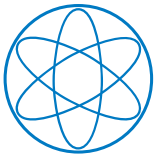

Technische Universität München

Physik Department

Theoretische Physik T37

Water: Structure, Dynamics and Solvation

Dipl.-Phys. (Univ.)

Felix Sedlmeier

Vollständiger Abdruck der von der Fakultät für Physik der Technischen Universität München zur Erlangung des akademischen Grades eines

Doktors der Naturwissenschaften (Dr. rer. nat.)

genehmigten Dissertation.

Vorsitzender:		Univ.-Prof. Dr. Thorsten Hugel
Prüfer der Dissertation:	1.	Univ.-Prof. Dr. Roland Netz, Freie Universität Berlin
	2.	Univ.-Prof. Dr. Martin Zacharias

Die Dissertation wurde am 22.11.2011 bei der Technischen Universität München eingereicht und durch die Fakultät für Physik am 15.12.2011 angenommen.

The most incomprehensible thing about the world is that it is comprehensible.

Albert Einstein (1879 – 1955)

ABSTRACT

In recent years it has become clear that water has a much more significant function in biological processes on the nano scale than it was assumed previously. Especially hydrophobic effects play an important role in aggregation processes and protein folding. It is the goal of this work to gain a thorough understanding of the behavior of water near curved interfaces by the use of molecular dynamics simulation methods. As a prerequisite, in a first step, structural correlations in bulk water are investigated. By studying solvation processes and fluctuations of air/water interfaces we succeed in further clarifying the role of the hydrophobic effect in protein folding and develop a consistent description of hydrophobic solvation over several length scales. Furthermore, we describe the dynamics of water molecules near interfaces by means of stochastic methods.

In den letzten Jahren hat sich die Erkenntnis durchgesetzt, dass Wasser eine sehr viel bedeutendere Funktion in biologischen Prozessen auf der Nanoskala hat, als bisher angenommen. Vor allem hydrophobe Effekte spielen eine entscheidende Rolle für Aggregationsvorgänge und die Proteinfaltung. Das Ziel dieser Arbeit ist es, durch den Einsatz von Molekulardynamik Simulationen, ein umfassendes Verständnis des Verhaltens von Wasser an gekrümmten Grenzflächen zu erlangen. Als Grundlage dafür werden in einem ersten Schritt strukturelle Korrelationen in purem Wasser untersucht. Durch das Studium von Solvationsprozessen und der Fluktuationen an Luft/Wasser Grenzflächen, gelingt es die Rolle des hydrophoben Effekts für die Proteinfaltung weiter zu klären und eine skalenübergreifende Beschreibung hydrophober Solvation zu entwickeln. Des weiteren wird die Dynamik von Wassermolekülen an Grenzflächen mittels stochastischer Methoden beschrieben.

CONTENTS

CHAPTER 1

INTRODUCTION AND OUTLINE

Water was the matrix of the world and of all its creatures ... Just as the noblest and most delicate colors arise from this black, foul earth, so various creatures sprang forth from the primordial substance that was only formless filth in the beginning. Behold the element of water in its undifferentiated state! And then see how all the metals, all the stones, all the glittering rubies, shining carbuncles, crystals, gold, and silver are derived from it; who could have recognized all these things in water ?

Paracelsus (1493 – 1541)

Water is without doubt the most essential liquid on earth. More than 70% of our planet's surface is covered by oceans. Deep sea currents and water vapour in the athmosphere determine our climate. The hydrological cycle provides the land with rain. Rivers and glaciers shape the surface of the earth.

But most importantly, water is the "matrix" of life [10, 11]. Although it is debated if water is unique in its function as the "universal solvent of life" or if it is just one of many possible candidates, happening to be abundant on earth, it is doubtless essential for life as we know it. On average 60% of the body weight of a human are due to water [12], and most life sustaining processes require its presence. Water is not only the solvent, in which most biochemical processes take place, but also plays an important role in many metabolic reactions in the body [10].

The importance of water for all aspects of our life has also had its impact on our culture and society. Aristotle named water one of his four elements beside earth, fire and air and in all major religions water plays a key role in ceremonial rituals, symbolizing purification and rebirth. Not surprisingly, water is also one of the most

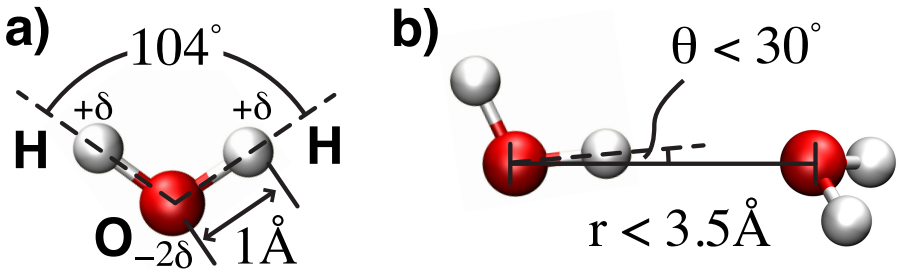

Figure 1.1.: Illustration of the geometry of (a) the water molecule and (b) the hydrogen bond.

studied liquids, the web of science lists more than 300 000 publications containing the key word water only in 2010. Still, many of its properties are not yet well understood.

Although the necessity of the presence of water for biological life has been recognized a long time ago, our understanding of its role has changed drastically in the last decades. While water was long considered merely as the background in front of which the biomolecular machinery worked, even computer simulations of biomolecules used to be performed in vacuum rather than in water, it becomes more and more clear that water has a more significant and active part in these processes [13]. Understanding of the role that water plays in biomolecular processes is therefore one of the prerequisites to understanding these processes themselves.

Water is not only the most important, but also one of the most extraordinary liquids known. Water is the only inorganic substance that appears naturally in its liquid form and also the only substance on earth that is naturally found in its solid, liquid and gaseous state. Furthermore, water shows anomalies in almost all of its thermodynamic and transport properties, most prominent among these the anomaly in the density, showing a maximum at a temperature of 4° C [14] in contrast to the monotonous increase of density with decreasing temperature that most liquids exhibit.

All these extraordinary properties of water can be traced back to its molecular structure and with it its ability to form hydrogen bonds (see Fig. 1.1). The water molecule is formed by two hydrogen atoms that are both bound to one oxygen atom forming an angle of about $\angle(HOH) \approx 104°$, close to the tetrahedral angle, while the OH bond length is roughly 1 Å [15]. Since the oxygen atom has a much higher electronegativity than the hydrogen atoms, it tends to draw their electron density towards itself, leaving the hydrogen atoms with a positive and the oxygen atom with a negative partial charge. Together with the small size of the water molecule, this allows for a very strong interaction between the hydrogen atom of one water molecule and the oxygen atom of an adjacent molecule, which is commonly referred to as a hydrogen bond (HB). The binding energy of a HB is roughly 25 kJ/mol which equals $\approx 10\ k_B T$ at ambient temperatures [16], much stronger than other intermolecular interactions, but it is also highly directional, losing much of its strength if the angle between the OH bond of the donor molecule with the line connecting the oxygen atoms becomes larger than $\approx 30°$. It is these two properties, that largely account for the structural properties of water.

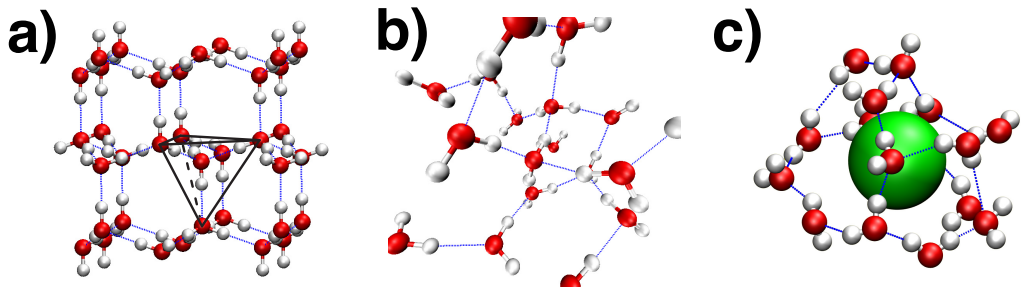

Figure 1.2.: Illustration of the hydrogen bond network (a) in hexagonal ice, (b) in liquid water and (c) around a hydrophobic solute. Hydrogen bonds are indicated by dashed blue lines.

In ice[1], each water molecule is surrounded by four other molecules at the edges of a regular tetrahedron forming the maximally possible four hydrogen bonds (see Fig. 1.2 a). Although in liquid water the structure is much more irregular and no long-range order is present, the local tetrahedral coordination is preserved to a high degree [17, 18] and at ambient conditions, on average ≈ 3.5 out of the four possible hydrogen bonds are maintained [19] (see Fig. 1.2 b). This hydrogen bonding network is at the origin of most of the anomalous properties of water and also the key to their understanding.

But there are still many open questions. Recently, it has been suggested, that the water structure at ambient conditions is governed by a competition of two distinct water species differing in the degree of tetrahedral ordering and density, which form clusters with a size of ≈ 1 nm [20]. This idea goes back to the hypothesis of water possessing a second critical point marking the end of a first order phase transition between one more and one less ordered liquid species [21] as a possible explanation for its thermodynamic anomalies. Although this suggestion has been controversially discussed in the literature [22, 23], it raises the question how strong correlations in the degree of tetrahedral ordering in liquid water are, and how far they persist. This question is especially relevant in light of the discussion about a structuring effect of small solutes as discussed below. We address this question in the first part of our work by determining spatial self- and cross-correlation functions of the density and several structural order parameters in water at ambient conditions.

1.1. Water at interfaces: Hydrophobicity and curvature effects

As in the bulk phase, the behavior of water near aqueous interfaces is largely dominated by its tendency to form hydrogen bonds or rather by the constraints the intro-

[1] to be precise, the four-coordinated tetrahedral structure is found in ice Ih, the hexagonal state of ice which forms at ambient pressures [10]

duction of a surface puts on the formation of a hydrogen bond network. This depends of course on the chemical nature of the substrate.

The interactions between a hydrophobic surface and water are non-specific and much weaker than the water-water interaction, so that the water attempts to minimize the contact area by forming a large contact angle [24–26]. Also, the water molecules in the layers adjacent to the surface orient themselves in a way reminiscent of the orientational structure in hexagonal ice in order to minimize the number of hydrogen bonds that are broken [9, 27]. This effect should, however, not be taken as evidence for the formation of an 'ice-like' layer near the surface, since the total entropy increases when a hydrophobic interface is created, which is evident from the decrease of the interfacial tension with increasing temperature [15]. Further characteristics of a hydrophobic surface are the formation of a depletion layer [6, 28–32] and the occurrence of slip in hydrodynamic flows [33, 34] as will be discussed in more detail below. It shall be noted, that in this sense an air/water interface should be viewed as a perfectly hydrophobic interface, i. e., the limiting case for completely vanishing surface water interaction.

At hydrophilic surfaces, that possess polar groups with which the water can form hydrogen bonds, the water structure is still perturbed by the presence of the interface but wholly different phenomena occur. For instance, two hydrophilic surfaces repel each other [35–37], the so called phenomenon of hydration repulsion, while two hydrophobic surfaces are drawn together [38, 39].

The situation changes completely if we go from extended surfaces to the solvation of small solutes, that confront the aqueous phase with a highly curved interface. While the hydrogen bond network has to be broken at an extended hydrophobic interface, small hydrophobic molecules can be accommodated without breaking hydrogen bonds at the cost of a slight rearrangement of the network (see Fig. 1.2 c). This manifests itself in a crossover from a large scale solvation or extended interface regime to a small scale solvation regime that can be seen in many characteristic properties[40, 41]. While the cost of the creation of an extended interface or the solvation of a large solute scales with its surface area, the solvation free energy for smaller solutes scales with the solute's volume [42]. At ambient temperatures the solvation entropy of small solutes is negative, while for large solutes and extended surfaces it is positive [43, 44]. In short, on the nano scale most interfacial properties attain a distinctive curvature dependence. Furthermore, hydrophobic solutes tend to aggregate in water, the mechanism of which is still debated but supposedly also depends on the involved length scales [40, 45].

All these phenomena taken together make up the famous "hydrophobic effect" [46], which is at the bottom of many aggregation and solvation processes spanning a wide range of length scales from the solubility of rare gas solutes [47–49], over molecular recognition [50, 51] and amphiphilic aggregation processes [52] to protein folding [53] and misfolding [54, 55]. Since Kauzmann [56] first suggested that the burial of hydrophobic residues in the protein interior away from the water could be a driving force for protein folding, the hydrophobic effect is believed to play a dominant role in protein structure and stability, for reviews see e. g. [45, 53]. On the other

hand misfolding and the subsequent aggregation of globular proteins to form amyloid structures is at the origin of many diseases such as Alzheimer's and Parkinson's [54].

Despite the importance of the hydrophobic effect its mechanism is still debated and a consistent description over the different regimes is missing. Frank and Evans [57] explained the negative entropy and enthalpy of solvation of small hydrophobes in their 'ice-berg' model by the formation of a layer of structured water with enhanced hydrogen bonds around the solute, reminiscent of the crystalline clathrate hydrates that can form under high pressures [58]. Building on this, Kauzmann [56] suggested, that the aggregation of two hydrophobes is facilitated by the release of the structured water in between the solutes which is accompanied by an increase of entropy. Stillinger on the other hand attributed the hydrophobic aggregation to the clumping tendency of ordered structures and draws an analogy to the thermodynamic anomalies in supercooled water [16, 59]. Although the 'ice-berg' view has been adopted by many authors, the character of the water in the solvation shell is a matter of debate. Blokzijl and Engberts [45] argue, that the assumption of a crystalline-like structure with enhanced hydrogen bonding is not necessary to explain the favorable enthalpy of solvation, which they attribute to van der Waals interaction between water and solutes. The structure of the hydrogen bonding network around the solutes is merely maintained tolerating the orientational constrains put up by the solute, while the aggregation of solutes is a consequence of the limited capacity to accommodate hydrophobic solutes.

It has been argued, that the hydrophobic effect should rather be defined by its unusual temperature dependence [46, 60] and any explanation of its mechanism must account for it instead of the solvation entropy at ambient temperature. Indeed, the solvation entropy of hydrophobic solutes increases rapidly with increasing temperature and even changes its sign due to the large and positive heat capacity change upon solvation. Extrapolating the solvation entropies and enthalpies for several small hydrophobic solutes, it has been noted that they converge at a universal temperatures [61], which seems to indicate that hydrophobic solvation is dominated by universal water features and not so much by solute specifics [62, 63]. The reported convergence of the denaturing entropy of a group of different proteins at roughly the same temperature as hydrophobic solutes [64, 65] was consequently argued to indicate that the denaturing entropy of proteins is dominated by the hydrophobic effect and used to estimate the hydrophobic contribution to protein stability [66–68]. However, this appealing picture was subsequently questioned since the initially claimed universal convergence of denaturing entropies holds only for a small subset of proteins, for a larger data collection no convergence is seen [69], which can still not be satisfactorily explained. We argue, based on the study of solvation of small hydrophobic solutes with varying solute water interactions, that the differences induced by variations in the residue-water interactions are sufficient to explain these effects.

Besides its temperature dependence, the size dependence is maybe the most striking characteristic of hydrophobic solvation. The crossover between the small scale and the large scale solvation regime, happens on a length scale on the order of ≈ 0.5 nm [41], which makes it especially relevant for protein folding and molecular aggregation [70].

Theoretical descriptions based on the assumption of Gaussian density fluctuations on small length scales give a reasonable description of the small solute regime [71–75], while interfacial thermodynamics are employed to account for large solutes [76]. But even for solutes smaller than 0.5 nm, proportionality of the solvation free energy and the solvent accessible surface of the solute with varying effective proportionality constants is often reported, see e. g. Ref. [77], a common misconception which has its origin in the fact that for molecules made up from similar building blocks, like alkane chains, due to additivity the solutes surface area as well as its volume are proportional to the chain length [41, 78].

A description spanning both regimes might be obtained by the introduction of a curvature dependent surface tension, a concept which has been first proposed by Tolman [79] in 1949 in the context of liquid droplets. However, not even for simple liquids a consensus has been reached about the sign of the coefficient to the first order curvature correction, usually termed the Tolman length, see e. g. [80, 81] and references therein. Scaled particle theories try to bridge the gap between the two regimes by constructing a sophisticated interpolation function including curvature correction terms [43, 82–85]. While most of the studies mentioned so far deal with spherical solutes, there is evidence that hydrophobic hydration is not only sensitive to the size but to the shape of a solute as well [86–88].

This could be taken into account by a more general description of the surface free energetics in terms of a curvature based free energy functional like the one proposed by Helfrich [89]. Such a description involves additional parameters, whose determination provides a formidable challenge, see [90–92] and references therein. We demonstrate that progress can be made by studying simultaneously the solvation of spherical and cylindrical solutes, which allows for the extraction of the elastic properties of the aqueous interface.

Instead of studying water interfaces curved due to the presence of a solute, one can also take a complementary approach and study the shape fluctuations of a free liquid/vapor interface, where curvature corrections manifest themselves in a wave vector dependent effective surface tension [92–94]. Experimentally interfacial fluctuations can be studied by small angle X-ray scattering techniques [95–97]. Restrictions in the accessible wave vector range and accuracy and the entanglement of interfacial and bulk fluctuations make the interpretation of such experiments difficult [91, 98–100]. The complete configurational knowledge in a computer simulation, on the other hand, allows for the disentanglement of these effects and leads to a consistent description of the surface energetics, as we demonstrate in this work.

1.2. Water dynamics: The hydrogen bond dance

As well as the static properties, also the dynamic properties of many processes in aqueous solution are closely related to the dynamics of the water itself. Examples include the kinetics of protein folding [101, 102], ion pair dissociation [103] or the

water permeation through membrane channels [104]. Also the boundary conditions of hydrodynamic flows are determined by the dynamics of the interfacial water [105, 106] with important implications for microfluidic devices [107].

The water dynamics in turn is governed by the fluctuations and rearrangements of the hydrogen bonding network through the breakage and formation of individual hydrogen bonds. Stillinger [16] suggested, that the dominant process is what he called switching-of-allegiance, that is the substitution of one hydrogen bond acceptor with another near at hand, a view which is supported by the work of Csajka and Chandler [108]. Laage and Hynes [109, 110] note that this switching occurs in a rather abrupt manner including angular jumps of the hydrogen bond donor. The non-exponential kinetics of the hydrogen bond relaxation [111, 112] is attributed to a coupling with diffusion by Luzar and Chandler [113].

Near interfaces, the dynamics of the water are influenced by the chemical character of the surface. At hydrophobic surfaces the lateral motion of the water is not so strongly perturbed by the weak substrate water interactions, which leads to the phenomenon of surface slip [105, 106], that is in hydrodynamic flows the water keeps a finite velocity relative to the substrate, an effect which is closely linked to the occurrence of a depletion layer [33, 34]. Near hydrophilic surfaces on the other hand the well known no-slip boundary condition holds, that is the water layers adjacent to the surface do not show a relative velocity.

Simulation studies report a slowing down of water diffusion both at hydrophobic [34, 114, 115] and hydrophilic surfaces [34, 114, 116], which is much stronger at hydrophilic surfaces. Some studies of water in thin films on hydrophilic surfaces [117, 118] and in confinement by hydrophilic walls at nanometer separation [119–121] even report the formation of 'ice-like' layers in conjunction with a viscosity increase of several orders of magnitude, while others find a moderate increase of the viscosity by a factor on the order of 4 [34]. A quantitative comparison is difficult, however, since most of the methods used to determine the dynamics involve an averaging over a certain distance from the surface that might obscure fast variations [34, 117]. Also the entanglement of effects due to the free energy profile imposed by the substrate and the diffusivity require a more careful analysis, as has been recently demonstrated for a system of hard spheres in confinement [122]. In this work we apply a similar method to the dynamics of water near hydrophobic and hydrophilic walls and solutes.

1.3. Outline of this work

It is the goal of this work to gain a thorough understanding and a consistent description of the thermodynamics and dynamics of water near curved and planar interfaces by the use of molecular dynamics simulation methods.

In chapter 2 we describe the computational and analysis methods used in this work as far as relevant for the overall work. More specific analysis tools are described in

the individual chapters if it is necessary. We also discuss the general properties of the water models employed and the modeling of surfaces and solutes.

In chapter 3 we investigate several structural properties of bulk water. As a stringent test of the quality of the water models used, we determine the low wave vector region of the static structure factor and compare the results with experimental data. It turns out, that all investigated water models can reproduce the experimental data reasonably well, including subtle features such as the slight minimum observed around wave vectors of $q \approx 4\,\mathrm{nm}^{-1}$ [23, 123, 124] and are consequently well suited to investigate water structure. Subsequently, we calculate spatial self- and cross correlation functions of the density and structural order parameters such as the hydrogen bond number and the tetrahedrality parameter introduced by Errington and Debenedetti [125] and show that there is no strong coupling between density and structural fluctuations.

In chapters 4 and 5 we turn to the description of hydrophobic solvation effects. While chapter 4 is mainly concerned with the solvation of small scale solutes and its dependence on the solute water interaction, chapter 5 deals with the crossover between the small scale and large scale solvation regime and a consistent description based on a local surface free energy functional.

By determining the thermodynamic solvation properties for idealized hydrophobic solutes with varying solute water interactions over a wide range of temperatures, we show in chapter 4 that the temperature at which entropy and enthalpy converge depends sensitively on the specific features of the interaction potentials. We further explain the differences in the solvation thermodynamics for different water models and the discrepancies with previous studies [72] using hard sphere models. Finally, we discuss the implications for the interpretation of the hydrophobic contribution to protein stability.

In chapter 5 we investigate, how the Helfrich [89] free energy functional can give a consistent description of the free energy of a curved water interface. In the first part (Sec. 5.2) we extract the bending rigidity by analyzing fluctuation spectra of the free air/water interface. For this purpose we introduce a method to separate bulk and interfacial fluctuations without any fitting parameters. We also determine the intrinsic density profile and discuss implications for the interpretation of scattering experiments. In the second part (Sec. 5.3) we study the solvation of hydrophobic spheres and cylinders with radii up to 2 nm. We determine solvation free energies, entropies and enthalpies which enables us to identify the relevant crossover length scales and discuss implications for hydrophobic aggregation. Applying the Helfrich functional simultaneously to the solvation free energies of solutes with different geometries allows us to extract the surface elastic constants, including the coefficient of the first order correction, i. e., the Tolman length, which is not accessible by analyzing surface fluctuations.

In chapter 6 we apply a Fokker-Planck based stochastic formalism to describe the dynamics of single water molecules near hydrophobic and hydrophilic solutes and interfaces. This formalism allows us to disentangle the free energy and diffusivity profiles of the dynamic processes. We find that the diffusivity profiles show strong variations

including a dramatic drop near the hydrophilic surface as well as near another water molecule, whereas the drop near hydrophobic surface and solute is rather moderate.

Finally, we give a summary of our results and discuss implications and possible starting points for future work.

CHAPTER 2

COMPUTATIONAL METHODS AND MODELING

Since the relevant length scales we are interested in are in the nanometer regime, a naive application of the concepts from continuum theories is bound to fail at some point. Rather, modeling on the molecular scale is necessary. On the one hand this gives direct access to structural properties on the atomistic scale, on the other hand it is the basis for a description on a meso- or macroscopic scale, e. g. by the introduction of suitable corrections to continuum theories.

In principle, statistical mechanics provides the framework to derive physical observables from the microscopic properties of a system, that is its Hamiltonian. In practice, however, exact solutions exist only for few special cases and in general approximations have to be made. Density functional and integral equation theories yield good results for simple liquids, that is atomic liquids with pairwise additive interactions. The complex structure of the water molecule and the coexistence of long and short ranged interactions make an analytical treatment of liquid water very difficult.

That is where numerical simulations techniques like Monte Carlo and Molecular Dynamics can step in. Based on the interaction model put in, a simulation yields exact results, their statistical accuracy, however, limited by the computational resources available. Simulations therefore serve a twofold purpose. On the one hand they can be used to verify theoretical results, on the other hand, they can tackle problems eluding theoretical treatment altogether, provided the underlying models have been thoroughly tested. In that way, simulations can also give input to higher level theories, whose parameters are hard to derive from a more fundamental treatment.

2.1. Molecular dynamics simulations

For the present study, we chose to employ the molecular dynamics (MD) method, since, in contrast to Monte Carlo simulations, it is suitable for the investigation of dynamic as well as static properties [126, 127]. In MD simulations one numerically integrates Newton's equations of motion for a system of interest in order to obtain a

trajectory of the system. Such a trajectory does not follow the exact time evolution of the system for the given starting conditions over the time scales of the simulation but there is much evidence that the generated trajectory is always close to a true trajectory for a time scale that is much longer than the time the Lyapunov instability takes to develop [128, 129]. Since one is usually only interested in statistical averages over an ensemble of trajectories, or equivalently a time average over a long trajectory, the results obtained from an MD simulation are representative of a true trajectory in phase space.

At the center of any molecular dynamics technique is of course the question of how to describe the interatomic interactions that enter into the equations of motion. Since we are dealing with molecular systems, these interactions are of quantum mechanical nature. However, even approximate quantum mechanical treatments [130] as e. g. in the Car-Parinello MD method [131] are computationally expensive and the system sizes and time scales that can be reached with reasonable effort are still to small for many applications. In classical MD simulations, as we will employ throughout this work, one therefore uses effective pairwise interaction potentials, whose parameters and functional forms are either derived from first principles methods or are optimized to reproduce experimental observables. Bonded interactions are typically modeled by harmonic bond and angle potentials and empirical torsion potentials to yield the correct molecular geometry, while non-bonded interactions include electrostatic forces due to partial charges on polar molecules and dispersion interactions described by Lennard-Jones potentials. Since these are only effective interaction potentials much care has to be taken to validate their performance in each specific situation. A detailed description of the force fields used in this work is given below.

All MD simulations throughout this work are performed using the Gromacs simulation package [132, 133], which is well tested and optimized for computational efficiency. The equations of motion are integrated via a leap frog integrator with a time step of $\Delta t = 2$ fs.

While the integration of Newton's equation produces trajectories with constant total energy and therefore corresponds to a micro-canonical ensemble (NVE), it is often more suitable to use a canonical (NVT) or isobaric-isothermal ensemble (NPT) in order to compare to experimental situations or theoretical calculations. This can be accomplished by using a thermostat or barostat algorithm to keep the temperature or the pressure constant during a simulation [126]. Unless noted otherwise, we use a Berendsen weak coupling thermostat and barostat [134] for temperature and pressure control. The relaxation times are usually set to $\tau = 1.0\,\mathrm{ps}$ in production runs.

Simulation systems are contained in cubic or rectangular boxes. To avoid finite size and undesired surface effects at the box edges periodic boundary conditions are applied in all three dimensions. To reduce the computational cost, short-ranged, e. g. Lennard-Jones, interactions are truncated at a cutoff radius $r_c = 0.9$ nm, unless noted otherwise. Since the interaction potential decays $\propto r^{-6}$ such a simple cutoff suffices and its effects on the systems dynamics are negligible, except for very rare cases as demonstrated in [135]. The effects on the pressure tensor can be significant, how-

ever, which can lead to errors in NPT simulations. In homogeneous systems one can correct for these cutoff effects by an analytical correction applied to both energy and pressure [127]. The treatment of electrostatic forces requires more elaborate methods, since the Coulomb potential decays only as $\propto r^{-1}$ and a simple cutoff scheme would lead to severe artifacts. We use a variant of the Ewald summation technique, where the interaction is split up into a quickly varying short-ranged part and a slowly varying long-ranged part. While the short-ranged part can be calculated in real space by using a simple cutoff as for the Lennard-Jones interaction with a cutoff radius of $r_c = 0.9\,\mathrm{nm}$, the contribution of the long-ranged part is calculated by a Fourier summation in reciprocal space. In the so-called particle mesh Ewald variant [136, 137], that we use in our simulations, the partial charges are spread on a grid in order to be able to use the fast Fourier transform method for the summation. We apply tinfoil boundary conditions in all simulations.

Furthermore, all bonds involving hydrogen atoms are constrained using the LINCS [138] algorithm (in the substrates) or the analytic SETTLE algorithm [139] (in the water molecules). Due to these constraints high frequency modes are removed and a longer integration time step can be used.

2.2. Force fields and modeling

As discussed above the force fields, that define the interatomic interactions in a MD simulation, are of utmost importance and have to be chosen carefully. In the following section we describe in detail the interaction potentials and the solvent, solute and substrate models that are used in this work.

2.2.1. Water models

Since the first computer simulations of liquid water by Barker and Watts [140] and Rahman and Stillinger [141] a great number of water models has been proposed (for a review see e.g. [142, 143]). The majority of these models treats the interactions between two molecules by electrostatic and dispersion interactions and an electronic repulsion. The charge distribution of the molecule is usually modeled by point charges located at the positions of the oxygen and hydrogen atoms or on additional virtual sites. The electronic repulsion is typically modeled by an r^{-12}-term which is combined with the r^{-6}-dispersion term in a Lennard-Jones potential centered on the oxygen atom. In most cases the interaction parameters, that is the partial charges and the Lennard-Jones interaction parameters, are optimized in such a way that a certain set of experimental observables, e. g. the heat of vaporization, density, etc. at ambient conditions is reproduced. The geometry of the molecule is either rigid or flexible, in which case the intramolecular forces are treated by harmonic bond and angle potentials. Further refinements include the introduction of atomic polarizability to describe multi-body interactions [144].

However, with increasing complexity of the models also the computational cost increases and a thorough optimization in the high-dimensional parameter space is often not possible any more. Therefore, in this work we restrict ourselves to several simple rigid water models, that nonetheless haven proven to perform well in various situations. A detailed discussion of the relevant model properties and corresponding references is given in the individual chapters.

The SPC [145], SPC/E [146], TIP4P/2005 [147] and TIP5P [148] water models all have a rigid geometry with fixed point charges and a varying number of interaction sites. All of them have two positively charged hydrogen atoms and an oxygen atom on which the Lennard-Jones interaction is centered. They differ mainly in the placement of the negative charge. In the SPC and SPC/E water model the negative charge is placed on the oxygen atom, while in the TIP4P/2005 water model the negative charge is placed on an additional virtual site on the bisector of the HOH angle. In the TIP5P model the negative charge is placed on two virtual sites located on the edges of a slightly distorted tetrahedron, formed by the hydrogen atoms and two virtual sites.

While the geometry of the SPC water model was set to an OH bond length of $\overline{OH} = 0.1$ nm and a bond angle equal to the tetrahedral angle $\angle(HOH) = 109.47°$, the partial charge of the hydrogen atom $q_{\mathrm{H}} = 0.41$ e and the coefficient of the repulsive Lennard-Jones term were optimized to reproduce the heat of vaporization and the density of water at $T = 300$ K. Here, e denotes the unit charge. The SPC/E water model is a reparameterization of the SPC model with the same objectives but including a correction for the polarization self-energy of the water dipole which leads to a different hydrogen partial charge of $q_{\mathrm{H}} = 0.4238$ e. Despite its simplicity, the SPC/E water models yields good results and has become one of the most widely used water models [142, 143]. It represents a good compromise between accuracy and computational efficiency and due to its widespread use it allows easy comparison of our results with the literature. We therefore use it in most parts of this work. Simulations with the SPC water model are only included for comparison with previous works.

As two examples of more refined water models we also use the TIP4P/2005 and the TIP5P models. In addition to the density and heat of vaporization at ambient conditions, the TIP4P/2005 parameters were fit to reproduce the temperature of the density maximum at ambient pressure, the density of ice II at 123 K and 0 MPa and of ice V at 223 K and 530 MPa, and the range of stability temperatures of ice III at 300 MPa [147]. The TIP4P/2005 model gives a very good description of the temperature dependence of several thermodynamic properties of water, including the density, isothermal compressibilty and isobaric heat capacity [149]. The TIP5P model was developed with the goal of reproducing the water density over a wide range of temperatures and pressures while simultaneously recovering the water structure at ambient conditions by introducing an additional interactions site with respect to the TIP4P model [148].

2.2.2. Solutes

One objective of this work is to study the influence of solute size, shape and interaction potential on hydrophobic hydration. We therefore use a model of idealized, spherical hydrophobic particles interacting with the water by a very general interaction potential, which gives us the freedom to study the influence of potential features such as the stiffness of the repulsion and the role of attractive interactions on the solvation properties and vary its size independently. A suitable choice is the Buckingham double exponential potential of the form

$$U_{\mathrm{SPH-OW}}(r) = A\,e^{-B(r-R)} - C\,e^{-D(r-R)}, \tag{2.1}$$

where r is the distance between solute center and water oxygen, R is the size of the solute, B and D are the inverse decay lengths of the repulsive and attractive parts of the potential, respectively, and A and C are constants chosen as follows: In the case of a purely repulsive solute $C = 0$ and $A = k_{\mathrm{B}}T_0$ with $T_0 = 300\,\mathrm{K}$. This defines the radius of the particle as the separation, where the interaction potential equals $k_{\mathrm{B}}T_0$, that is, $U_{\mathrm{SPH-OW}}(R) = k_{\mathrm{B}}T_0$. The decay length of the repulsive part is varied in the range $1/B = 0.005\,\mathrm{nm} - 0.03\,\mathrm{nm}$ with an increment of $0.001\,\mathrm{nm}$. The upper limit $0.03\,\mathrm{nm}$ corresponds to the decay length used in the parameterization of a Buckingham exponential-6 potential of a water oxygen atom [150] and should therefore give a realistic estimate for the stiffness of an interatomic potential. This value is therefore used in our study of the size dependence, where only the size R is varied and the other parameters are kept fixed.

In the limit of vanishing decay length, $1/B \to 0$, one obtains a hard core potential,

$$U^{\mathrm{HC}}_{\mathrm{SPH-OW}}(r) = \begin{cases} \infty, & \text{for } r < R \\ 0, & \text{for } r > R \end{cases}, \tag{2.2}$$

which we also study as a limiting case.

To obtain an attractive solute the constants A and C are chosen in such a way that (i) $U_{\mathrm{SPH-OW}}(R) = k_{\mathrm{B}}T_0$ and (ii) $\min(U_{\mathrm{SPH-OW}}(r)) = -\epsilon_0$, where ϵ_0 is the depth of the potential. We vary both the range of the attractive part, $1/D = 0.05, 0.1$ and $0.2\,\mathrm{nm}$, and the depth of the potential, $\epsilon_0 = 0.1$, 0.2, 0.3, 0.4, 0.5, 0.6, 0.7, 0.8 and $1.3\,\mathrm{kJ/mol}$. An illustration of the shape of the potential for various different parameters is given in Fig. 2.1. The advantage of such a double exponential potential over the more commonly used Lennard-Jones 12-6 potential is that the solute size R, the decay lengths of the repulsive and attractive parts $1/B$ and $1/D$ and the potential depth ϵ_0 can be varied independently, whereas in a Lennard-Jones potential there are only two free parameter and it is therefore not shape-invariant with increasing solute size. Another characteristic feature of the exponential potential is its finite value for $r \to 0$, which allows very small solutes to overlap with the water molecules. We show below that this effect is only significant for very small solutes, and is therefore no serious limitation for our purposes. We note that the radius R of the solute is an exclusion radius,

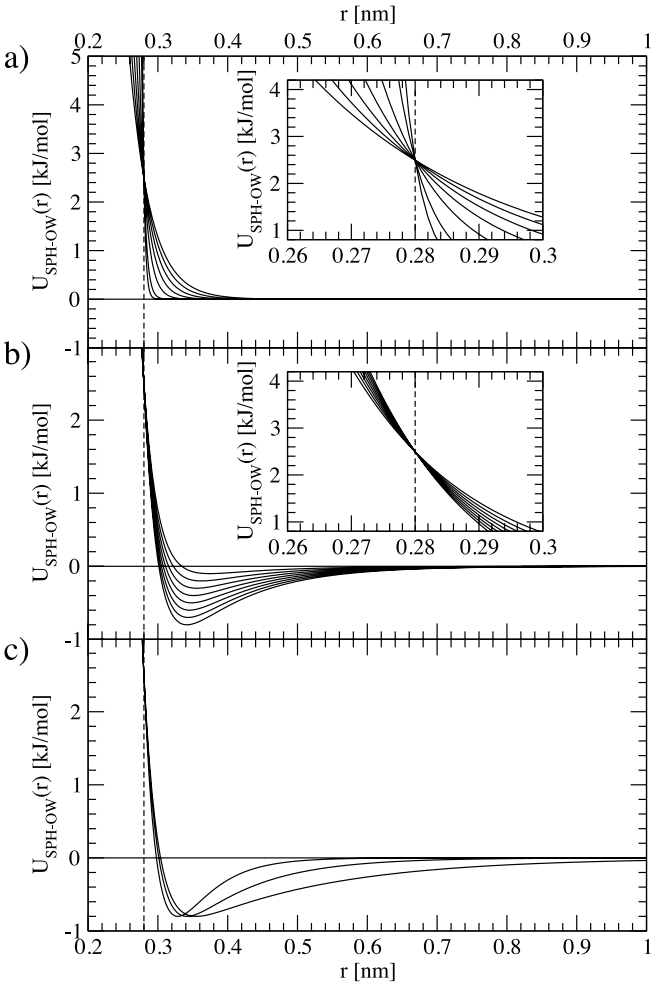

Figure 2.1.: Illustration of the solute-water interaction potential $U_{\mathrm{SPH-OW}}(r)$ (see Eq. 2.1) for a spherical solute of radius $R = 0.28\,\mathrm{nm}$ and various potential shapes. (a) Purely repulsive potential with varying decay lengths $1/B = 0.005$, 0.01, 0.015, 0.02, 0.025 and 0.03 nm. (b) Attractive potentials with $1/B = 0.02\,\mathrm{nm}$, attraction decay length $1/D = 0.05\,\mathrm{nm}$ and varying potential depth $\epsilon_0 = 0.1$, 0.2, 0.3, 0.4, 0.5, 0.6, 0.7 and 0.8 kJ/mol. (c) Attractive potentials with $1/B = 0.02\,\mathrm{nm}$, $\epsilon_0 = 0.8\,\mathrm{kJ/mol}$ and varying range $1/D = 0.05, 0.1$ and 0.2 nm. Vertical lines indicate the radius R of the solute, defined by $U_{\mathrm{SPH-OW}}(R) = k_{\mathrm{B}}T_0$ with $T_0 = 300\,\mathrm{K}$. The insets in (a) and (b) show enlarged views of the potential.

that is, it is the radius around the center of the solute from which the center of the water oxygen atom is effectively excluded by the repulsion. We neglect all interactions between the solute and the water hydrogens.

Cylindrical solutes are modeled as a string of spheres aligned along the z-axis, with an axial separation of Δz. The cylinder has the same length as the box size in z-direction, so that by the use of periodic boundary conditions, it has an infinite length and edge effects are excluded. The interaction potential of the cylindrical solutes with the water oxygen is therefore given by

$$V_{\mathrm{CYL-OW}}(r_{||}, z) = \tilde{A} \sum_{i=1}^{N} e^{-B\sqrt{r_{||}^2 + (z - z_i)^2}}, \tag{2.3}$$

where N is the number of spheres, $r_{||} = \sqrt{x^2 + y^2}$ is the distance from the cylinder axis and $z_i = i\Delta z$, $i = 1, \ldots, N$, are the z-positions of the spheres that form the cylinder. Note that in Eq. 2.3 we have absorbed the term $\exp(-BR)$ into the prefactor $\tilde{A}$.

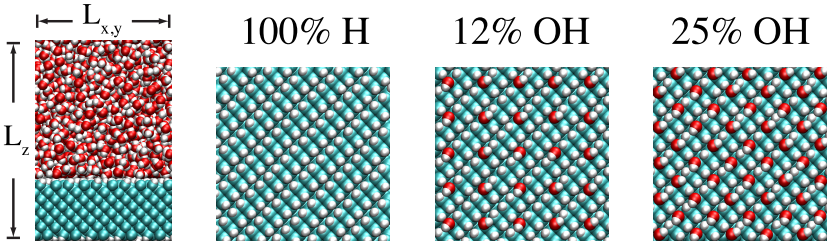

Figure 2.2.: Side view of the simulation box in the interfacial geometry and top views of the different hydrophobic and hydrophilic substrates.

To obtain a rather smooth cylinder, we choose the spacing between the spheres as $\Delta z = 0.025\,\mathrm{nm}$, which ensures that the corrugation of the potential along the z-axis is negligible and we have

$$\begin{aligned} V_{\mathrm{CYL-OW}}(r_{||}) &\approx \tilde{A}\int_{-\infty}^{\infty}\frac{dz}{\Delta z}e^{-B\sqrt{r_{||}^2+z^2}} \\ &= \frac{2\tilde{A}r_{||}}{\Delta z}K_1(Br_{||}), \end{aligned} \tag{2.4}$$

where K_1 is the first order modified Bessel function of the second kind. Analogously to the spherical solutes we choose $1/B = 0.03\,\mathrm{nm}$ and determine the constant $\tilde{A}$ by the condition $V_{\mathrm{CYL-OW}}(R) = k_\mathrm{B}T_0$. From that definition it follows, that $\tilde{A}(R) = \Delta z k_\mathrm{B}T_0/f_{\mathrm{CYL}}(B,R)$, with $f_{\mathrm{CYL}}(B,R) = 2RK_1(BR)$.

For comparison we also calculate solvation free energies for solutes interacting via the repulsive part of a Lennard-Jones potential,

$$V^{\mathrm{LJ}}_{\mathrm{SPH-SOL}}(r) = \frac{E}{r^{12}}. \tag{2.5}$$

The solute radii R are defined analogously to the Buckingham potential by $V^{\mathrm{LJ}}_{\mathrm{SPH-SOL}}(R) = k_\mathrm{B}T_0$, yielding $E = k_\mathrm{B}T_0R^{12}$.

As an example of a hydrophobic solute with optimized force field parameters we also study a methane molecule modeled in a united atom representation as a single Lennard-Jones sphere using the OPLS [151] force field parameters.

2.2.3. Planar interfaces

For the study of water near planar interfaces, we use a slab geometry, where a simulation box is only partially filled by water in the z-direction, the remaining part is either empty, thereby forming a setup with two planar air/water interfaces parallel to the xy-plane (see Fig. 5.1 and Fig. 5.3), or filled by a solid substrate (see Fig. 2.2). Due to the periodic boundary conditions, this setup corresponds to a water slab confined between two solid surfaces.

As a model for a nonpolar surface we use hydrogen-terminated diamond, to obtain polar surfaces a certain fraction of the terminal hydrogen atoms is replaced by hydroxyl groups. The diamond surface is modeled by the well known double face-centered-cubic lattice (lattice constant $a = 3.567$ Å) of carbon atoms with the $\langle 100 \rangle$ direction parallel to the z-axis. A slab of finite thickness is cut out of the lattice with its two surfaces perpendicular to the z-axis, and the surface layer is reconstructed and terminated by hydrogen atoms. The atoms of the diamond interact with each other via harmonic bond and angle potentials as well as a torsion potential. The interaction between a surface atom and a water oxygen atom is given by a Lennard-Jones potential.

For the hydrophilic diamond, a variable fraction (12% or 25%) of the terminal hydrogen atoms is replaced by hydroxyl groups with partial charges $q_C = 0.266$ e, $q_O = -0.674$ e and $q_H = 0.408$ e (see Fig. 2.2). The force constants and Lennard-Jones interaction parameters are taken from the GROMOS96 force field [152].

The contact angle of SPC/E water on the hydrophobic diamond was found to be $\Theta = 101°$ [9], while the hydrophilic substrates exhibit complete wetting.

2.3. Free energy simulations

The key quantity characterizing the solvation of a solute is its solvation free energy ΔF, that is, the free energy necessary to bring the solute from the pure ideal gas phase into aqueous solution. The solvation free energy per solute is equal to the solutes excess chemical potential $\Delta F = \mu_{ex}$ in the solution. From the temperature derivative of the solvation free energy one obtains the solvation entropy ΔS per solute,

$$\Delta S = -\frac{\partial \Delta F}{\partial T}. \tag{2.6}$$

and the solvation enthalpy,

$$\Delta H = \Delta F + T\Delta S. \tag{2.7}$$

We use different methods to determine the solvation free energy, based mainly on the size of the solute. While the Widom particle insertion method [153] is very efficient, it is only applicable for small solutes. We use it to determine the solvation free energies of small solutes with varying interaction parameters, where a wide range of different parameters is scanned. The thermodynamic integration method [126], on the other hand, can be used for arbitrary solute sizes, but demands much more computational effort. It is therefore used to determine solvation free energies for the large spherical and cylindrical solutes.

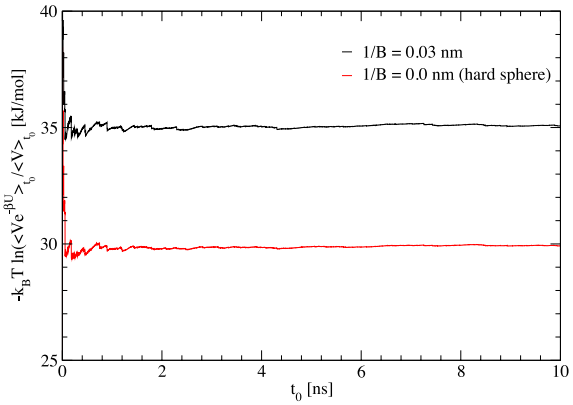

Figure 2.3.: Running average of the excess chemical potential calculated by the particle insertion method according to Eq. 2.8 for a purely repulsive solute of radius $R = 0.345\,\mathrm{nm}$ with a potential stiffness of $1/B = 0.03\,\mathrm{nm}$ (black curve) and for a hard core solute of the same size (red line), where the average $\langle . \rangle_{t_0}$ is taken over all saved configurations with $t < t_0$. The insertions are done in a box containing 895 SPC/E water molecules simulated at $T = 300\,\mathrm{K}$. In each configuration of the trajectory $n_{\mathrm{ins}} = 10^7$ insertions are performed for the finite potential stiffness and $n_{\mathrm{ins}} = 2 \cdot 10^6$ for the hard core solutes. It is seen, that the excess chemical potential is well converged after 10 ns.

2.3.1. Particle insertion method

We determine the excess chemical potential of small solutes with varying interaction parameters by the Widom particle insertion method [153]. In the case of an isobaric-isothermal ensemble it is given by [154]

$$\mu_{\mathrm{ex}} = -k_{\mathrm{B}} T \ln \left(\frac{< V e^{-\beta \Delta U} >}{< V >} \right), \tag{2.8}$$

where ΔU is the potential energy of the interaction between the solute and the solvent, V is the volume of the system, $\beta = 1/(k_{\mathrm{B}} T)$ and the angle brackets denote an isobaric-isothermal average over configurations of the system without the solute.

For each saved configuration $n_{\mathrm{ins}} = 10^7$ insertions are performed in the case of a finite potential stiffness and $n_{\mathrm{ins}} = 2 \cdot 10^6$ in the case of hard sphere solutes. Figure 2.3 shows the running average, that is an average including only configurations up to a certain time t_0, of the excess potential (Eq. 2.8) for a purely repulsive solute of radius $R = 0.345\,\mathrm{nm}$ with a potential stiffness of $1/B = 0.03\,\mathrm{nm}$ (black curve) and a hard core solute of the same size (red curve) in SPC/E water at $T = 300\,\mathrm{K}$. It is seen that the excess potential is well converged after 10 ns.

2.3.2. Thermodynamic integration method

To determine the solvation free energies of large spherical and cylindrical solutes ΔF, the method of thermodynamic integration is used, which relates the free energy dif-

ference $\Delta\tilde{F}$ between two states I and II of a thermodynamic system, characterized by two potential energy functions U^{I} and U^{II}, to the averaged derivative $\langle \partial U(\lambda)/\partial\lambda \rangle$ of an intermediate potential energy $U(\lambda)$, that connects the two states by a virtual path, i. e., $U(\lambda = 0) = U^{\mathrm{I}}$ and $U(\lambda = 1) = U^{\mathrm{II}}$, where $\lambda = 0 \ldots 1$ is a path variable. The free energy difference $\tilde{F}$ between the two states is then given by the integral

$$\Delta\tilde{F} = \int_0^1 d\lambda \langle \frac{\partial U(\lambda)}{\partial\lambda} \rangle_\lambda, \tag{2.9}$$

where the average $\langle . \rangle_\lambda$ has to be taken for a system interacting via $U(\lambda)$. To obtain the solvation free energy of a solute, the initial state I is chosen such that the solute does not interact with the solvent, while in the final state II, the full interaction with the solvent is switched on. That is, the potential energy function U^{I} contains no solute-solvent interactions, while U^{II} contains the full interaction. For simulations in an isobaric-isothermal ensemble the solvation free energy contains an additional term due to the volume change [155],

$$\Delta F = \Delta\tilde{F} + k_{\mathrm{B}} T \ln(\frac{V^{\mathrm{II}}}{V^{\mathrm{I}}}), \tag{2.10}$$

where V^I and V^{II} are the system volumes in state I and state II, respectively. This term accounts for the difference in the ideal gas entropy in the initial and final state of the thermodynamic integration. For the solvation of a nonpolar solute, this volume change is mainly due to the solute's volume ΔV, since the water can be considered incompressible to a good approximation. If the volume of the simulation box V is much larger than the volume of the solute, the correction term is small.

For large solutes it is convenient to break the thermodynamic integration into several steps with varying system sizes, going from an initial size R^{I} to a final size R^{II} in each step, where $R^{\mathrm{I}} = 0$ for the first step and R^{II} equals the desired solute size in the last step. In this way, smaller simulation boxes can be used for small solutes, reducing the computational cost.

We perform linear scaling between the states, that is the potential energy function of the intermediate states is defined by

$$U^{R^{\mathrm{I}} \to R^{\mathrm{II}}}(\lambda) = (1 - \lambda) U^{R^{\mathrm{I}}} + \lambda U^{R^{\mathrm{II}}}. \tag{2.11}$$

Since the repulsive Buckingham potential has no divergence at small distances, linear scaling is possible even for the first step, where the solute is completely decoupled in the initial state, without getting a diverging $\langle \partial U^{R^{\mathrm{I}} \to R^{\mathrm{II}}}(\lambda)/\partial\lambda \rangle$, as for a Lennard-Jones potential [156].

Since the radius of the solute depends only on the prefactor of the interaction potential, the potential $U^{R^{\mathrm{I}} \to R^{\mathrm{II}}}(\lambda)$ at each intermediate λ-value corresponds to a solute of intermediate radius $R(\lambda)$. Conversely, the λ-values can be chosen in such a way, that they correspond to equidistant values of the solute radius. For the integration

step from R^{I} to R^{II} the intermediate λ-value corresponding to a solute of radius R ($R^{\mathrm{I}} < R < R^{\mathrm{II}}$) is

$$\lambda(R) = \frac{f_{\mathrm{X}}(B,R) - f_{\mathrm{X}}(B,R^{\mathrm{I}})}{f_{\mathrm{X}}(B,R^{\mathrm{II}}) - f_{\mathrm{X}}(B,R^{\mathrm{I}})}, \tag{2.12}$$

for the case of a spherical (X=SPH) and cylindrical (X=CYL) solute, respectively, where $f_{\mathrm{SPH}}(B,R) = \exp(BR)$ and $f_{\mathrm{CYL}}(B,R)$ is defined above (see text after Eq. 2.4). The solvation free energy for a solute of radius R is then given by

$$\begin{aligned} \Delta F(R) = &\int_0^{\lambda(R)} d\lambda \langle \frac{\partial U^{R^{\mathrm{I}}\to R^{\mathrm{II}}}(\lambda)}{\partial \lambda} \rangle \\ &+ k_{\mathrm{B}} T \ln(\frac{V(R)}{V(R^{\mathrm{I}})}) + F(R^{\mathrm{I}}), \end{aligned} \tag{2.13}$$

with $R^{\mathrm{I}} < R < R^{\mathrm{II}}$. In order to ensure proper equilibration, we calculate the average $\langle \partial U^{R^{\mathrm{I}}\to R^{\mathrm{II}}}(\lambda)/\partial\lambda \rangle$ for a discrete set of λ-values corresponding to a radius increment of $\Delta R = 0.0125$ nm. The solvation free energy is subsequently obtained by integrating a quadratic spline interpolation of the resulting data set, thereby reducing the integration error significantly. We use the TI method to calculate solvation free energies of Buckingham spheres and cylinders for radii up to $R = 2.0$ nm. We carefully check the accuracy of the procedure as explained in detail in App. B.

CHAPTER 3

CORRELATIONS OF DENSITY AND STRUCTURAL FLUCTUATIONS IN BULK WATER

3.1. Introduction

3.1.1. Motivation

Understanding the water structure in the pure bulk liquid is the prerequisite for understanding its behaviour in more complex situations. But even the bulk behaviour of water is surprisingly difficult to understand, partly due to anomalous behaviour in almost all thermodynamic observables [15]. The best-known example is certainly the anomaly in the water density, which shows a maximum at 4° C, at which temperature the thermal expansion coefficient $\alpha_P = 1/V\,(\partial V/\partial T)_P$ changes sign. But also other thermodynamic properties like the isothermal compressibility $\kappa_T = -1/V\,(\partial V/\partial P)_T$ and the isobaric heat capacity $C_P = (\partial H/\partial T)_P$ exhibit anomalies: At atmospheric pressure κ_T has a minimum at 46°C and C_P has a minimum at 35°C [14, 157–159]. This stands in marked contrast to the behaviour of simple liquids, whose thermodynamic properties vary monotonously with temperature.

Despite intense efforts for many years, there is still no complete and simple explanation for these anomalies. Several hypotheses have been proposed [160–162], among which the liquid-liquid critical point (LLCP) scenario has received much support in the recent literature. According to the LLCP scenario, water possesses a metastable critical point at very low temperatures which marks the endpoint of a first order phase transition between a high density (HDL) and a low density (LDL) liquid phase. The LDL phase is associated with tetrahedral-like local structure, while the HDL phase corresponds to a local structure with distorted hydrogen bonds [21, 163]. The anomalous temperature dependence of the thermodynamic response functions then follows naturally, since they are expected to diverge at the transition line or exhibit maxima or minima at the continuation of the transition line into the one phase region [163]. However, conclusive experimental evidence for this scenario is still missing and the

connection between anomalous water properties and the existence of low-temperature singularities is controversially discussed [163, 164].

Recently, it has been suggested that remnants of these phases persist even at higher temperatures and that extended clusters of HDL and LDL are present at ambient conditions [20]. These conclusions were partly based on the well-known experimental observation that the structure factor $S(q)$, obtained from SAXS or neutron scattering, shows an enhancement at very low wave vectors q [23, 123, 124, 165]. In conjunction with X-ray adsorption, Rahman and Emission spectroscopy it was argued that the density fluctuations manifest in $S(q)$ originate from concentration fluctuations of two structurally distinct liquid species differing in density [20]. From an Ornstein-Zernike (OZ) analysis of the scattering data the typical size of these clusters was estimated to be on the order of ≈ 1 nm. It was also stated that standard three-point water models such as SPC/E are not able to reproduce the minimum in the structure factor [20], from which it was concluded that the local water structure is ill-reproduced by current classical simulation models for water.

The relationship between the density and structure of water has been much discussed in recent literature [23, 166–168], partly because this relation is crucial for understanding the water density anomaly. Using an analysis of structural water clusters in SPC/E water simulations, Errington et al. [166] have found a decrease in the density of water clusters both with increasing tetrahedrality and increasing cluster size at temperatures of $T = 220$ K and $T = 240$ K. This suggests that the formation of tetrahedrally ordered low-density water is cooperative. Moore and Molinero [167] used the monatomic mW [169] water model for an extensive study of the water structure in the temperature range from 100 K to 350 K. They found an increase in the average tetrahedrality and the fraction and cluster size of four-coordinated molecules upon cooling. However, they did not observe a low-q enhancement of the structure factor, which they attributed to the lack of density difference between differently coordinated water molecules in the mW model [167]. Only when they restricted the calculation of the structure factor to four-coordinated water molecules, they saw an increase for low q from which they infer correlation lengths that grow with decreasing temperature, using an OZ analysis. Matsumoto [168] showed that the change in the average composition of differently coordinated water molecules upon cooling is not correlated with the mean density of the liquid. He could accurately explain the temperature dependence of the density by taking into account the interplay of the average bond length, which decreases upon cooling and therefore tends to increase the density, and the distortion of the tetrahedral bonding network, which decreases upon cooling and thereby decreases the density. Very recently, Soper et al. [22] and Clark et al. [23] argued that an enhancement in the low-q region of the structure factor is consistent with normal particle number fluctuations and not necessarily indicates the presence of two structural water species with different densities. Furthermore, it was shown that the OZ analysis applied in Ref. 20 used to infer a spatial scale of regions with correlated densities is not very meaningful far away from a critical point. Clark et al. [23] very convincingly demonstrated the absence of pronounced density inho-

mogeneities on lengthscales ranging from 0.6 nm to 6 nm based on the unimodality of density histograms obtained by simulations of TIP4P-Ew water [23], thus casting additional doubt on the interpretation of S(q) data as a sign of the coexistence of two different local structural motifs in liquid water [20].

While the relation between spatially averaged structural properties and the mean density of water seems well understood, the question of the existence and spatial size of structurally correlated regions in liquid water is less clear. In particular, the discussion in Ref. 20 raised the question to what degree the spatial extent of density correlations (as directly inferred from SAXS experiments via the structure factor) is related to the size of structurally correlated water patches (which can only indirectly be inferred from experiments).

3.1.2. Outline

Instead of using clustering algorithms to define the size of regions with high structural order [166–168], we determine spatial two-point correlation functions involving the local density and different local structural order parameters, namely the tetrahedrality order parameter [125, 170, 171], ψ, and the number of hydrogen bonds a water molecule forms with its neighbours, n_{HB}. By using the exact same mathematical form for assessing the presence of spatial correlations of density and structural fluctuations, we are able to make a simple and meaningful comparison between density-density correlations (expressed in terms of the well-known radial distribution function) and density-structure and structure-structure correlations. Except for the density-density correlation function, we find only weak correlations that decay to zero within a few Å. This means that although water is a highly structured fluid, the structure shows only weak spatial correlation and that the coupling between density and structural fluctuations is also quite weak when compared with the degree to which density-density correlations are present.

In order to check how robust the simulated structure factor is with respect to force field modifications, we compare the SPC/E [146], the TIP4P/2005 [147] and the TIP5P [148] water models. The SPC/E water model has a density maximum at $T = 235$ K [172] and a minimum in κ_T around $T = 270$ K [149] and thus differs considerably from the experimental values. It exhibits the LDA and HDA phases in the amorphous state [173, 174] and it has been suggested, that it has a LLCP [175]. The TIP5P water model has been parameterized to yield the correct position of the density maximum at $T = 277$ K [148] using a reaction field method to account for electrostatic periodic boundary conditions. Note that in combination with the Particle Mesh Ewald summation method [136, 137], as used in this work, the density maximum is shifted slightly to $T = 284$ K [176]. It has been shown, that the TIP5P water model shows a LLCP [174, 177] and that its isobaric heat capacity shows a sharp increase for decreasing temperature [174], in accordance with the experimental data. The isothermal compressibility of the TIP5P water model does not show a minimum within the range studied so far [149]. The TIP4P/2005 model is a recent reparam-

eterization of the widely used TIP4P [178] water model. It excellently reproduces the temperature dependence of the density as well as the isothermal compressibility at atmospheric pressure, exhibiting a density maximum at $T = 278$ K [147] and a minimum in κ_T at $T = 310$ K [149]. The TIP4P model has a LLCP [174], so it is likely that the TIP4P/2005 model has a LLCP, too. We find that all three water models exhibit an enhancement of the structure factor for low q, which is pronounced for the TIP5P and TIP4P/2005 water models, and still perceptible for the SPC/E water model. The TIP4P/2005 model almost quantitatively accounts for the experimental structure factor in the low-q region, while the TIP5P and SPC/E models show various degrees of deviation. Together with the results of Clark et al. [23], who found a minimum of $S(q)$ using the TIP4P-Ew water model in very good agreement with experiment, this shows that the scattering enhancement at low q is a quite robust feature of simple classical water models and does not point to any subtle structural property of water that is missed by these models. Clearly, the accurate determination of the low-q region of the structure factor is a challenging task in simulations, since in a finite system the minimal accessible wave vector as well as the resolution in reciprocal space are inversely proportional to the system size. Therefore, large systems are necessary leading to high computational costs. Furthermore, the method to extract the structure factor from simulation trajectories has to be chosen with care, since finite size artifacts can otherwise obscure the results [179]. Clark et al. [23] managed to reduce Fourier truncation ripples by performing simulations in the grand canonical ensemble. We compare several methods to extract the structure factor from simulations in the canonical ensemble that yield a consistent picture of the low-q region of the structure factor.

3.2. Structure factor and orientational order parameters

From Molecular Dynamics (MD) simulations we can obtain information about density and structural correlations of water in the liquid temperature range.

Structure factor. On the two-point level the density correlations of a fluid are characterized by the pair distribution function,

$$g(\vec{r},\vec{r}') = \frac{\langle \rho^{(2)}(\vec{r},\vec{r}')\rangle}{\langle \rho(\vec{r})\rangle\langle \rho(\vec{r}')\rangle}, \tag{3.1}$$

where $\rho^{(2)}(\vec{r},\vec{r}') = \sum_{i,j=1;i\neq j}^{N} \delta(\vec{r}-\vec{r}_i)\delta(\vec{r}'-\vec{r}_j)$ and $\rho(\vec{r}) = \sum_{i=1}^{N}\delta(\vec{r}-\vec{r}_i)$ are the two and one particle density operators, N is the number of particles and $\vec{r}_i$ is the position of the i-th particle. For a homogenous and isotropic system $g(r) = g(\vec{r},\vec{r}')$ is a function of the distance $r = |\vec{r}-\vec{r}'|$ only and called radial distribution function (RDF). The RDF can be extracted straightforwardly from a MD simulation by generat-

ing a histogram of inter particle distances and appropriate normalization. Scattering experiments measure the structure factor $S(\vec{q})$, defined as

$$S(\vec{q}) = \langle \frac{1}{N} \sum_{i,j=1}^{N} e^{-i\vec{q}\cdot(\vec{r}_i - \vec{r}_j)} \rangle. \tag{3.2}$$

For a homogeneous and isotropic system it is a function of $q = |\vec{q}|$ only and related to the RDF by a Fourier transformation [180],

$$S(q) = 1 + 4\pi\rho \int_0^\infty dr r \frac{\sin(qr)}{q} (g(r) - 1), \tag{3.3}$$

where $\rho = \langle \rho(\vec{r}) \rangle = N/V$ is the number density of the fluid. Eq. 3.3 constitutes the first of the two methods used to calculate the structure factor in this work (FT method) and is based on the RDFs obtained from MD simulations. Note, that we take only the oxygen atoms of the water molecules into account, thereby assuming that the electron density of the water molecule is approximately spherical and centered around the oxygen atom [181]. Due to the periodic boundary conditions and the minimum image convention used in the MD simulation the RDF can only be obtained up to a radius $r_{\max} = L/2$, where L is the length of the periodic box. Therefore, the upper boundary in the integral in Eq. 3.3 has to be replaced by $r_{\max}$, which leads to pronounced "cutoff ripples" especially for low wave vectors q [179] and effectively restricts the use of Eq. 3.3 to the range $q > q_{\min}^{\mathrm{FT}} = 2\pi/r_{\max}$. The cubic simulation box we use in this study has a size of $L \approx 10$ nm and thus $q_{\min}^{\mathrm{FT}} \approx 1.2\ \mathrm{nm}^{-1}$. Due to the r factor in the integrand of Eq. 3.3 these cutoff artifacts are increased even by minute numerical errors in the RDF at larger radii, which might be introduced for example by round-off errors. To enforce that the RDFs correctly converge to 1 for large r, we calculate the average of the RDF over the interval 3 nm $< r <$ 5 nm and divide the RDF by that average. Typically, the deviations of the average from 1 before the normalization are on the order of 10^{-5}.

Since the aforementioned subtleties in the application of Eq. 3.3 to calculate the structure factor prohibit a clear interpretation of $S(q)$, especially in the low-q limit we are interested in, we also calculate the structure factor directly from the simulation trajectories by applying the definition, Eq. 3.2. One can rewrite Eq. 3.2 in the following way,

$$S(\vec{q}) = \langle \frac{1}{N} \big[\sum_{i=1}^{N} \sin(\vec{q}\cdot\vec{r}_i) \big]^2 \rangle + \langle \frac{1}{N} \big[\sum_{i=1}^{N} \cos(\vec{q}\cdot\vec{r}_i) \big]^2 \rangle], \tag{3.4}$$

which is more convenient for evaluation from a simulation trajectory, since it contains only single sums. Eq. 3.4 constitutes the second method used to calculate the structure factor in this work (D method). Due to the finite size of our simulation system, $S(\vec{q})$ can only be evaluated for wave vectors $\vec{q} = (n_x, n_y, n_z)2\pi/L$, where the n_i are integers

and L is the length of the simulation box, which in our simulations is cubic. The minimum wave vector that can be sampled is therefore given by $q^{\mathrm{D}}_{\mathrm{min}} = 2\pi/L$ and thus smaller by a factor of two compared to the FT method, leading to $q^{\mathrm{D}}_{\mathrm{min}} \approx 0.6\ \mathrm{nm}^{-1}$ for the box size used in this study.

Additional information on the low q behaviour of the structure factor is available from thermodynamics. The limiting value $S(0)$ for $q \to 0$ is connected to the isothermal compressibility $\kappa_{\mathrm{T}} = -1/V(\partial V/\partial P)_{\mathrm{T}}$ by the relation [180],

$$S(0) = \rho k_{\mathrm{B}} T \kappa_{\mathrm{T}}, \tag{3.5}$$

which will be used as a stringent test of the data for $S(q)$ at small but finite q.

Isothermal compressibility. The isothermal compressibility is determined by a finite difference method [182],

$$\kappa_{\mathrm{T}} = \frac{1}{\rho}\left(\frac{\partial \rho}{\partial P}\right)_{\mathrm{T}} \approx \frac{\ln(\rho_2/\rho_1)}{P_2 - P_1}. \tag{3.6}$$

To evaluate this expression the system is simulated in a NVT ensemble with the densities $\rho_{1,2} = \rho \pm 0.04$ kg/l and the resulting pressures $P_{1,2}$ are sampled. Here ρ is the equilibrium density at a pressure of $P = 1$ bar, as obtained from separate MD simulations (see Tab. 3.1). The resulting compressibilities (see Tab. 3.1) agree very well with those from previous studies, see e. g. Ref. 149, where κ_{T} was calculated from volume fluctuations in an isobaric-isothermal ensemble.

Order parameters. To quantify the degree of water structuring we use two different order parameters. The first one is the tetrahedrality order parameter ψ [170] with the normalization used by Errington and Debenedetti [125],

$$\psi = 1 - \frac{3}{8}\sum_{i=1}^{3}\sum_{j=i+1}^{4}\left(\cos(\phi_{ij}) + \frac{1}{3}\right)^2, \tag{3.7}$$

where ϕ_{ij} is the angle formed by the lines connecting the oxygen atom of a given water molecule to the oxygen atoms of its i-th and j-th nearest neighbor. Only the four nearest neighbors are taken into account. In order to investigate spatial correlations, we define the spatially resolved tetrahedrality density,

$$\psi(\vec{r}) = \sum_{i=1}^{N} \psi_i \delta(\vec{r} - \vec{r}_i), \tag{3.8}$$

where ψ_i and $\vec{r}_i$ are the tetrahedrality and the position of the i-th water molecule.

As a second measure for the water ordering we use the number of hydrogen bonds (HB), n_{HB}, a water molecule forms with its neighbors. Two water molecules are considered to form an HB if the distance between their oxygen atoms is less than $r_{\mathrm{HB}} = 0.35$ nm and the angle formed by the OH vector of one molecule and the line connecting the oxygen atoms of both molecules is less than $\theta_{\mathrm{HB}} = 30°$. Analogously to

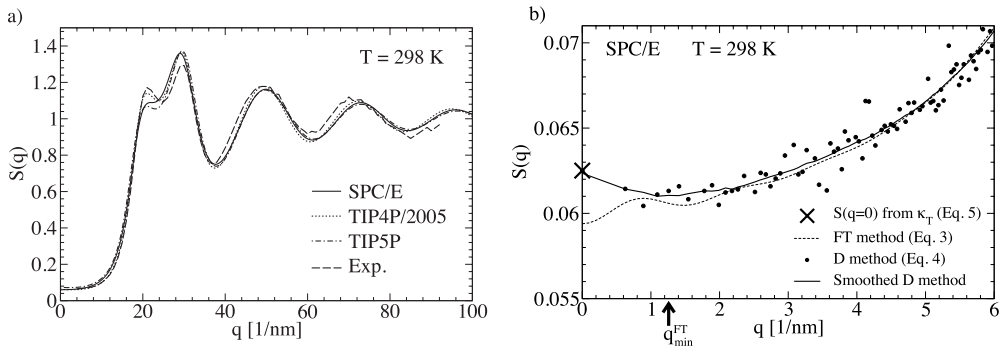

Figure 3.1.: (a) Structure factor $S(q)$ obtained by the FT method (see Eq. 3.3) at $T = 298$ K and $p = 1$ bar for the SPC/E (full line), TIP4P/2005 (dotted line) and TIP5P (dashed dotted line) water models in comparison with the experimental $S(q)$ (dashed line). The experimental data for the scattering cross-section is taken from an X-Ray scattering experiment [183], and we calculate the structure factor using the isotropic form factor from quantum chemical calculations [184]. (b) Low-q region of the structure factor for SPC/E water at $T = 298$ K and $p = 1$ bar obtained by the FT method (dashed line, see Eq. 3.3) and by the direct method (filled circles, see Eq. 3.4). The $S(q = 0)$ value obtained by Eq. 3.5 (cross) is also shown. The full line is obtained by smoothing the data from the direct method including the $S(q = 0)$ value. Note that in the smoothing we did not enforce the slope of $S(q)$ to vanish at $q = 0$. The minimum wave vector of the FT method, $q_{\min}^{\mathrm{FT}} \approx 1.2$ nm^{-1}, is indicated by an arrow.

the tetrahedrality order parameter we define the spatially resolved HB number density,

$$n_{\mathrm{HB}}(\vec{r}) = \sum_{i=1}^{N} n_{\mathrm{HB},i}\,\delta(\vec{r} - \vec{r}_i), \tag{3.9}$$

where $n_{\mathrm{HB},i}$ is the number of HBs the i-th water molecule forms with its neighbours. Note, that with the above definitions $\langle n_{\mathrm{HB}}(\vec{r})\rangle = \langle n_{\mathrm{HB}}\rangle\rho$ and $\langle \psi(\vec{r})\rangle = \langle\psi\rangle\rho$.

3.3. Results and discussion

3.3.1. Structure factor

It is a subtle task to extract the low wave vector region of the structure factor $S(q)$ from computer simulations, since the minimal accessible wave vector and the resolution in reciprocal space are restricted by the size of the simulated system. To determine $S(q)$ unambiguously we use two different methods. The first method, to which we will refer in the following as Fourier transform (FT) method, makes use of Eq. 3.3 to obtain the structure factor from the radial distribution function. The second method (direct method) is to directly calculate $S(q)$ from the simulation trajectories by Eq. 3.4. Additionally we determine the isothermal compressibility κ_T to calculate the $q \to 0$

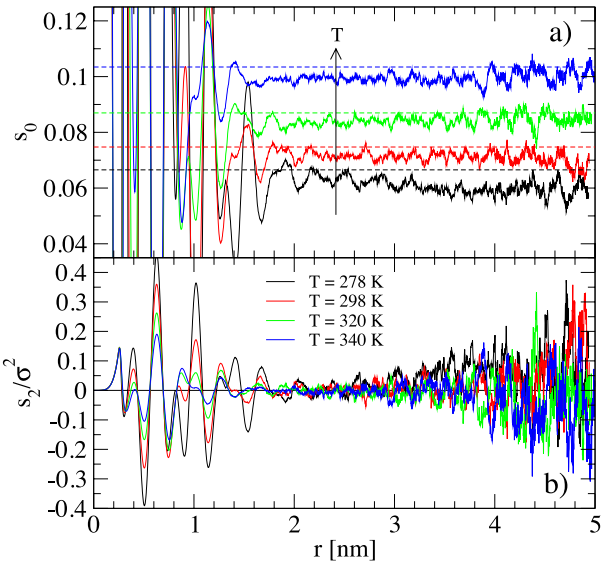

Figure 3.2.: Running integral of the (a) zero order and (b) normalized second order coefficient of the Taylor expansion of the structure factor of the SPC/E water model (Eq. 3.11) for different temperatures $T = 278$, 298, 320 and 340 K, where $\sigma = 3.17$ Å is the Lennard-Jones length of SPC/E water. Dashed lines in (a) indicate the $S(q = 0)$ values obtained from the compressibility data (see Tab. 3.1) by Eq. 3.5.

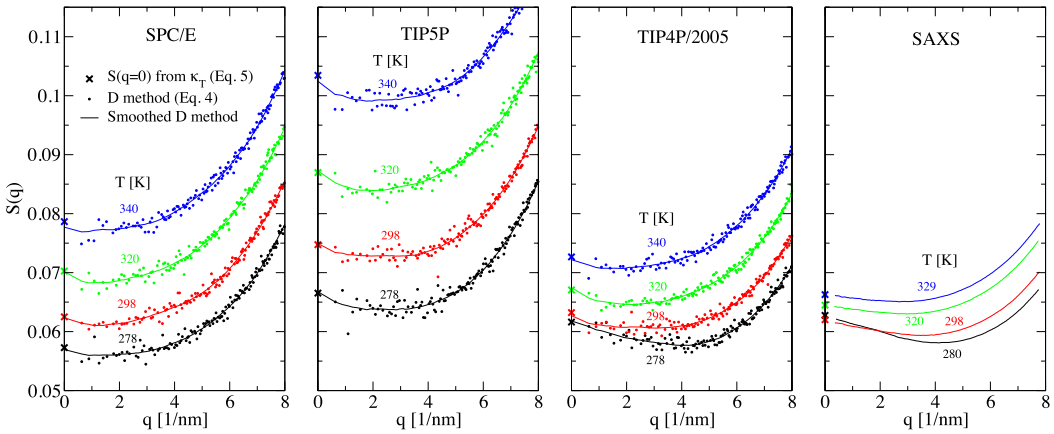

Figure 3.3.: Small wave vector region of the structure factor $S(q)$ obtained from MD simulations of the SPC/E, TIP5P and TIP4P/2005 water models and from experimental SAXS data (taken from Ref. 20). Filled circles are the result of the direct evaluation of Eq. 3.4. The $S(q = 0)$ values obtained from the compressibility data by Eq. 3.5 are marked by crosses. Full lines are obtained by smoothing of the data from the direct method including the $S(q = 0)$ values obtained from the compressibility (not enforcing a vanishing slope at the origin). Different colors indicate different temperatures as indicated in the graphs. Experimental compressibilities are taken from Ref. 14.

Table 3.1.
Densities, compressibilities and mean structural order parameters for the studied water models obtained from MD simulations at a pressure of $p = 1$ bar.

water model	T [K]	ρ [kg/l]	κ_T [10^{-11} Pa^{-1}]	$S(q=0)$	$\langle\psi\rangle$	$\langle n_{\mathrm{HB}}\rangle$
SPC/E	278	1.008	44.32	0.057	0.661	3.69
SPC/E	298	0.999	45.50	0.063	0.635	3.61
SPC/E	320	0.987	48.23	0.070	0.609	3.51
SPC/E	340	0.973	51.53	0.079	0.588	3.41
TIP5P	278	0.986	52.62	0.067	0.713	3.51
TIP5P	298	0.983	55.30	0.075	0.661	3.34
TIP5P	320	0.969	60.80	0.087	0.615	3.16
TIP5P	340	0.949	69.47	0.103	0.581	3.01
TIP4P/2005	278	1.001	48.02	0.062	0.700	3.75
TIP4P/2005	298	0.998	46.11	0.063	0.670	3.67
TIP4P/2005	320	0.989	45.92	0.067	0.640	3.57
TIP4P/2005	340	0.979	47.32	0.073	0.616	3.48

limit of the structure factor, given by $S(0) = \rho k_{\mathrm{B}} T \kappa_{\mathrm{T}}$. The results for the compressibility are summarized in Tab. 3.1. We use simulation boxes with a size of roughly $10 \times 10 \times 10$ nm^3, containing $\approx 30\,000$ water molecules, yielding minimal wave vectors of $q_{\mathrm{min}}^{\mathrm{D}} \approx 0.6$ nm^{-1} and $q_{\mathrm{min}}^{\mathrm{FT}} \approx 1.2$ nm^{-1} for the two different methods.

In Fig. 3.1 a we show the structure factor of the SPC/E, the TIP4P/2005 and the TIP5P water model at $T = 298$ K and $p = 1$ bar, obtained by the FT method, over a large q-range in comparison with experimental results. It can be seen, that all water models quite accurately reproduce the position of the first three peaks of the experimental structure factor, while they differ slightly in the height of the peaks, in agreement with earlier simulation results [178]. Fig. 3.1 a is mainly shown to stress that the discussion of the low-q region of $S(q)$ for $q < 10\mathrm{nm}^{-1}$ concentrates on a small part of the full $S(q)$ curve where the scattering intensity is quite small and relatively featureless.

Fig. 3.1 b shows a close-up view of the low-q region of the structure factor for the SPC/E water model at $T = 298$ K, comparing the different methods to extract the structure factor from the simulations. The dashed line marks the result of the FT method, filled circles the results of the direct method and the $S(q = 0)$ value obtained from the compressibility is marked by a cross. The solid line is obtained by applying a second order Savitzky-Golay smoothing filter [185] with a fixed interval width of $\Delta q = 2$ nm^{-1} to the results from the direct method including the $S(q = 0)$ value obtained from the compressibility. In the FT method results one clearly observes cutoff ripples at low q and pronounced deviations from the direct method results and from the $S(q = 0)$ value inferred from the compressiblilities.

The reason is the high sensitivity of the FT method in the low-q region to statistical fluctuations in the RDF. This becomes apparent if we look at a Taylor expansion of $S(q)$,

$$S(q) = \sum_{i=0}^{\infty} s_{2i}\, q^{2i}, \tag{3.10}$$

$$s_{2i} = \delta_{i,0} + \frac{(-1)^i 4\pi\rho}{(2i+1)!} \int_0^{\infty} dr\, r^{2i+2}[g(r)-1]. \tag{3.11}$$

The function value and the curvature at $q = 0$ of $S(q)$ are determined by the first two terms in the expansion and thus by the coefficients s_0 and s_2. Obviously, the slope of $S(q)$ at $q = 0$ vanishes. In Fig. 3.2, we plot the running integrals corresponding to s_0 (Fig. 3.2 a) and s_2 (Fig. 3.2 b) obtained from the RDF of the SPC/E water model at different temperatures of $T = 278$, 298, 320 and 340 K. Also included in Fig. 3.2 a are the results for $S(q = 0)$ estimated from Eq. 3.5 (dashed lines). It is obvious from Fig. 3.2 a, that the statistical fluctuations, amplified by the r^2 factor in the integral, make an accurate determination of s_0 impossible. The actual s_0 value obtained from Eq. 3.11 and therefore also the $S(q = 0)$ value calculated by the FT method is a result of these random fluctuations. The situation is even worse for s_2, since there is a factor of r^4 in the integral. This shows, that a meaningful determination of the curvature of $S(q)$ for $q = 0$ from the FT method alone is not possible. It also demonstrates that even very slight numerical inaccuracies in the RDF can result in significant changes of the low-q behaviour of the structure factor.

Fig. 3.3 shows the low-q region of the structure factor of the SPC/E, the TIP5P and the TIP4P/2005 water models at different temperatures using the direct method. Also included for comparison are the experimental curves of Ref. 20 (SAXS). It is seen, that for the TIP5P and TIP4P/2005 water models there is a pronounced minimum in the structure factor at wave vectors between $q \approx 3$ nm^{-1} and $q \approx 5$ nm^{-1}, in agreement with previous results for the TIP4P-Ew water model [23]. For the SPC/E model the minimum is less pronounced but still perceptible. Quantitatively, the results for the SPC/E and TIP5P water models deviate somewhat from the experimental $S(q)$, while the TIP4P/2005 model compares excellently with the experiment. So rather than stressing the differences between different water models, we take as the main message of this figure that all water models studied by us and also the TIP4P-Ew model [23], exhibit an $S(q)$ minimum at small q, which means that this is a quite robust feature of classical water models.

3.3.2. Order parameters

In the following we investigate to what extent the enhancement seen in the low-q region of the structure factor is related to spatial correlations of the water structure. To that end we examine two structural order parameters and their self and

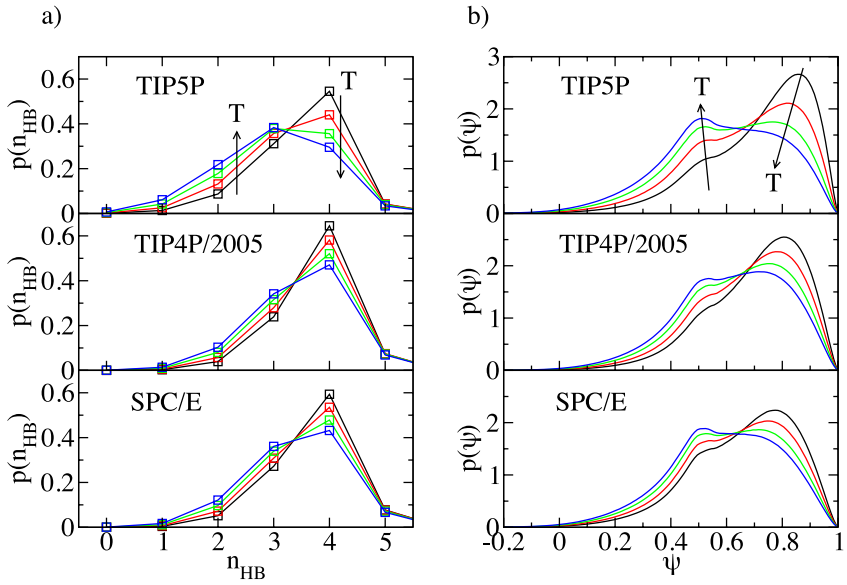

Figure 3.4.: (a) Probability distribution $p(n_{\mathrm{HB}})$ of the number of hydrogen bonds n_{HB} and (b) probability distribution $p(\psi)$ of the tetrahedrality order parameter ψ for TIP5P, TIP4P/2005 and SPC/E water at temperatures of $T = 278$ K (black), 298 K (red), 320 K (green) and 340 K (blue) and at a pressure of $p = 1$ bar. Arrows indicate the effect of increasing temperature.

cross-correlations with the local density. The geometric aspects of the local water ordering can be accurately described by the tetrahedrality order parameter ψ, defined in Eq. 3.7. For a perfect tetrahedral network $\psi = 1$, while for randomly oriented molecules $\psi = 0$. As a measure for the strength of the hydrogen bonding network we take the number of hydrogen bonds n_{HB} a water molecule forms with its neighbors. Here, we adopt the commonly used HOO-angle and OO-distance criterium for the hydrogen bond formation [19]. Fig. 3.4 and Fig. 3.5 show the single and joint probability distribution of the two order parameters for the studied water models and varying temperatures. In agreement with previous studies [125], the tetrahedrality parameter displays a bimodal structure and for increasing temperature the probability of the high-ψ peak decreases while the probability of the low-ψ peak increases. Similarly, the number of water molecules forming four hydrogen bonds decreases, while the number of water molecules forming three or less hydrogen bonds increases with increasing temperature. From the joint probability distribution (Fig. 3.5) it transpires that the high-ψ peak corresponds to water molecules forming four hydrogen bonds, while the low-ψ peak corresponds to water molecules forming three or less hydrogen bonds. The distinctly different ψ distributions of the sub populations for $n_{\mathrm{HB}} = 3$ and $n_{\mathrm{HB}} = 4$ explains the bimodality of the ψ distributions in Fig. 3.4.

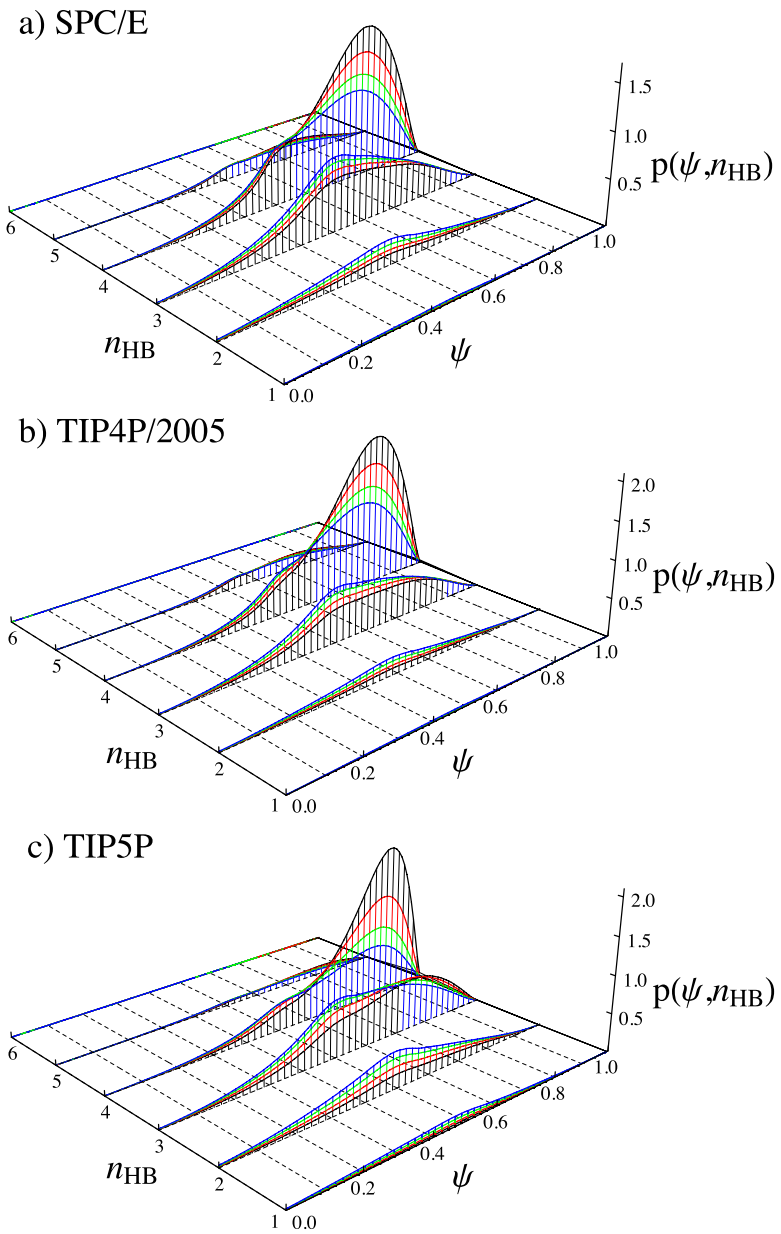

Figure 3.5.: Joint probability distribution $p(\psi, n_{\mathrm{HB}})$ of the number of hydrogen bonds n_{HB} and the tetrahedrality order parameter ψ for (a) SPC/E, (b) TIP4P/2005 and (c) TIP5P water at temperatures of $T = 278$ K (black), 298 K (red), 320 K (green) and 340 K (blue) and at a pressure of $p = 1$ bar.

3.3.3. Correlation functions

To gain information about spatial correlations of the different local water configurations, we define two-point correlation functions of the various local order parameters. In Fig. 3.6 a we show the normalized self-correlation function for the density

$$C_{\rho\rho}(r) = g(r) = \frac{\langle \rho(0)\rho(r)\rangle}{\rho^2}, \tag{3.12}$$

and the normalized self-correlation functions

$$C_{\psi\psi}(r) = \frac{\langle \psi(0)\psi(r)\rangle}{\langle \psi\rangle^2 \langle \rho(0)\rho(r)\rangle}, \tag{3.13}$$

and

$$C_{nn}(r) = \frac{\langle n_{\mathrm{HB}}(0)n_{\mathrm{HB}}(r)\rangle}{\langle n_{\mathrm{HB}}\rangle^2 \langle \rho(0)\rho(r)\rangle}, \tag{3.14}$$

of the tetrahedrality order parameter and the hydrogen bond numbers for the SPC/E water model at temperatures of $T = 278$, 298, 320 and 340 K. All correlation functions are normalized to unity at large separations. In addition, we normalize the functions $C_{\psi\psi}(r)$ and $C_{nn}(r)$ by the density density correlation function $C_{\rho\rho}(r)$ such that in the absence of variations in the tetrahedrality parameter ψ or hydrogen bond number n_{HB} the functions would be constant. In contrast to the density density correlation function $C_{\rho\rho}(r)$, the self-correlation functions $C_{\psi\psi}(r)$ and $C_{nn}(r)$ are quite featureless and thus show that there are only weak correlations between structural fluctuations. The weak correlations that one can discern decay to zero after ≈ 6 Å. Note that the small jump seen in the correlation function C_{nn} (indicated by a vertical arrow) is due to the HB cutoff radius $r_{\mathrm{HB}} = 0.35$ nm of the hydrogen bond criterium.

In Fig. 3.6 b the self-correlation functions $C_{\psi\psi}(r)$ and $C_{nn}(r)$ are compared with the cross-correlation functions

$$C_{\psi n}(r) = \frac{\langle \psi(0)n_{\mathrm{HB}}(r)\rangle}{\langle \psi\rangle\langle n_{\mathrm{HB}}\rangle\langle \rho(0)\rho(r)\rangle}, \tag{3.15}$$

$$C_{\rho\psi}(r) = \frac{\langle \rho(0)\psi(r)\rangle}{\langle \psi\rangle\langle \rho(0)\rho(r)\rangle} \tag{3.16}$$

and

$$C_{\rho n}(r) = \frac{\langle \rho(0)n_{\mathrm{HB}}(r)\rangle}{\langle n_{\mathrm{HB}}\rangle\langle \rho(0)\rho(r)\rangle}. \tag{3.17}$$

Not surprisingly, the self- and cross-correlation functions of the tetrahedrality parameter and the hydrogen bond number show similar behaviour, in line with the results

from Fig. 3.5 which point to a close correspondence between the two order parameters. We see that there are only weak spatial correlations between these two measures of the local water structure, in other words the degree to which a given water molecule is tetrahedrally ordered or hydrogen-bonded is only very weakly correlated to the structural ordering of a neighboring water molecule. Note that Fig. 3.5 tells us that the structural distribution functions are quite broad, so we learn that while structural fluctuations are pronounced, their spatial correlation is weak. Interestingly, the cross-correlation functions $C_{\rho\psi}$ and $C_{\rho n}$ between the density and the two structural order parameters exhibit even weaker correlations than the other correlation functions. In disagreement with the arguments brought forward in Ref. 20, we see that there is very little correlation between density and structural fluctuations, meaning in specific that features in $S(q)$ data unfortunately tell us very little about the spatial correlations of water structure. In Fig. 3.7 we show the normalized self- and cross-correlation functions of the density and the structural order parameters for the SPC/E, the TIP4P/2005 and the TIP5P water models for different temperatures. The qualitative behaviour does not differ much between the different water models. In agreement with previous findings [181], the TIP5P water model is slightly overstructured in comparison with the TIP4P/2005 and SPC/E water models.

3.4. Conclusion

In this chapter we showed that for several commonly used water models at temperatures above melting, there exist only weak spatial correlations between different structural order parameters. The typical range of structural correlations in Fig. 3.6 is consistent with a decay length on the order of 1 Å as observed in Ref. 167 for a coarse grained water model. The relation of such a decay length with a correlation length as inferred from an Ornstein-Zernike analysis of the structure factor is however far from clear [23]. We furthermore do not observe a pronounced spatial correlation between structural and density fluctuations, implying that features in the structure factor can not be interpreted in terms of or associated with structural properties, in contradiction to the assumptions made in Ref. 20 and in line with the results in Ref. 23. Errington et al. [166] report a reciprocal coupling between the tetrahedrality and the density in tetrahedrally ordered clusters in SPC/E water at low temperatures of $T = 220$ K and $T = 240$ K. That we find very weak spatial coupling between the density and the tetrahedral ordering in two-point correlation functions suggests that the clustering result of Errington et al. [166] involves multi-point correlations. At this point it is important to stress that the correlations we find between local density and structure are not totally absent, but they are rather much smaller than the density-density correlations (see Fig. 3.6). So whether one calls the density-structure correlation small or large depends on which reference one is using for comparison. Our results are consistent with the findings of Matsumoto [168], who observed no direct relation between the density anomaly and structural heterogeneities, but rather an interplay of monotonic hydro-

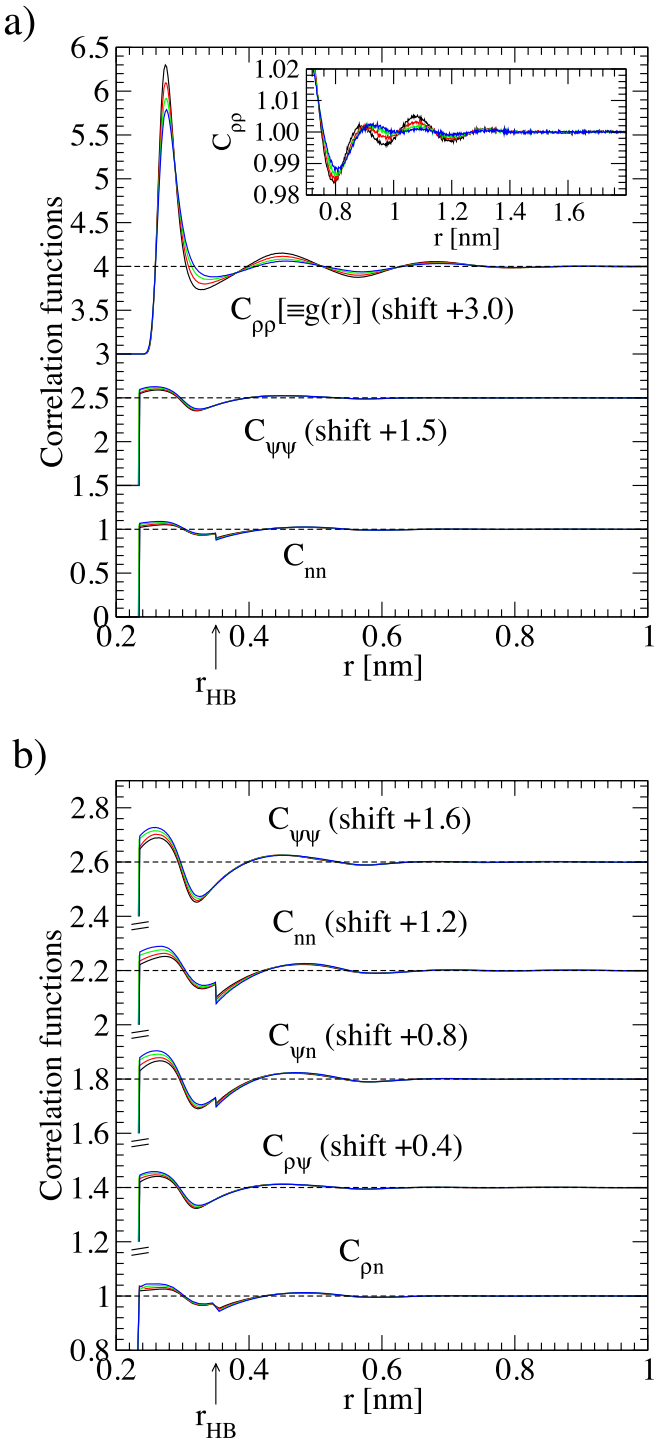

Figure 3.6.: (a) Self-correlation functions of density, $C_{\rho\rho}$, tetrahedrality order parameter, $C_{\psi\psi}$, and the number of hydrogen bonds, C_{nn}. The inset shows an enlarged view of the long range region of the density self-correlation function. (b) Comparison of the self- and cross-correlation functions of the density and the structural order parameters. For clarity some curves are shifted as indicated in the figure. All data is obtained by MD simulations of the SPC/E water model at temperatures of T = 278 K (black), 298 K (red), 320 K (green) and 340 K (blue) and at a pressure of $p = 1$ bar.

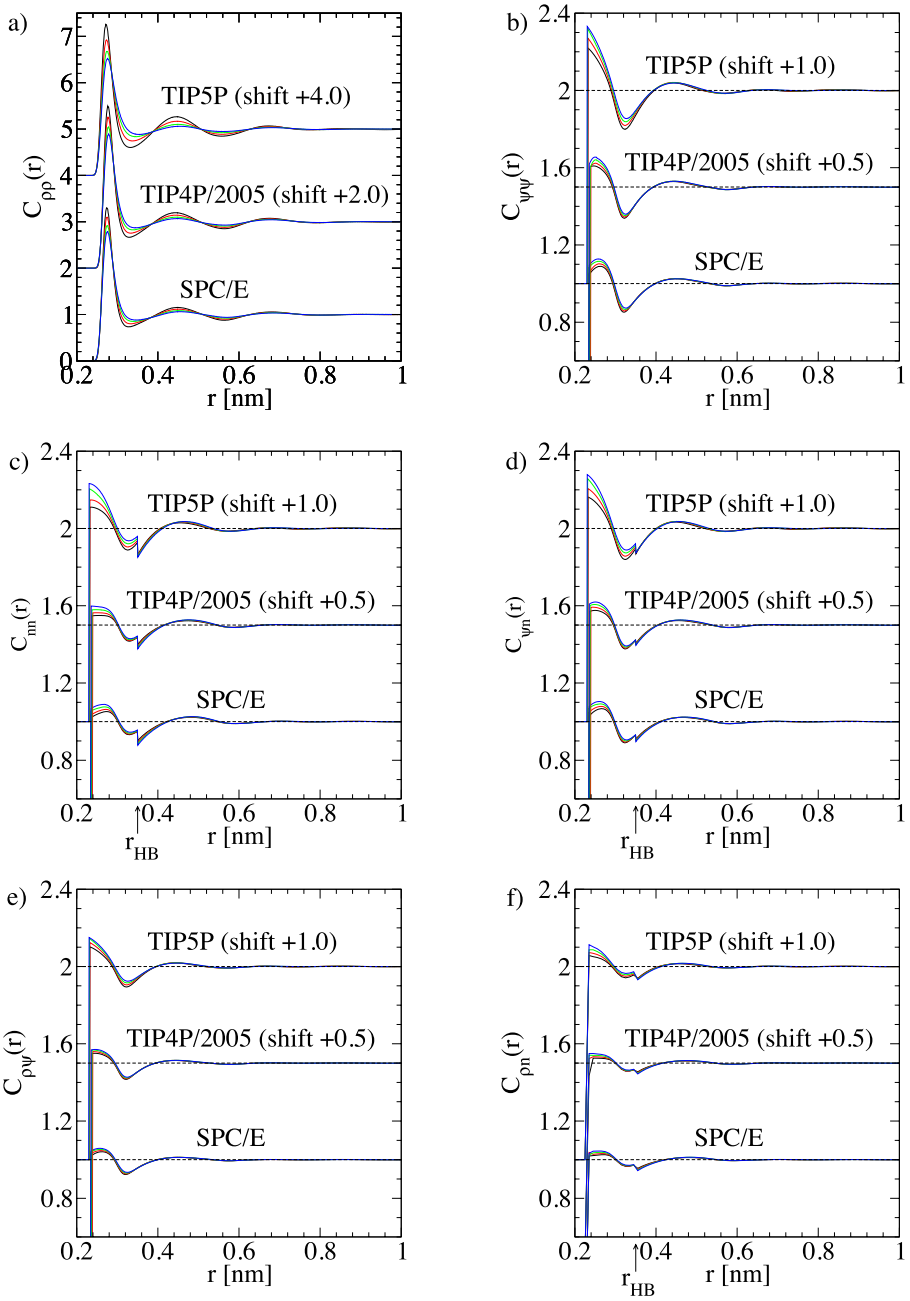

Figure 3.7.: Correlation functions of the density and the structural order parameters for the TIP5P, TIP4P/2005 and SPC/E water models at temperatures of $T = 278$ K (black), 298 K (red), 320 K (green) and 340 K (blue) and at a pressure of $p = 1$ bar. (a) Density density correlation function $C_{\rho\rho}$, (b) correlation function of the tetrahedrality order parameter $C_{\psi\psi}$, (c) correlation function of the number of hydrogen bonds C_{nn}, (d) cross correlation of the tetrahedrality order parameter and the hydrogen bond number $C_{\psi n}$, (e) cross correlation of the tetrahedrality order parameter and the density $C_{\rho\psi}$ and (f) cross correlation of the hydrogen bond number and the density $C_{\rho n}$. Arrows in graphs (c), (d) and (f) indicate the cutoff radius $r_{\mathrm{HB}} = 0.35$ nm of the hydrogen bond criterium. For clarity some curves are shifted as indicated in the graph.

gen bond extension and angular distortion in the network (see Fig. 3.4) upon cooling. While the spatially averaged values of the density and the hydrogen bonding network distortion are of course related, we show that their fluctuations are not strongly correlated in space. The picture of coexisting domains of differently structured water is not supported by an analysis of the respective two-point correlation functions. Such correlations might grow as temperature is lowered into the metastable liquid regime below melting and one approaches the liquid-liquid critical point, which, however, is not focus of the present work.

We also show that the experimentally well documented minimum in the structure factor at small wave vector q, which has very recently been seen in simulations of TIP4P-Ew water [23], is obtained with different simple water models, suggesting that this is a quite robust feature, which in fact is related to the interplay of attractive and repulsive forces [22, 186]. Finally, let us stress that we are not claiming that classical water models can accurately describe all aspects of water structure, however, the low-q behavior of $S(q)$ does not constitute a serious hurdle for current classical water models.

CHAPTER 4

ENTROPY AND ENTHALPY CONVERGENCE BEYOND THE HARD SPHERE MODEL

4.1. Introduction

4.1.1. Motivation

The question of protein folding and stability is one of the fundamental problems in biology [187]. Despite intense scientific efforts since Anfinsens pioneering work [188] it is not yet completely clear what the dominant forces are, that govern protein stability [53, 189]. The hydrophobic effect has long been suspected to play a major role [56]. It was therefore seen as a major breakthrough, when the observation of convergence of the denaturation entropy per residue of a whole class of proteins at a universal temperature allowed to draw a close analogy with the solvation properties of simple hydrophobic compounds [66, 67].

It was first observed by Privalov and Khechinashvili [64, 65], that the entropies and enthalpies of denaturation per residue for a number of proteins, if extrapolated to high temperatures, converge to a common value at a temperature near $T_S^* \approx T_H^* \approx 110^\circ$ C. Baldwin [61] noticed, that at roughly the same temperature the entropy of dissolution of several liquid hydrocarbons [190] extrapolates to zero (while the convergence temperature of the solvation enthalpy is much lower). A similar convergence has been observed [66, 67] for the dissolution of saturated hydrocarbon gases [47, 191–194], noble gases [47–49], cyclic dipeptides [62, 195] and gaseous alcohols [196]. These observations stirred an intense discussion about the interpretation and implications of these findings for the role of the hydrophobic effect in protein folding [62, 63, 67, 68, 196–198], which we will summarize briefly further below.

Theoretically, the temperature dependence of hydrophobic hydration has been studied by various methods [43, 71–73, 75, 199–208], mostly focussing on the solvation of simple model solutes such as hard spheres [43, 72, 73, 75, 200–202, 204] or Lennard-Jones particles [71, 199, 203, 206, 208]. Using a Gaussian model for particle number

fluctuations in atomic-scale cavities in conjunction with simulated water radial distribution functions, convergence temperatures of about $T_S^* \approx 400$ K for small hard-sphere solutes of different radii, close to the experimental results, were obtained [72, 73, 75]. The model allowed a simple interpretation of this phenomenon in terms of particle number fluctuations, water density variation, and to a limited extent the isothermal compressibility of water [72, 73]. Results from the revised scaled-particle theory [43] show, that the convergence temperature T_S^* for larger sphere radii starts to depend on the size of the solutes, but for typical solute radii around 3 Å convergence temperatures in the range $\approx 370 - 400$ K are observed.

Despite this seemingly good agreement of the entropy convergence temperatures obtained from theoretical models for hard-sphere solvation with the experimental results for both proteins and simple hydrophobic compounds, a few open questions remain:

i) For simple hydrophobic compounds, the convergence temperatures of solvation entropy and enthalpy widely differ, the latter being lower by typically 100°, while the putative entropy and enthalpy convergence temperatures for proteins are the same [61, 67]. To account for this, it is assumed that the solvation of hydrophilic groups contributes to the enthalpy but not to the entropy, so that the solvation entropies of proteins and hydrophobic compounds are similar but not the enthalpies [68]. In contradiction to this assumption and not surprisingly, we find a continuous change of the solvation entropy as one goes from hydrophobic to hydrophilic solutes and in all cases the solvation entropy does not strictly vanish.

ii) The theoretically predicted convergence of hard-sphere solvation entropies at about 400 K was obtained based on simulation results for SPC water simulated at the experimental liquid-vapor coexistence density [72]. As we show in this work, at ambient pressure of 1 bar, which seems the relevant condition when comparing to protein data, the entropy convergence temperature for hard-sphere solvation goes down to 340 K, in disagreement with both protein and simple hydrocarbon data.

iii) Perhaps most strikingly, Robertson and Murphy [69] showed, that for a larger set of proteins neither entropy nor enthalpy convergence is observed (see Fig. 4.1, circles), although the polar and non-polar surface areas per residue, that are buried upon folding, show the same trends as for the smaller set of proteins originally studied (denoted by triangles) [67].

4.1.2. Outline

In this chapter we do not directly consider protein denaturation thermodynamics, but rather investigate the solvation of a more general class of spherical solutes. It has been shown, that attractive solute-water interactions have a pronounced influence on the solvation thermodynamics [71, 75, 202, 203, 207]. We therefore systematically study the dependence of the entropy and enthalpy convergence temperature for spherical solutes on the solute-water interaction potential. We use a Buckingham double exponential potential with four free parameters to vary the stiffness of the repulsive part, the range and strength of the attractive part of the interaction as well as the solute

radius independently. Solvation free energies are obtained from molecular dynamics (MD) simulations by the particle insertion method. We mainly use the popular extended simple point charge (SPC/E) water model, but also compare our results with the simple point charge (SPC) and the TIP5P parameters to check the influence of the water model [206, 208] on the solvation properties.

In Sec. 4.2, we review basic notions of thermodynamic convergence of solvation and protein denaturation, in Sec. 4.3, we introduce the main concepts using the example of hard-sphere solutes. In Sec. 4.4, we discuss the dependence of the entropy and enthalpy convergence on the solute-water interaction details and the water model employed. In Sec. 4.5, we summarize and conclude.

4.2. Thermodynamics of convergence

Assuming a temperature independent heat capacity change ΔC_p upon solvation of a solute or denaturation of a protein, from $T\partial\Delta S/\partial T = \Delta C_p$ and $\partial\Delta H/\partial T = \Delta C_p$, the entropy and enthalpy changes follow as [209]

$$\Delta S(T) = \Delta S(T_0) + \Delta C_\mathrm{p} \ln\left(\frac{T}{T_0}\right), \tag{4.1}$$

and

$$\Delta H(T) = \Delta H(T_0) + \Delta C_\mathrm{p}\left(T - T_0\right), \tag{4.2}$$

where T_0 is an arbitrary reference temperature. We will show, that this assumption is approximately true for the systems studied by us. If entropy convergence occurs at a temperature denoted by T_S^* for a group of species, then a plot of $\Delta S(T)$ versus ΔC_p at a fixed temperature T yields a straight line, whose slope $\ln(T/T_S^*)$ is determined by the convergence temperature T_S^* and whose intercept $\Delta S(T_S^*)$ gives the entropy change at the convergence temperature [67]. Similarly, a plot of ΔH versus ΔC_p yields a straight line with the slope $T - T_H^*$ and intercept ΔH^*, if enthalpy convergence is observed. Note that such a plot allows to extract the convergence temperature and the convergence entropy or enthalpy based on the assumption of a constant heat capacity in a straightforward manner (but it does not allow to check wether the heat capacity is actually constant). In Fig. 4.1 we show such a plot for the original set of proteins [66] used in the analysis of Murphy et al. [67] (open triangles) including a linear fit to the data. The data indicated by the filled triangle, corresponding to the denaturing of the protein parvalbumin, was listed in Ref. 66 (see Table I of Ref. 66) but neither included in the data fitting nor in the graph of Ref. 67. Note that the data in this plot has been extrapolated from the denaturing temperature by assuming the relations Eqs. 4.1 and 4.2 to hold, an assumption which for proteins is in general difficult to validate since the denaturing temperature can only be varied by adding denaturant or pH change (and thus possibly causing side effects) in a restricted range.

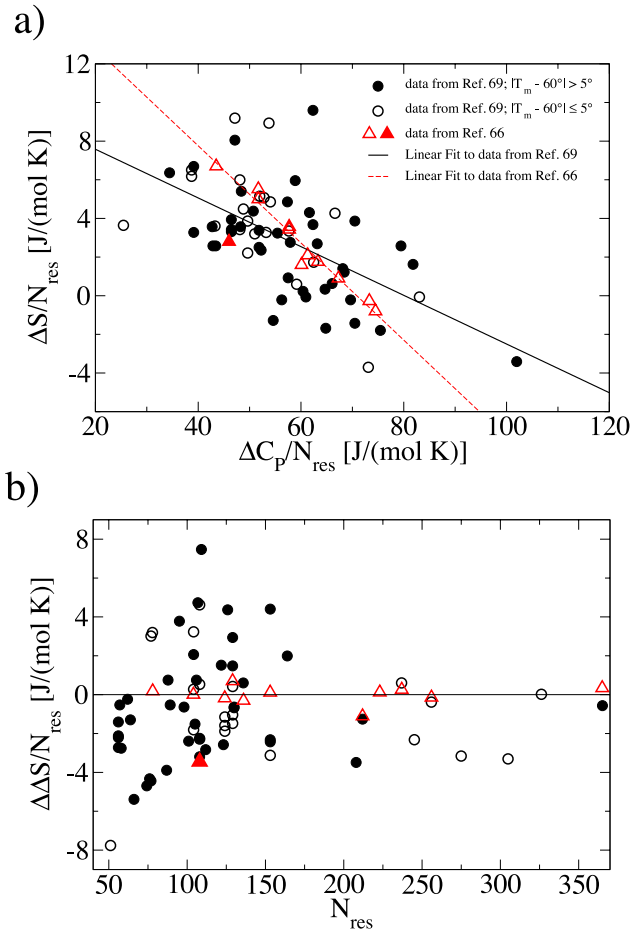

Figure 4.1.: (a) Entropy change ΔS plotted against the change in isobaric heat capacity ΔC_p upon denaturation per residue extrapolated to 25° C for different sets of proteins. The small set (triangles) is taken from Ref. 66. Open triangles denote the proteins, that have been used in the analysis of Ref. 67 to argue for the occurrence of entropy convergence in protein denaturation. The data point for parvalbumin (filled triangle) was included in the data set of Ref. 66 (see Table I of Ref. 66) but not shown in the graph and not considered in the data fitting of Ref. 67. The data for the larger set of proteins (circles) is taken from Ref. 69. This set is separated into proteins with denaturation temperatures T_m in the interval $55°C < T_\mathrm{m} < 65°C$ (open circles) and T_m outside this interval (filled circles). The black line is a linear fit to the data set of Ref. 69, the dashed line to the open triangles. (b) Deviation $\Delta\Delta S$ of the unfolding entropy per residue from the linear fit for the small set (dashed line in (a)) as a function of the number of residues N_res of the proteins. No systematic trend as a function of the protein size is seen. Also, there is no qualitative difference between the set of proteins with a denaturation temperature close to 60° C (open circles) and far away from 60° C (filled circles).

Murphy and Gill [62, 63] and Lee [68] showed that convergence of some thermodynamic observable, e. g. the entropy of denaturation of a set of proteins or the entropy of dissolution ΔS within a homologous series of compounds, can generally be expected if that observable is linearly dependent on the variable X (e.g. the number of hydrophobic groups in a homologous series of hydrocarbons) which distinguishes the elements of the series,

$$\Delta S(T) = \Delta S_R(T) + X\Delta S_X(T), \tag{4.3}$$

where $\Delta S_X(T)$ is the entropy change associated with the variable X and ΔS_R is the residual entropy change due to the molecular parts that are common within the series. From the relation $C_p = T\partial S/\partial T$ we obtain a linear dependence of the heat capacity change on X,

$$\Delta C_p = \Delta C_R + X\Delta C_X \tag{4.4}$$

where we assume all heat capacity contributions to be independent of temperature. Then, by eliminating X from Eqs. 4.3 and 4.4, we obtain

$$\Delta S(T) = \Delta S_R(T) + (\Delta C_p - \Delta C_R)\frac{\Delta S_X(T)}{\Delta C_X}, \tag{4.5}$$

i. e., a linear dependence of $\Delta S(T)$ on ΔC_p. A sufficient condition for both Eqs. 4.3 and 4.4 is the linear dependence of the free energy change ΔF on X [68]. The argument presented above is equivalent to the earlier observation of Sturtevant [210], that the ratio of entropy change and heat capacity change upon dissolution of several hydrophobic compounds is constant. Comparison with Eq. 4.1 shows, that the convergence temperature, given by the slope,

$$\ln\left(\frac{T}{T_S^*}\right) = \frac{\Delta S_X(T)}{\Delta C_X}, \tag{4.6}$$

depends solely on quantities associated with the variable X. Equation 4.5 further implies, that the entropy at convergence is equal to the residual entropy, $\Delta S(T_S^*) = \Delta S_R(T_S^*)$. Therein lies the importance of convergence phenomena, since they enable one to separate different contributions to the observable under study.

In the case of protein denaturation it is not a priori clear, what the distinguishing variable X is and therefore how the observed convergence should be interpreted [62, 63, 67, 68, 196]. Murphy et al. [63, 67, 211] argue, that for globular proteins the polar surface area per residue that is exposed to water upon unfolding is constant, while the non-polar surface area per residue varies and thus is taken proportional to X [211, 212]. This implies, that the contribution of the non-polar protein surface vanishes at T_S^*, while the residual entropy is due to solvation of polar groups and configurational entropy, and corroborates the analogy with the dissolution of other hydrophobic compounds [61, 67]. Accordingly, the similar convergence temperature

for the different compounds is taken as an universal feature of hydrophobic hydration [63, 67, 196]. Lee [68] originally suggested a slightly different assignment, normalizing the unfolding entropy by the buried surface area instead of the number of residues and taking the fraction of non-polar surface area exposed upon unfolding as the variable X. In that case the convergence is observed at the temperature, at which the polar and non-polar contributions to the entropy are equal. Both approaches essentially can be viewed as different definitions of the hydrophobic contribution to denaturation [211].

One notes that the mechanism for entropy convergence discussed in Eqs. 4.3 - 4.6 obviously rests on the assumption of additivity of the contributions of individual chemical groups to the total solvation entropy and enthalpy, an assumption which has been independently verified [191, 213, 214]. The other, more serious, assumption is that it is sufficient to sort the solvation contributions of all chemical groups into just two groups, hydrophilic and hydrophobic, characterized by the variable X, an assumption which we show not to be entirely true in this work. In fact, the concept of entropy convergence treated theoretically by the information theory approach and revised scaled particle theory in some sense goes beyond the additivity concept outlined above [62, 63, 68], since here it is shown that the entropy of solvation of hard spheres converges to a universal value at one temperature for a whole range of different sphere radii. The importance of this observation lies in the fact that the hydrophobic groups that are solvated when a protein denatures in general have different radii. However, the convergence entropy is non-zero for hard-sphere solvation, so that according to the assignment of Lee [68] one will in general not find a unique temperature where the hydrophobic contributions to the solvation entropy cancel the polar contributions for different proteins. Even more importantly, individual amino acids differ in more properties than just their radii, since details of the solute-water potential are expected to vary between different species, which adds additional variation to the expected convergence temperatures. Again, all these reservations serve to explain that entropy convergence for protein denaturation is not really expected, in accord with actual experimental observations (see the complete set of protein data in Fig. 4.1) [69].

The convergence of solvation entropies and enthalpies of liquid hydrocarbons (e.g. alkanes) simply reflects the additivity of solvation of individual linked methyl groups and thus is not really related to the main point of this work. An additional complication comes in because transfer studies from liquid hydrocarbons to aqueous solution (as well as protein denaturation studies) involve the liquid (or protein core) reference state, which is difficult to treat theoretically. Such complications are obviously absent for solvation studies with noble or hydrocarbon gases, which are more closely related to our calculations. In this respect it is important to realize that the entropy convergence of noble gases is far from perfect [43], a fact that is very much in line with our findings.

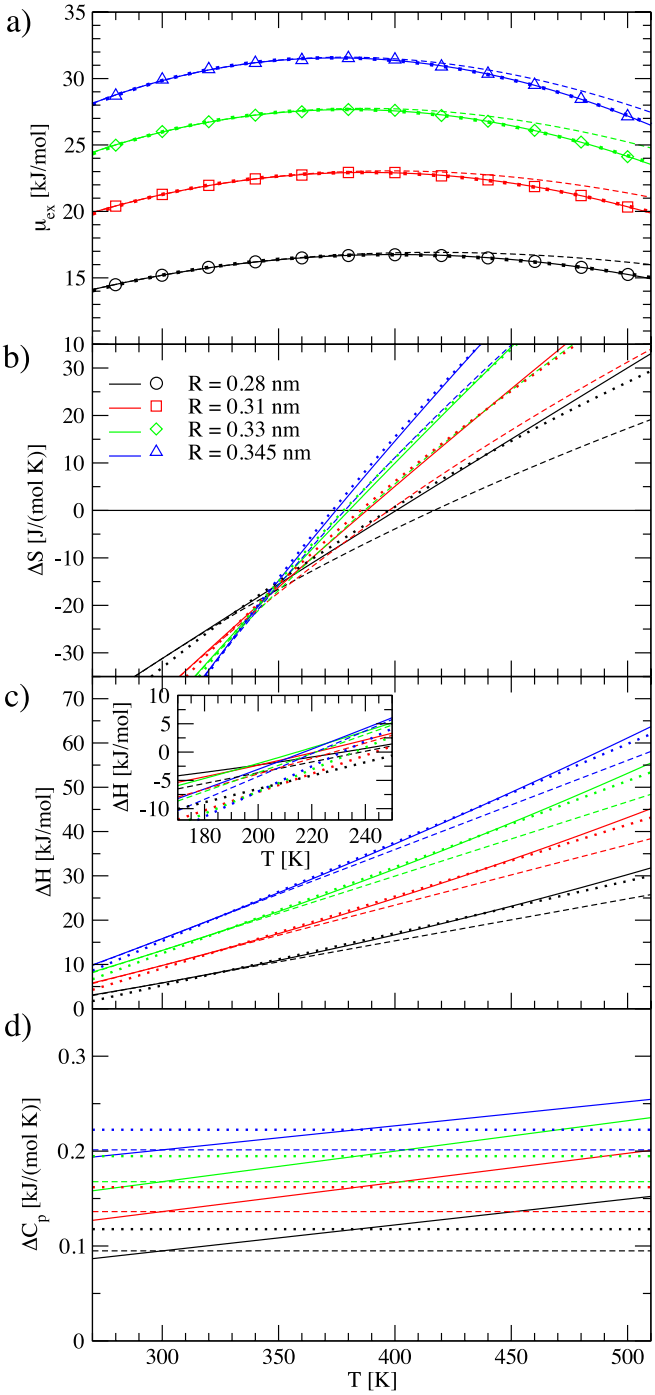

Figure 4.2.: (a) Excess chemical potential μ_{ex}, (b) entropy ΔS, (c) enthalpy ΔH and (d) isobaric heat capacity ΔC_p of differently sized hard core solutes in SPC/E water as a function of the temperature. The solutes have radii of 0.28 nm (circles, black lines), 0.31 nm (squares, red lines), 0.33 nm (diamonds, green lines) and 0.345 nm (triangles, blue lines), corresponding roughly to the size of neon, argon, methane and xenon. Excess chemical potentials are determined by test particle insertion (symbols). Solid lines are obtained by full fits of μ_{ex} according to Eq. 4.7 and using Eqs. 4.8-4.10. Dotted lines are fits of μ_{ex} under the constraint of constant ΔC_p, that is $c = 0$. Dashed lines are obtained by extrapolation, using Eqs. 4.1 and 4.2, from the reference temperature $T_0 = 300$ K with $\Delta S(T_0)$, $\Delta H(T_0)$ and $\Delta C_p(T_0)$ taken from the full fit. The trajectories for the particle insertion are obtained from MD simulations of 895 SPC/E water molecules at constant pressure $p = 1$ bar.

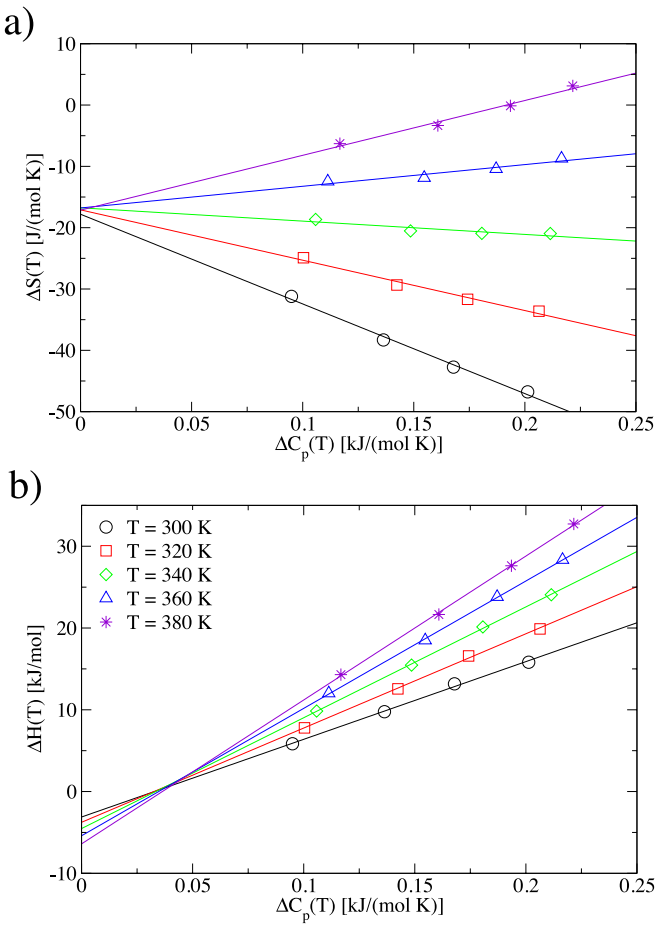

Figure 4.3.: (a) Solvation entropy $\Delta S(T)$ and (b) solvation enthalpy $\Delta H(T)$ of hard core solutes of varying size as a function of the heat capacity change $\Delta C_p(T)$ for different reference temperatures $T = 300$, 320, 340, 360 and 380 K. Data for entropies, enthalpies and heat capacity changes are obtained from fits to the particle insertion data according to Eqs. 4.7-4.9. Solid lines show linear fits to the data according to Eqs. 4.1 and 4.2. The resulting convergence temperatures, entropies and enthalpies are summarized in Tab. 4.1. All data is obtained for SPC/E water at $p = 1$ bar.

4.3. Hard-core solutes

In this work we determine the solvation free energy $\Delta F = \mu_{\text{ex}}$ as a function of the temperature for solutes with four different radii $R = 0.28$, 0.31, 0.33 and 0.345 nm, as used by Garde et al. [72] to model solvation of neon, argon, methane and xenon, and various potential shapes (see Eq. 2.1 and the following text). Figure 4.2 a shows the solvation free energies obtained by particle insertion (symbols) for hard core solutes in SPC/E water. In qualitative agreement with previous results [72], μ_{ex} has a maximum around 380 K. We fit the data by the form,

$$\mu_{\text{ex}}(T) = a + b\,T - c\,T^2 - d\,T\ln(T), \tag{4.7}$$

leading to the solvation entropy, $\Delta S = -\partial\mu_{\text{ex}}/\partial T$,

$$\Delta S(T) = d - b + 2c\,T + d\ln(T), \tag{4.8}$$

the solvation enthalpy, $\Delta H = \mu_{\text{ex}} + T\Delta S$,

$$\Delta H(T) = a + d\,T + c\,T^2, \tag{4.9}$$

Table 4.1.: Convergence temperatures T_S^* and T_H^*, entropies ΔS^* and enthalpies ΔH^* obtained from the plots shown in Fig. 4.3 for different reference temperatures T.

T [K]	T_S^* [K]	ΔS^* [J/(mol K)]	T_H^* [K]	ΔH^* [kJ/mol]
300	347.2	-17.8	205.0	-3.1
320	347.4	-17.1	204.7	-3.8
340	347.5	-16.8	204.5	-4.5
360	347.5	-16.8	204.2	-5.4
380	347.5	-17.1	204.0	-6.4

and a linearly varying heat capacity increment

$$\Delta C_p = d + 2c\ T, \tag{4.10}$$

see Fig. 4.2. To estimate how relevant the temperature dependence of the heat capacity is, we compare in Fig. 4.2 fit results using the full expression (shown by solid lines) with constrained fits where the heat capacity is forced to be constant and thus $c = 0$ (dotted lines in Fig. 4.2). We find the fits with $c = 0$ to be of acceptable quality, which is in line with the fact that the actual heat capacity variation with temperature is small. This is quite important in light of the common assumption of a constant heat capacity used for extrapolating experimental solvation data. To check this procedure explicitly, we extrapolate $\mu_{\text{ex}}(T)$, $\Delta S(T)$ and $\Delta H(T)$, using Eqs. 4.1 and 4.2 with a reference temperature $T_0 = 300$ K, where we extract values for $\Delta S(T_0)$, $\Delta H(T_0)$ and $\Delta C_p(T_0)$ from the full fit. The resulting extrapolated curves (dashed lines) differ from the full fits for high temperatures, but otherwise the accuracy seems acceptable. The entropy shows convergence at a temperature around $T_S^* \approx 350$ K, regardless of the method used to fit the data, which is gratifying as most experimental convergence temperatures are obtained via extrapolation. The value for T_S^* is significantly lower than the convergence temperature of about $T_S^* \approx 400$ K found previously for hard-spheres in SPC water [72]. We will discuss the origin of this discrepancy in detail further below but briefly mention here that it has to do with the different densities at which the simulations in [72] have been performed. The enthalpy convergence temperature lies outside the studied temperature range and occurs at roughly $T_H^* \approx 205$ K. The difference in convergence temperature of about $T_S^* - T_H^* \approx 140$ K is in rough agreement with experiments for simple liquid hydrocarbons, which give $T_S^* \approx 380$ K and $T_H^* \approx 290$ K, but there is a significant shift and we note that convergence in hydrocarbons occurs at vanishing entropy and enthalpy [61]. This is due to the fact that for homologous alkanes, convergence is mostly a consequence of additivity. For noble gases the entropy converges also around $T_S^* \approx 380K$, but the convergence entropy is non-zero. We will come back to this issue further below.

In Fig. 4.3 we plot the solvation entropy $\Delta S(T)$ and the solvation enthalpy $\Delta H(T)$ as a function of the heat capacity change $\Delta C_p(T)$ for several different reference temperatures $T = 300$, 320, 340, 360 and 380 K. The convergence temperatures T_S^* and T_H^* and the entropies ΔS^* and enthalpies ΔH^* at convergence are summarized in Tab. 4.1. For the entropy, the resultant numbers do not depend significantly on the reference temperature T and agree very well with what one directly reads off from Fig. 4.2. For the enthalpy, the individual linear fits in Fig. 4.3 are excellent, but the resulting convergence temperatures T_H^* and convergence enthalpies $\Delta H(T)$ depend quite a bit on the reference temperature chosen. This is in line with the fact that the enthalpy data show less pronounced convergence when compared to the entropy, see Fig. 4.2. This shows clearly that a plot of $\Delta S(T)$ or $\Delta H(T)$ versus $\Delta C_p(T)$ can be quite misleading, since if the heat capacity change is not independent of the temperature the values for the convergence temperature and convergence thermodynamic quantity depend considerably on the reference temperature chosen.

In all what follows we use the full expression Eq. 4.7 with a temperature dependent heat capacity change to fit the particle insertion data. As a simple definition for the convergence temperature T_S^* we take the temperature at which the entropies of solutes with radii $R = 0.28\,\mathrm{nm}$ and $R = 0.345\,\mathrm{nm}$ intersect, that is

$$\Delta S^{R=0.28\,\mathrm{nm}}(T_S^*) = \Delta S^{R=0.345\,\mathrm{nm}}(T_S^*). \tag{4.11}$$

The enthalpy convergence temperature T_H^* is defined analogously. We note that the convergence temperature depends systematically on the solute sizes that are compared [43], so our definition only makes sense for the restricted range of radii actually considered by us.

4.4. Influence of the solute-water interaction

4.4.1. Stiffness of the repulsion

We first investigate the effect of the stiffness of the repulsive part of the potential, which is determined by the decay length $1/B$. For this purpose, we study purely repulsive solutes (i.e. $C = 0$ in Eq. 2.1) with repulsion decay lengths in the range of $1/B = 0.005 - 0.03\,\mathrm{nm}$ and compare with hard core solutes. Figure 4.4 a shows the excess chemical potential of a solute of radius $R = 0.33\,\mathrm{nm}$ for different values of the decay length $1/B$ (circles, full lines) and for a hard core potential (squares, dashed line). This radius roughly corresponds to a methane molecule and is - because of the additivity of solvation properties - also relevant for alkane chains. It is seen that the solvation free energy curves are systematically shifted downwards for increasing potential stiffness, the stiffer the potential the less unfavorable the solvation process. This effect is more pronounced at small temperatures, leading to a shift of the free energy maxima to higher temperatures as indicated by the dashed-dotted line. The corresponding solvation entropies are shown in Fig. 4.4 b. For increasing potential stiffness

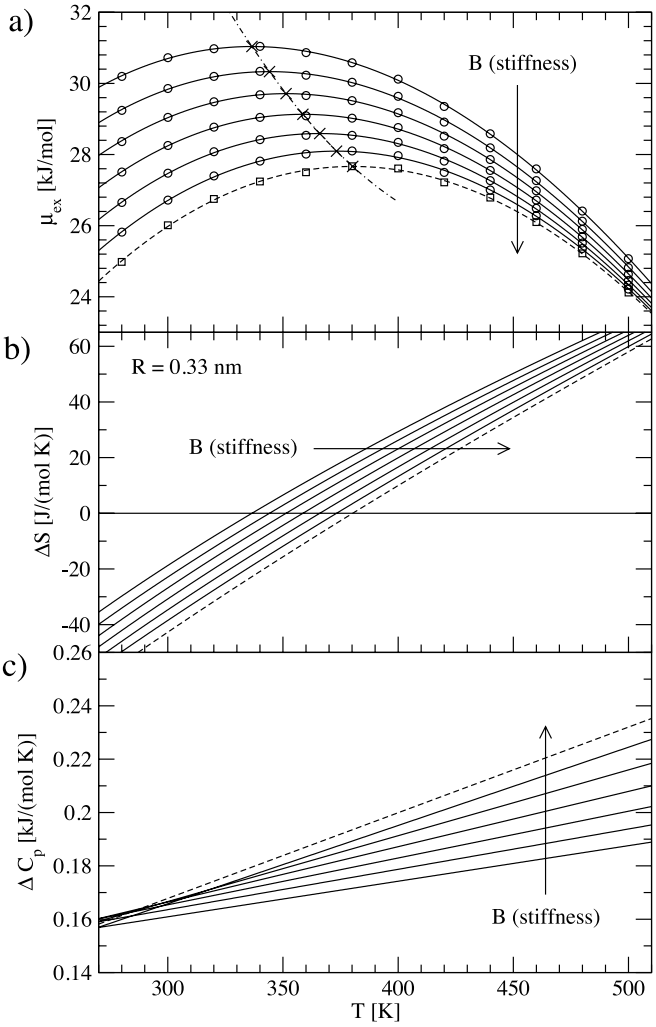

Figure 4.4.: (a) Excess chemical potential, (b) solvation entropy and (c) heat capacity change upon solvation of purely repulsive spherical solutes of radius $R = 0.33\,\mathrm{nm}$ for varying repulsion decay length $1/B = 0.005$, 0.01, 0.015, 0.02, 0.025 and 0.03 nm (circles, full lines) and a hard core solute of the same radius (squares, dashed lines) as a function of the temperature. The symbols are results from particle insertion. Lines are fits to the data according to Eqs. 4.7 - 4.10. The crosses in (a) mark the positions of the maxima of the chemical potentials and the dashed-dotted line is a quadratic fit. The trajectories for the particle insertion are obtained by MD simulations of the SPC/E water model at a constant pressure of $p = 1\,\mathrm{bar}$.

they are shifted towards higher temperatures, while the temperature dependence of the heat capacity in Fig. 4.4 c becomes more pronounced with increasing potential stiffness. One notes, that there is no crossing of the curves, i. e., for solutes characterized by same radii but different stiffness one does not find entropy convergence. The entropy shifts have a pronounced influence on the convergence temperature, as shown in Fig. 4.5. For increasing stiffness the convergence is shifted to higher temperatures, reaching a value of $T_S^* = 347\,\mathrm{K}$ for the limiting case of a hard core solute already shown in Fig. 4.2. Actual interaction potentials between solutes and water are far from the hard-core limit. For a realistic value of $1/B = 0.03\,\mathrm{nm}$ the convergence temperature is $T_S^* = 314\,\mathrm{K}$. This temperature is even farther away from the experimentally observed value of $T_S^* \approx 385\,\mathrm{K}$ for noble gases and proteins [67]. In essence, we see that a certain softness of the repulsive part of the solute-water interaction is relevant as it significantly shifts the convergence temperature to lower temperatures, but this

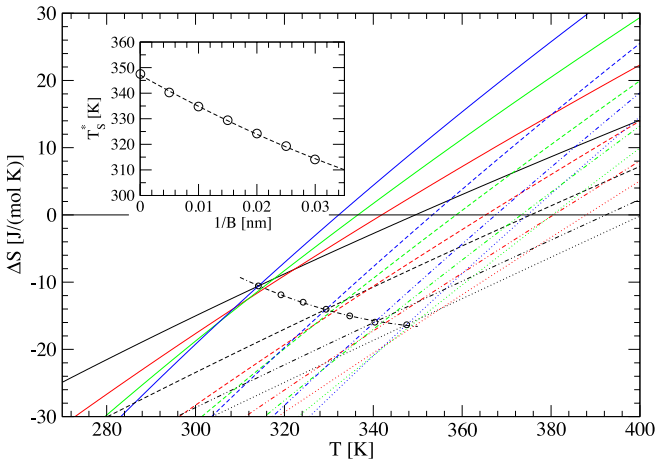

Figure 4.5.: Solvation entropies for purely repulsive solutes of varying size $R = 0.28\,\text{nm}$ (black), $0.31\,\text{nm}$ (red), $0.33\,\text{nm}$ (green) and $0.345\,\text{nm}$ (blue) and varying potential stiffness $1/B = 0.03\,\text{nm}$ (solid lines), $0.015\,\text{nm}$ (dashed lines), $0.005\,\text{nm}$ (dashed-dotted lines) and hard core (dotted lines) in SPC/E water at constant pressure $p = 1\,\text{bar}$. Circles indicate the intersection of the entropies of solutes with radii $R = 0.28\,\text{nm}$ and $R = 0.345\,\text{nm}$ for the same values of the potential stiffness as shown in Fig. 4.4 (not all entropy curves are shown). In the inset the convergence temperature defined by Eq. 4.11 is shown as a function of the repulsion decay length $1/B$.

realistic feature does not improve the comparison with the experimental convergence temperature. We will later see that an attractive component to the interaction will bring the convergence temperature up again.

4.4.2. Water models

Here, we investigate the origin of the discrepancies of our particle insertion simulation results, obtained with SPC/E water so far, with previous theoretical results, based on information theory in conjunction with simulations for SPC water [72]. Figures 4.6 a and b show the solvation free energies and entropies for hard core solutes of varying size in SPC/E, SPC and TIP5P water including the information theory results of Ref. 72. Our data for the three different water models indicated by solid lines are all obtained by particle insertion simulations at ambient pressure of $p = 1$ bar. While the excess chemical potentials agree rather well for temperatures around 300 K, they differ significantly at higher temperatures, which leads to a considerable spread in the resulting entropy convergence temperatures by about 30 K in Fig. 4.6 b. The data from Ref. 72, shown by the orange dashed lines, was obtained by the information theory approach based on SPC simulations at densities corresponding to the experimental vapor-liquid coexistence curve of water. The deviations from all the other data at $p = 1$ bar is significant. To understand the reason for this deviation, we resimulated SPC water at densities that match the experimental liquid-vapour coexistence densities and used

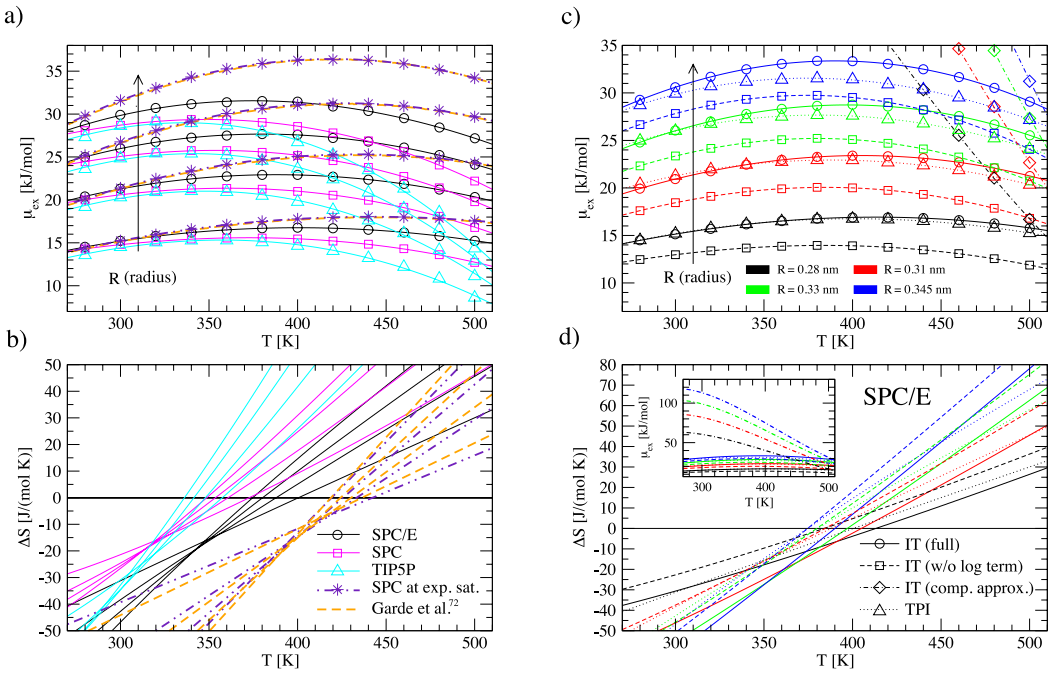

Figure 4.6.: (a) Excess chemical potentials μ_{ex} and (b) solvation entropies of hard core solutes of varying size $R = 0.28$, 0.31, 0.33 and 0.345 nm for different water models. Symbols show the data obtained from particle insertion for the SPC/E (circles, black), the SPC (squares, magenta) and the TIP5P (triangles, cyan) water model, solid lines are obtained by fits to the particle insertion data according to Eq. 4.7 and 4.8. All simulations are performed at a constant pressure of $p = 1$ bar. For comparison the information theory (IT) results of Garde et al. [72] (orange dashed lines) and our own IT results for SPC water simulated at the densities of the experimental saturation curve (purple stars and double-dotted dashed lines) are also included. (c) Comparison of the chemical potential obtained by the information theory model (see Eq. 4.12) including (circles and full lines) and neglecting (squares and dashed lines) the logarithmic term, the compressibility approximation (Eq. 4.15) (diamonds and dashed-dotted lines) and the results from the particle insertion (triangles and dotted lines) for SPC/E water at a constant pressure of $p = 1$ bar. Lines are fits to the data points. The inset in (d) shows the fits to μ_{ex} on a larger scale. (d) Comparison of the solvation entropies obtained by the temperature derivative of the fits to the chemical potentials shown in (c). Line styles have the same meaning as in (c).

Table 4.2.: Isothermal compressibility κ_T of the SPC/E water model at a pressure of $p = 1$ bar for varying temperature. The compressibilities are obtained from MD simulations by a numerical derivative according to Eq. 3.6. Error estimates are obtained by a block averaging algorithm.

T [K]	κ_T [10^{-11} Pa^{-1}]
278	44.32 ± 0.17
298	45.50 ± 0.17
320	48.23 ± 0.19
340	51.53 ± 0.20
360	55.91 ± 0.25
380	61.61 ± 0.28
400	69.10 ± 0.44
420	78.66 ± 0.96

the same information theory approach, the results are shown by purple stars and lines. The agreement with the previous IT approach is perfect, yet, the disagreement with the other simulations still needs to be explained.

To that end, let us briefly reconsider the information theory model for the solvation of hard core solutes [72–74]. It relates the excess chemical potential μ_{ex} of a hard-core solute to the solvent particle number fluctuations inside a cavity of the size and shape of the solute, assuming Gaussian fluctuations. Using a continuous Gaussian approximation for the particle number distribution, the excess chemical potential follows as

$$\mu_{\text{ex}}^{IT} = k_{\text{B}}T\rho^2 v^2/2\langle\delta n^2\rangle + k_{\text{B}}T\ln(2\pi\langle\delta n^2\rangle)/2, \tag{4.12}$$

where ρ is the number density of the solvent, v is the volume of the cavity, $\delta n = n - \langle n\rangle$, and n is the number of solvent particles inside the randomly placed cavity. The second moment of the particle number fluctuations, $\langle\delta n^2\rangle$, is related to a double integral over the oxygen-oxygen radial distribution function $g_{\text{OO}}(r)$ by

$$\langle n(n-1)\rangle = \rho^2 \int_v d^3r \int_v d^3r' g_{\text{OO}}\left(|\vec{r} - \vec{r}'|\right), \tag{4.13}$$

which thus yields a straightforward way to evaluate the expression Eq. 4.12 based on simulation results for the distribution function $g_{\text{OO}}(r)$. In the thermodynamic limit, i.e. for infinite cavity volume v, the relation

$$\frac{\langle\delta n^2\rangle}{\langle n\rangle} = \rho k_{\text{B}}T\kappa_T \tag{4.14}$$

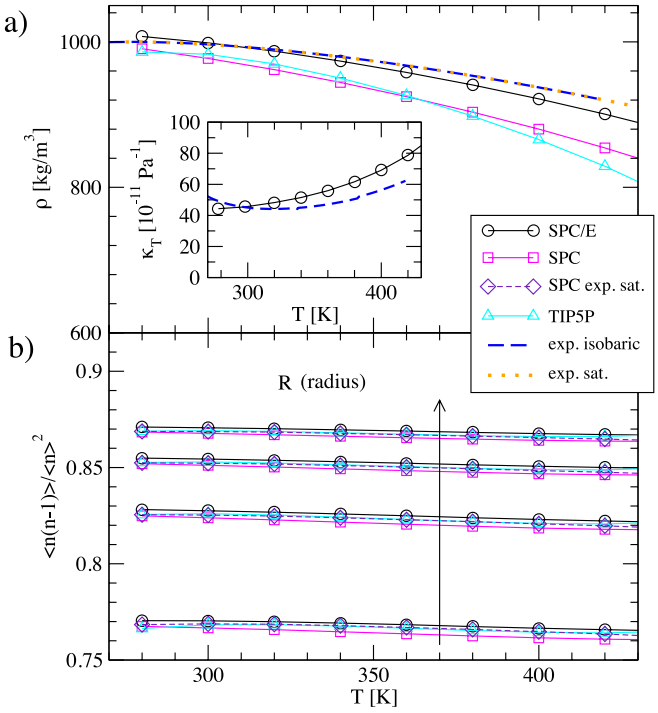

Figure 4.7.: (a) Water density ρ from MD simulations of the SPC/E (circles, black), the SPC (squares, magenta) and the TIP5P (triangles, cyan) water model at a pressure of $p = 1$ bar. Also shown for comparison is the experimental water density for constant pressure $p = 1$ bar (dashed line) [14] and along the saturation curve [215] (dotted line). The inset shows the compressibility of the SPC/E water model (circles) in comparison with the experimental data (dashed line) [14] (b) Normalized solvent particle number fluctuations $\langle n(n-1)\rangle/\langle n\rangle^2$ in a spherical cavity of varying radius $R = 0.28$, 0.31, 0.33 and 0.345 nm for the three considered water models at constant pressure $p = 1$ bar and for SPC water at the experimental saturation density (diamonds, purple). The symbols have the same meaning as in (a). Lines are guides to the eye.

connects particle number fluctuations with the isothermal compressibility κ_T. Neglecting the logarithmic term in Eq. 4.12 and using the compressibility, one obtains the drastically simplified expression

$$\mu_{\mathrm{ex}}^{IT} \approx \frac{\nu}{2\kappa_T}. \tag{4.15}$$

Figure 4.6 c and d show the excess chemical potentials and entropies as obtained from Eq. 4.12 including (circles, full lines) and neglecting (squares, dashed lines) the logarithmic term and also the predictions from Eq. 4.15 (diamonds, dashed-dotted lines) in comparison with the particle insertion results (triangles, dotted lines) for the SPC/E water model. Compressibilities for the SPC/E water model are obtained by a numerical derivative (see Eq. 3.6) and are summarized in Tab. 4.2. While Eq. 4.12 agrees well with the particle insertion results for small solutes and low temperatures, it differs considerably for larger solutes and high temperatures. This indicates a breakdown of the Gaussian approximation so that non-Gaussian contributions to the particle number fluctuations become important [216]. The logarithmic term is not very important for the entropies, as has been noted before [72]. The results from the simplified com-

pressibility expression in Eq. 4.15 are completely off the particle insertion results (see inset of Fig. 4.6), showing that Eq. 4.14 is not valid on the nano scale.

To explain the different results for the different water models and the discrepancy with the data of Ref. 72 we rearrange Eq. 4.12 without the logarithmic term in the following way,

$$\mu_{\mathrm{ex}}^{IT} \approx \frac{k_{\mathrm{B}}T}{2}\left(\frac{\langle n(n-1)\rangle}{\langle n\rangle^2} - 1 + \frac{1}{\nu\rho}\right)^{-1}, \tag{4.16}$$

where we used the relation $\langle n\rangle = \nu\rho$. We show ρ and $\langle n(n-1)\rangle/\langle n\rangle^2$ for the different water models and pressures as obtained from simulations in Fig. 4.7. As noted before [72], $\langle n(n-1)\rangle/\langle n\rangle^2$ shows only a weak dependence on temperature or pressure and does not differ much between the different water models (see Fig. 4.7 b). The density ρ on the other hand shows a pronounced temperature dependence, differs appreciably between the water models and also shows deviations from the experimental data. Comparing with Eq. 4.16 and noting that the neglect of the logarithmic term in Eq. 4.12 is not very serious, as shown in Figure 4.6 c and d, one concludes that it is mostly the variation in ρ that causes the differences in the solvation free energy [72, 206, 208], as seen in Fig. 4.6 a and b. Note that the compressibility κ_T obtained for SPC/E, shown in the inset of Fig. 4.7 a, shows considerable dependence on temperature and agrees overall quite well with experimental data. But, as shown above, its temperature dependence cannot be used as a simple explanation of the entropy convergence phenomena since Eq. 4.14 is too inaccurate to describe solvation of small solutes.

In summary, two different factors contribute to the shift of the entropy convergence temperature between our simulated particle insertion data and the published information theory results: Firstly, the temperature dependence of the experimental coexistence density is quite different from the simulated density at ambient pressure (and as a side remark, this deviation is more pronounced with SPC than with SPC/E), see Fig. 4.7 a, while the experimental densities at ambient and saturation pressures are very close. Secondly, there is a systematic shift of the entropy convergence to higher temperatures for the information theory results as compared to straight particle insertion results, see Figure 4.6 c and d. Finally, we note that the coexistence densities of the SPC water model are significantly lower than the experimental ones [217], simulating the SPC water model at experimental saturation densities therefore leads to unrealistically high pressures, e.g. 880 bar at $T = 500$ K compared to the experimental saturation pressure of 26.4 bar [215]. It is not clear what the significance of such high pressure is, but it might significantly change the water properties and therefore lead to unrealistic results.

4.4.3. Attractive interactions

We next investigate the solvation of non-polar solutes whose interaction with water also has an attractive part, according to Eq. 2.1. For a fixed decay length $1/B =$

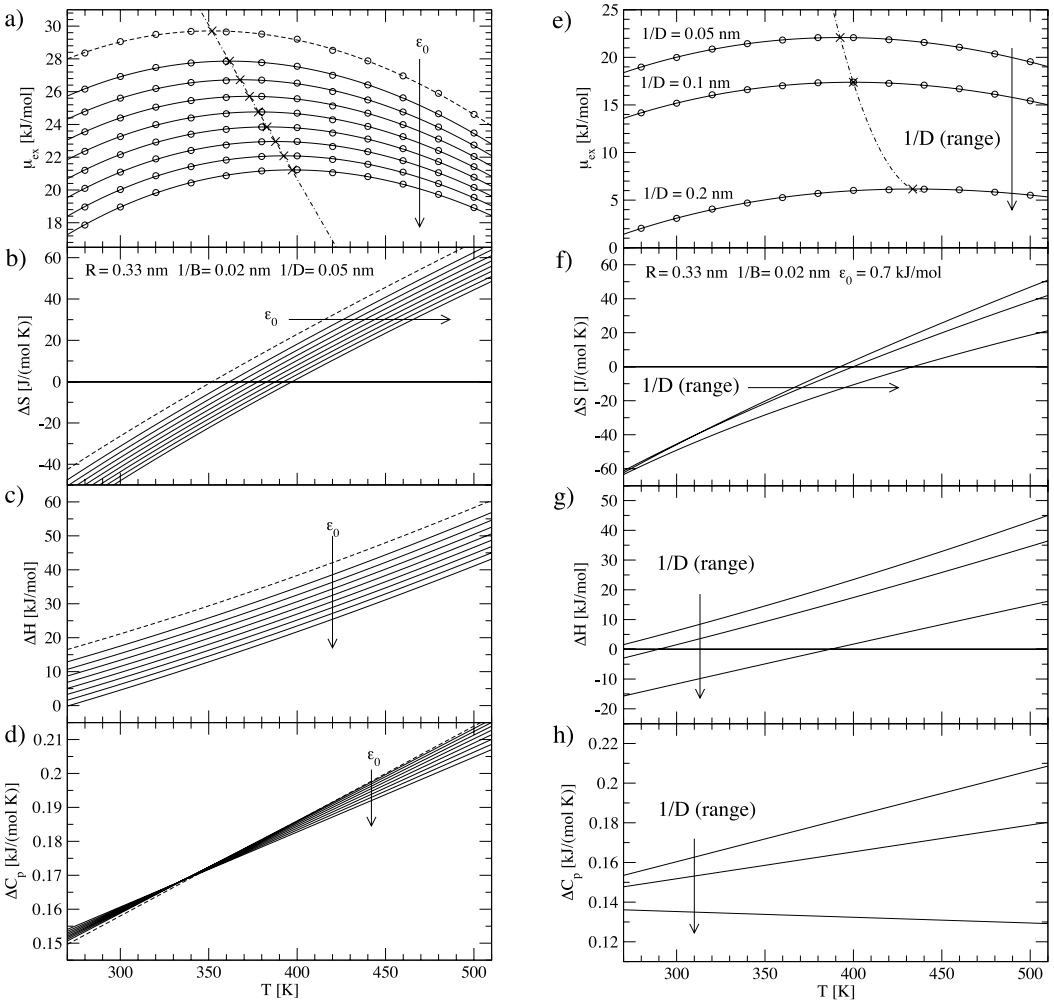

Figure 4.8.: Excess chemical potential for a spherical solute with radius $R = 0.33\,\mathrm{nm}$ (a) for $1/B = 0.02\,\mathrm{nm}$, $1/D = 0.05\,\mathrm{nm}$ and varying potential depth $\epsilon_0 = 0.0$, 0.1, 0.2, 0.3, 0.4, 0.5, 0.6, 0.7 and $0.8\,\mathrm{kJ/mol}$ and (e) for $1/B = 0.02\,\mathrm{nm}$, $\epsilon_0 = 0.7\,\mathrm{kJ/mol}$ and varying range of the attractive part of the potential $1/D = 0.05$, 0.1 and 0.2 nm. Circles show the data obtained by test particle insertion, lines are fits to the particle insertion data. The dashed line marks a purely repulsive solute ($\epsilon_0 = 0$), while the solid lines correspond to the attractive solutes. Crosses indicate the position of the maxima of the free energy curves and the dashed-dotted line is a fit to the maxima. [(b), (f)] Solvation entropies, [(c), (g)] enthalpies and [(d), (h)] heat capacity changes obtained from derivatives of the fits to the free energies shown in (a) and (e). The trajectories for particle insertion are obtained by MD simulation of the SPC/E water model at $p = 1\,\mathrm{bar}$.

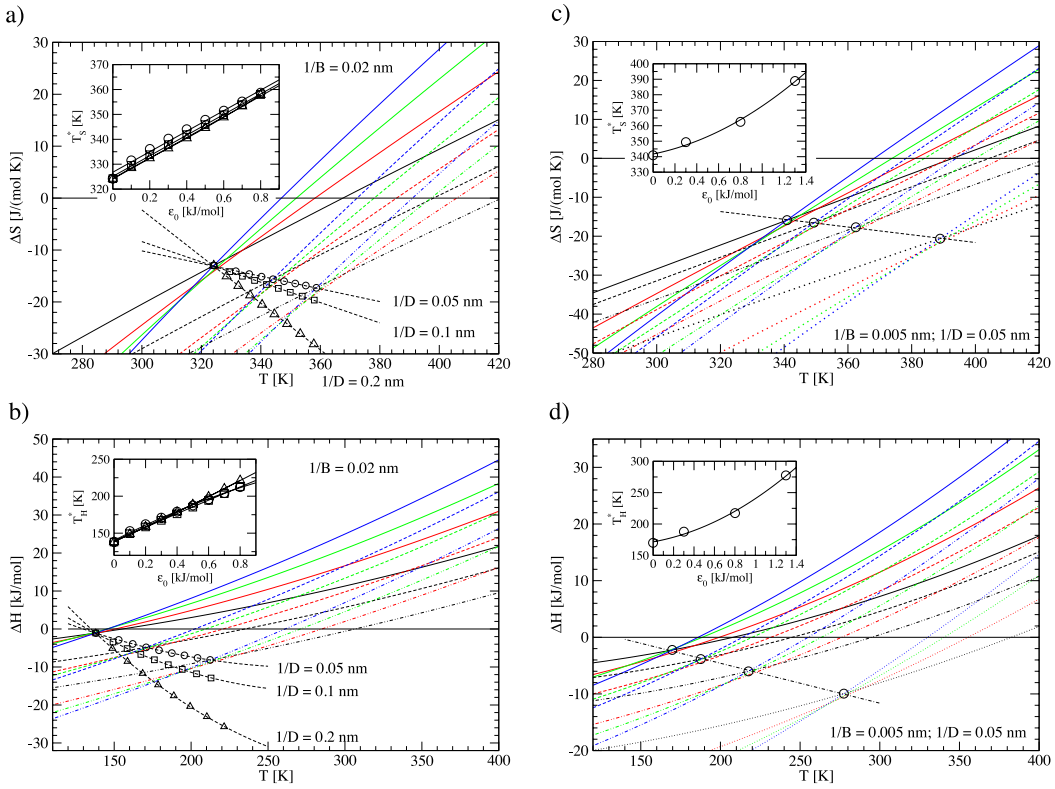

Figure 4.9.: (a) Solvation entropies for solutes with radii $R = 0.28\,\mathrm{nm}$ (black), $0.31\,\mathrm{nm}$ (red), $0.33\,\mathrm{nm}$ (green) and $0.345\,\mathrm{nm}$ (blue) for $1/B = 0.02\,\mathrm{nm}$, $1/D = 0.05\,\mathrm{nm}$ and varying potential depth $\epsilon_0 = 0$ (solid lines), $0.3\,\mathrm{kJ/mol}$ (dashed lines) and $0.8\,\mathrm{kJ/mol}$ (dashed-dotted lines). The symbols show the intersection of the curves for solutes of size $R = 0.28\,\mathrm{nm}$ and $R = 0.345\,\mathrm{nm}$ for an attraction range $1/D = 0.05\,\mathrm{nm}$ (circles), $1/D = 0.1\,\mathrm{nm}$ (squares, entropy curves not shown) and $1/D = 0.2\,\mathrm{nm}$ (triangles, entropy curves not shown) and $1/B = 0.02\,\mathrm{nm}$. The dashed curves are linear fits to the intersection points. The inset shows the convergence temperature defined by Eq. 4.11 for $1/D = 0.05\,\mathrm{nm}$ (circles), $1/D = 0.1\,\mathrm{nm}$ (squares) and $1/D = 0.2\,\mathrm{nm}$ (triangles) and $1/B = 0.02\,\mathrm{nm}$. Solid curves show linear fits to the data. (b) Analogous results for the solvation enthalpy. [(c), (d)] Solvation entropy and enthalpy for the stiffer repulsive potential characterized by $1/B = 0.005\,\mathrm{nm}$ for varying potential depth $\epsilon_0 = 0$ (solid lines), $0.3\,\mathrm{kJ/mol}$ (dashed lines), $0.8\,\mathrm{kJ/mol}$ (dashed-dotted lines) and $1.3\,\mathrm{kJ/mol}$ (dotted lines) and for only one attractive range $1/D = 0.05\,\mathrm{nm}$.

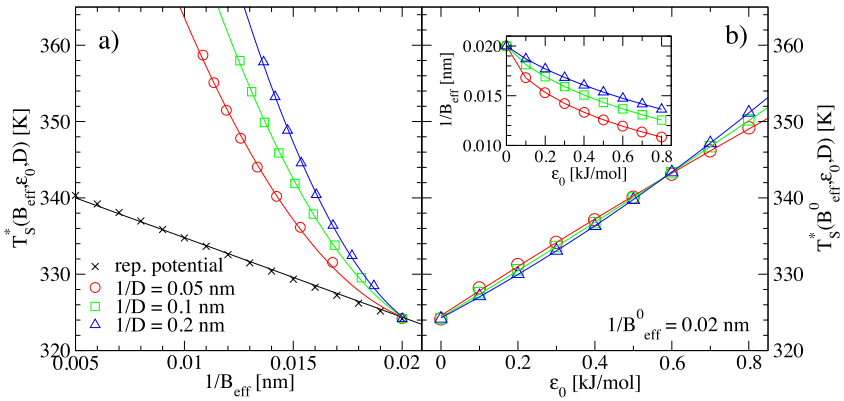

Figure 4.10.: (a) Convergence temperature for spherical solutes with $1/B = 0.02\,\text{nm}$, $1/D = 0.05$ nm (circles), 0.1 nm (squares) and 0.2 nm (triangles) and varying depth ($\epsilon_0 = 0.0$ - 0.8 kJ/mol) as a function of the effective stiffness $(1/B)_{\text{eff}}$, defined in Eq. 4.17. Lines are quadratic fits to the data. Also shown for reference is the convergence temperature for purely repulsive solutes (crosses) including a linear fit to the data. (b) Convergence temperature T_S^*, corrected for the varying effective stiffness as a function of the potential depth ϵ_0. The inset shows the effective stiffness of the attractive potentials as a function of the potential depth. Symbols have the same meaning as in (a). All data is obtained by particle insertion in SPC/E water at $p = 1$ bar.

0.02 nm of the repulsive part of the potential, we vary the range of the attractive interaction ($1/D = 0.05, 0.1$ and $0.2\,\text{nm}$) as well as the potential depth ($\epsilon_0 = 0.0$, 0.1, 0.2, 0.3, 0.4, 0.5, 0.6, 0.7 and $0.8\,\text{kJ/mol}$). In Fig. 4.8 a and b we show the resulting solvation free energies and entropies for a solute of radius $R = 0.33\,\text{nm}$ and for $1/B = 0.02\,\text{nm}$ and $1/D = 0.05\,\text{nm}$ for different values of the potential depth ϵ_0; in Fig. 4.8 e and f we show solvation free energies and entropies for $1/B = 0.02\,\text{nm}$ and $\epsilon_0 = 0.7\,\text{kJ/mol}$ for varying potential range $1/D$. It can be seen from Fig. 4.8 a and e, that for increasing potential depth and range the solvation free energies are shifted downwards, as expected due to the more favorable enthalpic contribution of the attraction (see Fig. 4.8 c and g). For the largest range studied, $1/D = 0.2$ nm, the solvation free energy energy approaches zero, meaning that we are almost describing hydrophilic (yet non-polar) solutes. At the same time the position of the maximum of the free energy curve is shifted towards higher temperatures. Accordingly, also the solvation entropy curves are shifted towards higher temperatures with increasing potential depth and range (see Fig. 4.8 b and f). Interestingly, for increasing attraction, that is as one goes from very hydrophobic solutes to less hydrophobic solutes, the solvation entropies become more negative while the heat capacities in Figs. 4.8 d and h stay roughly the same. This stands in contrast to the common view according to which the solvation of hydrophilic solutes is purely enthalpic and characterized by vanishing heat capacity [63, 68]. We note, that the solvation free energies for a Lennard-Jones parameterization of methane [208] are well within the spread observed in Fig. 4.8

e. For example at $T = 300$ K Ashbaugh et al. [208] find a solvation free energy of 9.3 kJ/mol for OPLS-methane in SPC/E water, while for a methane size solute with $\epsilon_0 = 0.7$ kJ/mol and $1/B = 0.02$ nm we obtain 15.2 kJ/mol for $1/D = 0.1$ nm and 3.2 kJ/mol for $1/D = 0.2$ nm.

The effect of increasing potential depth and range on the convergence temperature is shown in Fig. 4.9, where we plot the solvation entropies and enthalpies for solutes of varying radii and different values of the potential depth ϵ_0 and range $1/D$ as a function of the temperature. For the less stiff repulsive potential characterized by $1/B = 0.02$ nm we show in Figs. 4.9 a and b the intersection points of the entropy and enthalpy curves for solutes with radii $R = 0.28\,\mathrm{nm}$ and $R = 0.345\,\mathrm{nm}$ for attractive potential ranges of $1/D = 0.05\,\mathrm{nm}$ (circles), $1/D = 0.1\,\mathrm{nm}$ (squares) and $1/D = 0.2\,\mathrm{nm}$ (triangles). For the latter two the entropy curves are not shown. In Figs. 4.9 c and d we show data for $1/D = 0.05\,\mathrm{nm}$ and the stiffer repulsive potential $1/B = 0.005$ nm. It can be seen, that the convergence for increasing potential depth is shifted to higher temperatures, while the convergence entropies and enthalpies become more negative. This effect is more pronounced for more long-ranged attraction. In the insets of Fig. 4.9 we plot the convergence temperatures, defined by Eq. 4.11, as a function of the potential depth for varying potential ranges. Surprisingly, the convergence temperatures show very little dependence on the range of the attractive potential. It is apparent from Fig. 2.1 b, that a changing attractive potential depth also modifies the repulsive flank of the potential and thereby increases the apparent stiffness of the potential slightly. To understand the reason for the insensitivity of the entropy convergence temperature on the attractive range, we first have to disentangle the effects due to the repulsive and attractive parts of the potential. As a measure of the actual stiffness of the repulsive flank of the potential we define the effective stiffness $1/B_{\mathrm{eff}}$ of the potential (Eq. 2.1) as

$$\frac{1}{B_{\mathrm{eff}}} = -\frac{k_{\mathrm{B}} T_0}{\partial U_{\mathrm{SPH-OW}}(r)/\partial r|_{r=R}}. \tag{4.17}$$

For a purely repulsive solute (C = 0), this reduces to the usual decay length of the potential, $1/B_{\mathrm{eff}} = 1/B$. The effective stiffness for attractive potentials with varying range $1/D = 0.05$, 0.1 and 0.2 nm is plotted in the inset of Fig. 4.10 b as a function of the potential depth ϵ_0. The increase in the effective stiffness with potential depth is smaller for the longer ranged potentials in accordance with Fig. 2.1. We assume, that the convergence temperature is an analytic function of the effective stiffness B_{eff}, the potential depth ϵ_0 and range D, that is $T_S^* = T_S^*(B_{\mathrm{eff}}, \epsilon_0, D)$. Since with increasing the potential depth ϵ_0 also the effective stiffness B_{eff} increases, it is a priori not clear which of the two causes the change in the convergence temperature. In Fig. 4.10 a, we plot the convergence temperature for the attractive solutes as a function of $1/B_{\mathrm{eff}}$ and compare it to the results for the purely repulsive solutes. It is seen, that the convergence temperature for the attractive solutes rises much faster with increasing effective stiffness than for the purely repulsive solutes, so the change in effective stiffness alone cannot explain the shift in the convergence temperature; it is rather a combined effect

of both factors. In order to disentangle the effects of the attractive interactions and the effective stiffness of the repulsive part of the potential, we expand $T_S^*(B_{\text{eff}}, \epsilon_0, D)$ for fixed D in a Taylor series with respect to ϵ_0 and B_{eff},

$$\begin{aligned} T_S^*(B_{\text{eff}}, \epsilon_0, D) &\approx T_S^*(B_{\text{eff}}^0, \epsilon_0^0, D) \\ &+ \frac{\partial T_S^*(B_{\text{eff}}^0, \epsilon_0^0, D)}{\partial B_{\text{eff}}}(B_{\text{eff}} - B_{\text{eff}}^0) \\ &+ \frac{\partial T_S^*(B_{\text{eff}}^0, \epsilon_0^0, D)}{\partial \epsilon_0}(\epsilon_0 - \epsilon_0^0). \end{aligned} \tag{4.18}$$

Adding and subtracting $T_S^*(B_{\text{eff}}^0, \epsilon_0^0, D)$ one can rearrange Eq. 4.18 to yield

$$\begin{aligned} T_S^*(B_{\text{eff}}, \epsilon_0, D) &\approx T_S^*(B_{\text{eff}}, \epsilon_0^0, D) + T_S^*(B_{\text{eff}}^0, \epsilon_0, D) \\ &- T_S^*(B_{\text{eff}}^0, \epsilon_0^0, D). \end{aligned} \tag{4.19}$$

If we choose $1/B_{\text{eff}}^0 = 0.02$ nm and $\epsilon_0^0 = 0$, then $T_S^*(B_{\text{eff}}, \epsilon_0^0, D)$ and $T_S^*(B_{\text{eff}}^0, \epsilon_0^0, D)$ are given by the results for purely repulsive solutes and we can calculate $T_S^*(B_{\text{eff}}^0, \epsilon_0, D)$ by solving Eq. 4.19. We plot $T_S^*(B_{\text{eff}}^0, \epsilon_0, D)$ for $1/B_{\text{eff}}^0 = 0.02$ nm in Fig. 4.10 b as a function of the potential depth ϵ_0 for the three different ranges studied. Still a strong dependence on ϵ_0 can be observed, while there is almost no change with the range of the attractive part of the potential. We conclude that the entropy convergence temperature shows no dependence on the range of the attractive part of the potential and only depends on the attractive strength and repulsive stiffness. This suggests, that the main contribution to the temperature dependence of the solvation free energy comes from the first solvation shell around the solute and is therefore determined by the short range structure of the hydrogen bonding network.

4.5. Conclusion

We performed an analysis of the solvation properties of small spherical solutes for a broad class of solute-water potentials. In all cases the free energies show a maximum at a temperature that depends quite sensitively on details of the potential, below that temperature the solvation entropy is negative (i.e. the solute orders the water), above that temperature the entropy is positive (i.e. the solute increases the water disorder). The heat capacity is invariably positive. These are the common signatures of hydrophobic solvation of small solutes. No convergence is found for solutes of the same size characterized by different $1/B$ and ϵ_0, but restricted convergence is observed for the same $1/B$ and ϵ_0 and different radii of the solutes. The entropy convergence temperature, at which the solvation entropies of solutes of different radii are the same, depends also on potential details in the following fashion: The less stiff the short-ranged repulsive part of the potential, the lower the convergence temperature, the deeper the attractive part, the higher the convergence temperature. The range of the

attractive part does not influence the convergence properties, which suggests that it is only the first water shell that plays a role for convergence. Nevertheless, these results mean for the case of protein denaturation, where different amino acids plausibly are characterized by different effective water-amino acid potentials, entropy or enthalpy convergence cannot be expected in the general case. This is in agreement with a recent analysis of a large unbiased set of protein data [69]. It has been suggested that the spread in the protein convergence properties in Fig. 4.1 can be related to the size of the proteins [200]. However, when we plot the deviation from a straight-line fit as a function of the number of residues (see Fig. 4.1 b) we seem not to obtain any systematic trend. Likewise, although we show that the extrapolation procedure which is used to obtain thermodynamic data at one temperature, which basically rests on the assumption of a constant heat capacity, is fine for the solvation of non-polar solutes (see our analysis in Figs. 4.2 and 4.3), there could be extrapolation artifacts in the protein denaturation data. However, when we separate data from proteins that denature around 60° C (shown by open circles) from proteins that denature further away from 60° C (filled circles) we do not see a systematic difference in the two data sets, ruling out problems with the extrapolation method as a possible cause of the absence of entropy convergence. Taken together all evidence, entropy convergence of protein denaturation does not seem to be evidenced by the experimental data.

Although strictly speaking we cannot conclude that the breakdown of convergence in protein denaturation data is caused by the variations of the interactions of individual amino acids with water as we have studied in this work, we note that these variations are sufficient to give rise to a breakdown of convergence. Other factors that would work in the same direction are specificities in the folded state, which we did not address.

Most directly our results are applicable to the solvation of gaseous particles in water, since here specifics of the reference state (which is the liquid state for liquid hydrocarbons or the protein core for folded proteins) are absent. We stress again a subtle point mentioned already in the previous sections: For liquid hydrocarbons which form a homologous series, entropy convergence is foremost a consequence of the additivity of solvation properties of individual methyl and methylene groups and yields a vanishing entropy at the convergence temperature. In contrast, convergence for different noble gases is not connected to the additivity hypothesis but rather to an insensitivity of solvation thermodynamics to variations in the solute-water interaction and leads in general to a non-vanishing entropy at convergence.

We see that the entropy convergence of noble gases, which experimentally occurs around 380 K, is quite well reproduced for sensible values of the attractive strength and range around $1/B = 0.005$ nm and $\epsilon_0 = 1.3$ kJ/mol. Experimentally, the convergence is far from perfect, since e. g. the entropies of Ne, Ar and Xe do not cross at one temperature. The actual value of the entropy at convergence comes also out quite well from our simulation results. As seen in Fig. 2 of Ref. 43, Ar and Xe cross at an entropy of $\Delta S \approx -4$ cal/mol K ≈ -17 J/mol K, which is in line with typical convergence en-

tropies we obtain for a wide range of values of the attractive depth between $\epsilon_0 = 0.3$ and 1.3 kJ/mol, see Fig. 4.9 c.

Note that the model potential considered by us should be viewed as realistic for the solvation of hydrophobic particles which cannot form hydrogen bonds with the water. In the future, it will be interesting to study polar solutes as well and to check whether robust and significant differences to the solvation of unpolar solutes are obtained.

As a word of caution, we note that convergence properties depend sensitively on the water parameters used, which simply reflects the fact that one is dealing with higher-order derivatives of the free energy. Thus, they are very sensitive to small force-field variations and imperfections. The actual numbers quoted by us should thus be considered with care. Likewise, we only study small radii, for which more complicated effects associated with the crossover to the solvation of planar interfaces is not yet reached [42].

CHAPTER 5

SURFACE FUNCTIONAL DESCRIPTION OF HYDROPHOBIC HYDRATION

5.1. Introduction

5.1.1. Motivation

As noted above, the hydrophobic effect is the dominant driving force for self-assembly in the aqueous environment and spans many length scales, ranging from protein folding over macromolecular aggregation and membrane formation to macroscopic phase separation [52]. The solvation of hydrophobic objects displays a characteristic crossover at a length scale of $R^* \approx 0.5$ nm [40, 41, 43] which can be associated with the discreteness of water: While small hydrophobic solutes can be readily accommodated within the water hydrogen bonding network, mostly reducing the water configurational freedom, large solutes lead to a reduction of hydrogen bonds and the formation of a liquid-vapour like interface. It has been a long standing question how hydrophobic solvation on the nanoscale can be described by an interface model in terms of suitably defined geometrical measures.

In 1949, Tolman [79] proposed an asymptotic curvature correction for the surface tension of a spherical cavity, obtained from purely thermodynamic considerations,

$$\gamma_{\mathrm{SPH}} = \gamma_0 \left(1 - \frac{2\delta}{R}\right), \tag{5.1}$$

where γ_0 is the surface tension of a planar interface, R is the cavity radius and δ is the Tolman length, which corresponds to the shift between the Gibbs dividing surface (GDS) R_{GDS} and the surface of tension R_{S} in the planar limit [218],

$$\delta = \lim_{R\to\infty} R_{\mathrm{GDS}} - R_{\mathrm{S}}. \tag{5.2}$$

With the convention that the radius of a cavity (or bubble) is taken as positive (note that all cited results are adapted to this sign convention), a negative Tolman length

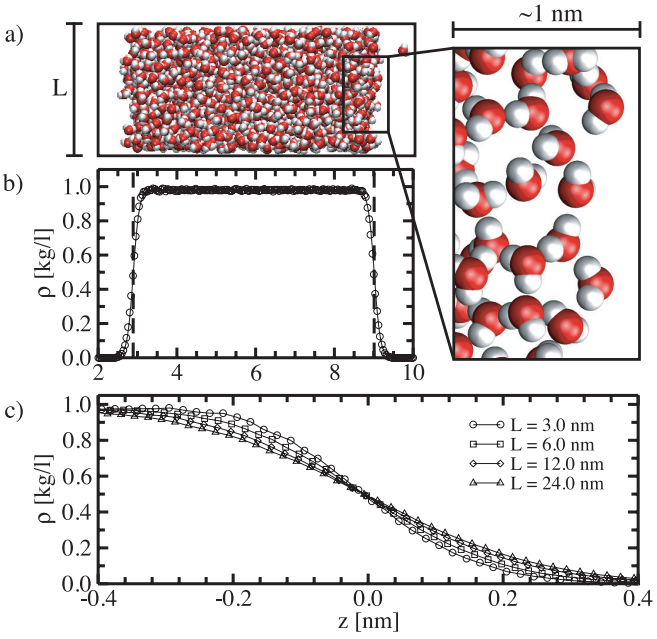

Figure 5.1.: a) Simulation snapshot of a simulation system containing two air/water interfaces for a lateral box size of $L = 3.0\,\mathrm{nm}$, containing 1807 water molecules. The enlarged slice to the right exhibits pronounced surface roughness. b) Average density profile (circles, $L = 3.0\,\mathrm{nm}$) compared with a hyperbolic tangent fit (solid line). Vertical dashed lines show the positions of the global GDS. c) Density profiles centered around the GDS for varying L; lines are guides to the eye.

means that a droplet is preferred over a cavity, i.e. the surface of tension is shifted towards the liquid water side of the GDS.

A more general description of the free energy of an interface is given by Helfrich's phenomenological curvature expansion [89],

$$\Delta F = \int dA \left[\tilde{\gamma} + 2\kappa (J - c_0)^2 + \bar{\kappa} K \right], \tag{5.3}$$

where $J = (1/R_1 + 1/R_2)/2$, $K = 1/(R_1 R_2)$ and c_0 are the mean, Gaussian and spontaneous curvatures, $R_{1,2}$ are the local principal radii of curvature and κ and $\bar{\kappa}$ are the normal and Gaussian bending rigidities. The planar surface tension is given by the constant term in Eq. 5.3, $\gamma_0 \equiv \tilde{\gamma} + 2\kappa c_0^2$. Expressions like Eqs. 5.1 and 5.3 give a simple description of hydrophobic solvation and are at the core of advanced implicit solvation models [219].

However, the determination of the coefficients is for several reasons not straightforward: i) While the magnitude of δ is generally agreed to be on the order of the molecular size, not even for simple Lennard-Jones (LJ) liquids a consensus is reached about its sign, see [80, 81] and references therein. ii) The aforementioned crossover between small-scale and large-scale solvation, caused by the water discreteness, occurs at roughly the same scale as the Tolman length, i.e. $R^* \sim \delta$, and it is not straightforward to disentangle these two lengths. iii) Furthermore, it is not clear how the Tolman length for water in contact with a hard solute compares with that of a liquid droplet or a bubble, where one has a liquid-vapor interface [220–224]. Using a combination of simulations and scaled particle theory, a Tolman length of the order of 1 Å was predicted for water at ambient temperature [83, 85]. Ashbaugh and Pratt [43] find

$\delta \approx 0.6$ Å at $T = 300$ K which decreases with increasing temperature and changes sign at $T \approx 350$ K. Huang et al. [42] deduce $\delta = 0.9$ Å at $T = 298$ K for SPC/E water from simulated solvation free energies of hydrophobic spheres. Yamamoto and Ohnishi [225] on the other hand find a maximum in the surface tension of helium bubbles in water as a function of bubble radius, corresponding to a negative Tolman length.

Not surprisingly, the sign and magnitude of the second order curvature correction is much debated as well. Square-gradient theory yields a negative bending rigidity for the "equilibrium route" [90], that is by considering an interface that is curved due to an external potential, while van Giessen and Blokhuis [226] obtained a positive κ and negative $\bar{\kappa}$ by applying a virial expression to computer simulations of a Lennard-Jones liquid forming spherical and cylindrical droplets.

Instead of bending the water surface by external forces, represented by a solute, one can also obtain information on the interfacial elastic properties by studying the equilibrium fluctuations of a free liquid/vapour interface, i. e. thermally induced capillary waves, which has been termed "fluctuation route" [90]. Standard capillary wave (CW) theory can be extended to incorporate the effects of higher order curvature corrections as described by Eq. 5.3, which results in a wave vector dependent effective surface tension $\gamma_{\text{eff}}(q) = \gamma_0 + \kappa q^2$ [93]. Note, that odd curvature terms vanish due to symmetry reasons.

Since a few years grazing-incidence X-ray scattering from liquid surfaces yields information on lateral density correlations in the interfacial region. The obtained scattering signal combines effects due to bulk-like density fluctuations close to the interface, dominant at large wavevectors [97], and effects due to shape fluctuations of the interface, dominant at small wavevectors [95, 96]. Disentangling these two contributions in the experimentally accessible intermediate range of wavevectors and extracting the capillary wave spectrum of the liquid-vapor surface is by no means straightforward [91, 98–100]. Experimental scattering spectra span the wave vector range of $q^{-1} \simeq 0.1 - 10\,\text{nm}$, posing a dilemma: for q values small enough that CW theory is valid, the deviations from the trivial limit $\gamma_{\text{eff}}(q) = \gamma$ are small and accuracy becomes the limiting factor.

In theoretical work, the extended capillary wave theory has been applied to the liquid vapor interface in a Lennard-Jones fluid by Stecki [93, 94], who found evidence for a negative bending rigidity. Chacón and Tarazona [92] on the other hand found a positive bending rigidity, using a different definition of the surface, where a minimum area surface is pinned to a set of pivot atoms. To complicate matters, it has been suggested by Blokhuis et al. [90], that the bending rigidities obtained by this "fluctuation route" might differ from those obtained by the "equilibrium route". Furthermore it has been argued, that for interaction potentials decaying $\propto r^{-6}$ a curvature expansion of the surface tension fails beyond the linear term [91, 227, 228], a problem which can be circumvented if the retardation to a r^{-7} dependence is taken into account.

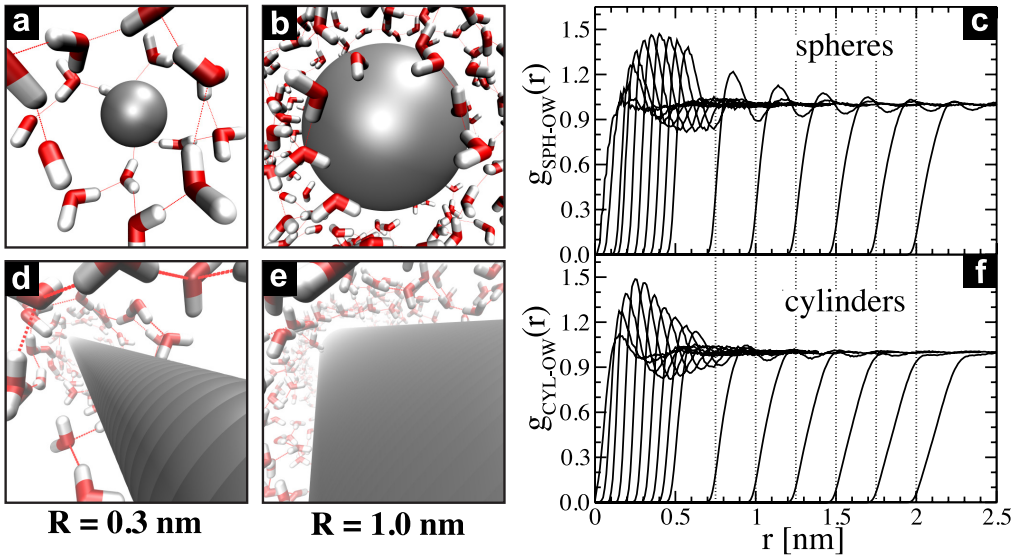

Figure 5.2.: Simulation snapshots of [(a),(b)] spherical and [(d),(e)] cylindrical hydrophobic solutes in water with different radii. Dashed lines indicate water hydrogen bonds. [(c),(f)] Radial distribution functions $g_{\mathrm{SPH-OW}}(r)$ and $g_{\mathrm{CYL-OW}}(r)$ between solutes and water oxygen atoms for solute radii in the range $R = 0.05 - 2.0\,\mathrm{nm}$. Vertical dotted lines indicate the solute radii for $R \geq 0.75$ nm. All simulation data for SPC/E water at $T = 300\,\mathrm{K}$ and $p = 1$ bar.

Capillary waves also have a broadening effect on liquid surfaces, adding to the intrinsic width of the interface with important consequences for scattering experiments probing the structure normal to the interface. Recent scattering experiments [229] suggest that the contribution of the intrinsic roughness is greater and consequently the length scale at which capillary wave theory breaks down is larger than it was previously assumed [230–233].

5.1.2. Outline

In this work we use large scale MD simulations to gain a thorough understanding of the curvature dependence of the interfacial free energy of water.

In Sec. 5.2 we follow the "fluctuation route", that is we investigate interfacial shape fluctuations present in large-scale atomistic simulations of the water-vapor interface (see Fig. 5.1). Simulating up to $N = 115000$ molecules in a rectangular box such that a water slab with two planar interfaces spontaneously forms, we can probe lateral length scales up to 24 nm and thus are in a similar wave vector range as scattering experiments; however, complete configurational knowledge allows us to gain structural insight beyond the pair correlation level. We introduce a method to separate bulk-like and interfacial shape fluctuations without any fitting parameters, which allows us to extract an estimate for the bending rigidity κ by comparison with capillary wave the-

ory. We further reconstruct the intrinsic density profile at the air/water interface by deconvolution and discuss the contribution of capillary waves to the total interfacial width.

In Sec. 5.3 we use a complementary approach. We determine solvation free energies of hydrophobic spherical and cylindrical solutes of radii up to $R = 2$ nm in water (see Fig. 5.2). By considering the full radius range from zero to $R = 2$ nm, we cover the crossover between the regimes where the solvation free energy scales as the cavity volume (for $R < R^*$) and where it scales as the surface area (for $R > R^*$). Simultaneously considering spherical and cylindrical geometries allows us to reliably extract the Tolman length, which is shown to be negative, and to obtain estimates for the other elastic constants of the Helfrich formula (Eq. 5.3). By comparing the solvation free energies of spheres and cylinders, we also estimate the free energy for aggregation of spheres into cylindrical objects.

5.2. Capillary waves at the air/water interface

5.2.1. Capillary wave theory

We have come a long way since the pioneering work of van der Waals (VDW) [218], who described the density profile across the interface on the mean field level (neglecting fluctuations of the interface shape) in the form

$$\rho(z) = \frac{\rho_\mathrm{l} + \rho_\mathrm{v}}{2} + \frac{\Delta\rho}{2} \tanh(\frac{2z}{w}), \tag{5.4}$$

where $\rho_{\mathrm{l,v}}$ are the bulk liquid and vapour densities, $\Delta\rho = \rho_\mathrm{l} - \rho_\mathrm{v}$ and w is a measure of the interfacial width. On the other hand, in capillary wave theory [234], the density profile is assumed to be kink-like while the interface position $h(\vec{r}_{||})$ is a smooth function of the lateral coordinate $\vec{r}_{||} = (x, y)$. For Gaussian fluctuations, the CW spectrum is

$$< |h(q)|^2 >= \frac{k_\mathrm{B} T L^2}{q^2 \gamma_\mathrm{eff}(q)}, \tag{5.5}$$

where L is the lateral system size,

$$h(\vec{q}) = \int h(\vec{r}_{||}) e^{i\vec{q}\cdot\vec{r}_{||}} d^2 r_{||} \tag{5.6}$$

is the Fourier transform of $h(\vec{r}_{||})$, and $\gamma_\mathrm{eff}(q)$ is the wave vector dependent effective surface tension. In the original CW theory [234] $\gamma_\mathrm{eff}(q) = \gamma_0$ where γ_0 is the macroscopic surface tension of the planar interface. Including the coupling between the intrinsic density profile and interface shape fluctuations [90, 235], additional terms in the CW spectrum appear and in a low-momentum expansion one finds $\gamma_\mathrm{eff}(q) = \gamma_0 + \kappa q^2$ in accordance with Helfrich's formula (Eq. 5.3).

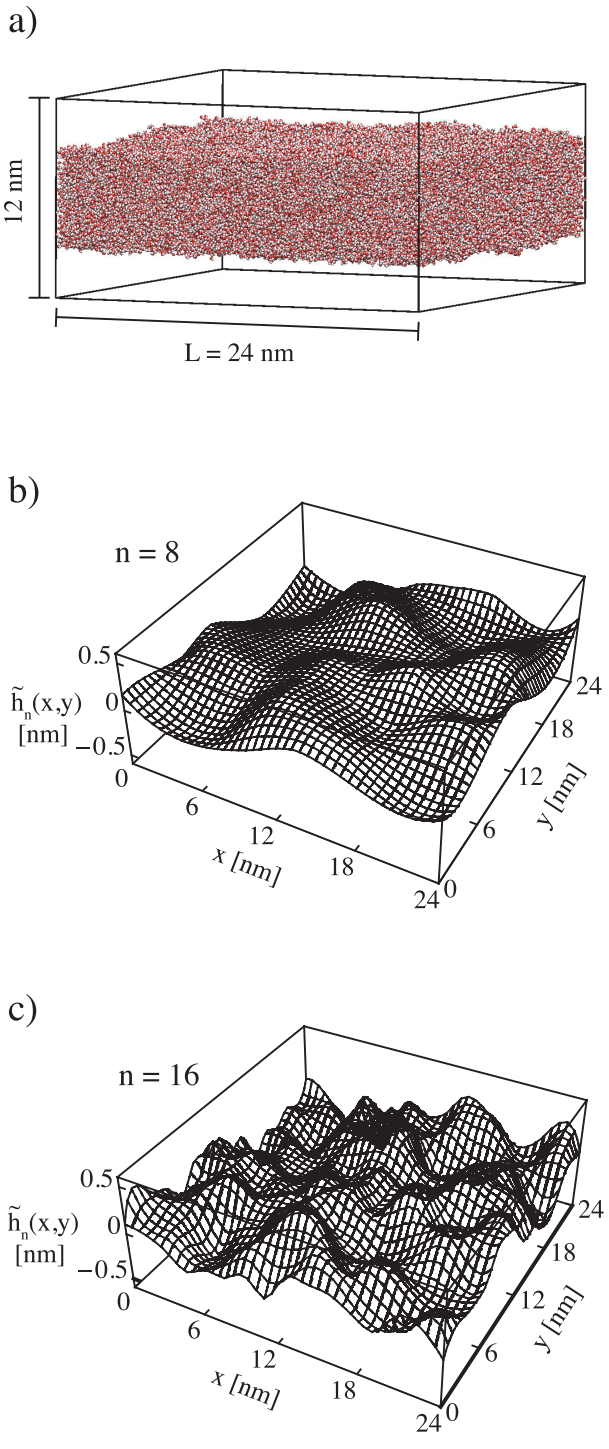

Figure 5.3.: a) Perspective view of the simulation system for the investigation of the air/water interface. The periodic box, indicated by the black frame, has a size of $24 \times 24 \times 12$ nm^3 and contains $\approx 115\,000$ water molecules. The simulation is done at $T = 300$ K. b),c) Illustration of the interfacial profile $\tilde{h}_n(x, y)$ obtained by the block averaging procedure from the simulation system shown in panel a for $\alpha = 3$ and block factors of b) n=8 and c) n=16.

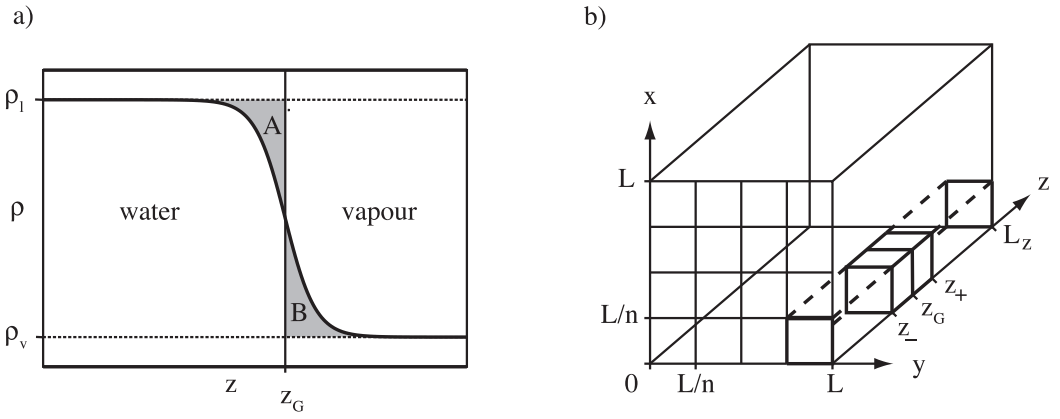

Figure 5.4.: a) Schematic illustration of the definition of the Gibbs-dividing-surface. The position z_G is defined in such a way, that the shaded regions A and B have equal area. b) Illustration of the prisms used in the local GDS method to extract the interface profile.

5.2.2. Interface extraction

Figure 5.3 a shows a perspective view of the simulation system. From the atomic coordinates, the interface profile is determined by the local Gibbs-dividing-surface (GDS) method [236] (see Fig. 5.4). The GDS is a measure for the interface position defined as the boundary z_G, for which the surface excess of the water vanishes,

$$\int_{-\infty}^{z_G} \left[\rho(z) - \rho_l\right] dz + \int_{z_G}^{\infty} \left[\rho(z) - \rho_v\right] dz = 0. \tag{5.7}$$

Here, $\rho_{l,v}$ are the bulk liquid and vapour densities. In Fig. 5.4 a this is schematically shown. Equation 5.7 enforces that the two shaded regions denoted by A and B have equal area.

To determine the interface profile the simulation box is divided into $n \times n$ prisms with quadratic base area of edge length $\Delta L = L/n$, as shown in Fig. 5.4 b. The interface height $\tilde{h}_n(\vec{r}_{||})$ at the lateral coordinates $\vec{r}_{||}$ is then defined as the position of the local GDS within the prism centered around $\vec{r}_{||}$, that is by Eq. 5.7 with z_G replaced by $\tilde{h}_n(\vec{r}_{||})$ and $\rho(z)$ replaced by the density profile $\rho_{r_{||}}(z)$ within the corresponding prism. Thus, $\tilde{h}_n(\vec{r}_{||})$ is defined only on the grid formed by the prisms footprints. To separate the two interfaces present in the simulation box and to control the influence of the bulk fluctuations the prisms are further restricted to an interval $[z_-, z_+]$ in z direction, where $z_\pm = z_G \pm \alpha w$, z_G is the global GDS, w is the interfacial width and α is an adjustable parameter. With these substitutions Eq. 5.7 reads

$$\int_{z_-}^{\tilde{h}_n(\vec{r}_{||})} \left[\rho_{r_{||}}(z) - \rho_l\right] dz + \int_{\tilde{h}_n(\vec{r}_{||})}^{z_+} \left[\rho_{r_{||}}(z) - \rho_v\right] dz = 0. \tag{5.8}$$

Multiplying both sides with $(\Delta L)^2$ and rearranging Eq. 5.8 we find

$$\tilde{h}_n(\vec{r}_{||}) = \frac{M_{r_{||}}}{(\Delta L)^2 \Delta\rho} - \frac{\rho_l z_- + \rho_v z_+}{\Delta\rho}, \tag{5.9}$$

where $\Delta\rho = \rho_l - \rho_v$ and $M_{r_{||}} = (\Delta L)^2 \int_{z_-}^{z_+} \rho_{r_{||}}(z) dz$ is the number of molecules in the prism centered around $\vec{r}_{||}$. The advantage of this method is, that it does not involve fitting of the density profile in a single prism and is therefore still applicable for large n, where the average number of molecules in a prism is very small. The height profile obtained by this method is denoted by $\tilde{h}_n(\vec{r}_{||})$, in contrast to the height function $h(\vec{r}_{||})$ that appears in capillary wave theory, since it depends on the block factor n, which specifies the lateral resolution $\Delta L = L/n$, α, the prism height, and also contains contributions from bulk-like density fluctuations. Figure 5.3 b and c show the height profile obtained from the same configuration for different values of the block factor n.

The coarse-grained profile $\tilde{h}_n(\vec{r}_{||})$ is related to the infinite-resolution limit $\tilde{h}(\vec{r}_{||}) \equiv \lim_{n\to\infty} \tilde{h}_n(\vec{r}_{||})$ by the convolution

$$\tilde{h}_n(\vec{r}_{||}) = \int d^2 r'_{||} g_n(\vec{r}_{||} - \vec{r}'_{||}) \tilde{h}(\vec{r}'_{||}), \tag{5.10}$$

with the coarse-graining function $g_n(\vec{r}_{||}) = 1/(\Delta L)^2$ for $-\Delta L/2 < x, y < \Delta L/2$ and $g_n(\vec{r}_{||}) = 0$ otherwise. The connection with the height function $h(\vec{r}_{||})$ that appears in the CW theory in Eq. (5.5) will be discussed below.

5.2.3. Interfacial broadening

The total width of the interfacial density profile is due to the width of the intrinsic density profile, which is the density profile in absence of capillary waves, and the broadening due to fluctuations of the surface shape. Having determined the profile of the surface shape, the intrinsic density profile can be reconstructed by shifting the molecular positions by the position of the local GDS,

$$\rho_{\mathrm{int},n}(z) = \langle \sum_{i=1}^{N} \delta(z - z_i + \tilde{h}_n(\vec{r}_{||,i})) \rangle / L^2, \tag{5.11}$$

where $\vec{r}_{||,i}$ and z_i are the coordinates of the water molecules. In Fig. 5.5 we show $\rho_{\mathrm{int},n}(z)$ for $n = 1$ and $n = 30$. The inset shows that for a given α a value of the lateral resolution $\Delta L = L/n$ exists for which the width w of $\rho_{\mathrm{int},n}(z)$ is minimal. For $\alpha = 3$ we find a minimal w for $\Delta L^* = L/30 = 0.8\,\mathrm{nm}$, which agrees with the roughness length scale found by visual inspection of the snapshots (see Fig. 5.1). It also coincides more or less with the cross-over radius R^* in the solvation of hydrophobic spheres [41] (as discussed below), supporting the view that this is the length scale of the intrinsic roughness due to the restructuring of the H-bonding network in water. For smaller n capillary waves broaden the interface, for larger n nano-scale roughness increases the

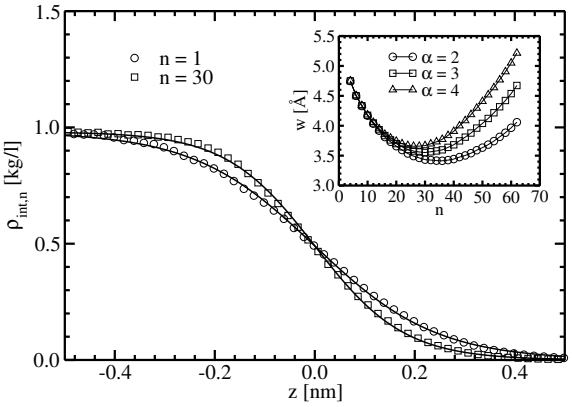

Figure 5.5.: Intrinsic density profiles $\rho_{\mathrm{int},n}(z)$ for $\alpha = 3$ and block factor $n = 30$ (circles) and $n = 1$ (squares, corresponding to the global laterally averaged density profile) with fits $\rho_{\mathrm{int},n}(z) = (\rho_\mathrm{l} + \rho_\mathrm{v})/2 + (\Delta\rho/2)\tanh(2z/w)$ (solid lines). The inset shows the width w as a function of n for $\alpha = 2, 3, 4$. Here $L = 24$ nm.

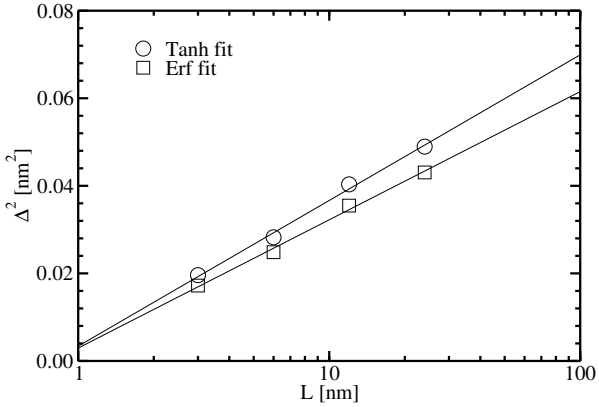

Figure 5.6.: Squared total interfacial width Δ^2 as a function of the lateral system size L obtained either from a hyperbolic tangent (circles) or an error function (squares) fit to the averaged density profile across the air/water interface. The lines are linear fits to the data. Note the logarithmic scale of the abscissa.

width of the intrinsic density profile. The slight α dependence of the minimum is due to bulk-like density fluctuations as discussed below.

Similarly, for increasing system size L, the density profiles in Fig. 5.1 c exhibit increasing widths due to the increasing effects of capillary waves. In the convolution approximation [237] the interfacial width is given by

$$\Delta^2 = \Delta_0^2 + \frac{k_B T}{2\pi\gamma_0} \ln\left(\frac{L}{b}\right), \tag{5.12}$$

where Δ_0 is the intrinsic width and the second term describes the contribution of capillary waves. It depends logarithmically on the lateral system size L and the length scale b associated with the short-wavelength cut-off of the capillary wave modes. We extract the total width from the simulation trajectory by fitting the averaged density profile normal to the interface either with the mean field hyperbolic tangent (see Eq. 5.4) or an error function,

$$\rho(z) = \frac{\rho_l + \rho_v}{2} + \frac{\Delta\rho}{2} \mathrm{erf}\left(\frac{\sqrt{\pi} z}{w}\right). \tag{5.13}$$

The squared width Δ^2, which is defined as the variance of the derivative $\rho'(z)$, is then given by $\Delta^2 = (\pi w)^2/48$ for the hyperbolic tangent and by $\Delta^2 = w^2/(2\pi)$ for the error function [237]. In Fig. 5.6 we plot the squared total width Δ^2 as a function of the lateral system size L for both the hyperbolic tangent and the error function fit. It is seen that the total width indeed scales with the logarithm of the lateral system size, as predicted by capillary wave theory. From the slope of a linear fit to the data, we calculate the planar surface tension γ_0 yielding $\gamma_0 = 45.6$ mN/m for the hyperbolic tangent fit and $\gamma_0 = 51.3$ mN/m for the error function fit. The result from the error function fit agrees very well with the surface tension obtained independently from the anisotropy of the pressure tensor ($\gamma_{lv,0} = 52.9$ mN/m) in agreement with the findings of Ismail et al. [237]. Note, that the simulations in this section are done with a slightly smaller Lennard-Jones cutoff $r_c = 0.8$ nm, leading to a slightly smaller surface tension in comparison with the results presented in Sec. 5.3.

The intrinsic width Δ_0 can be inferred from the width of the intrinsic density profile (see Fig. 5.5). Since the intrinsic width depends on the block factor n but only slightly on the parameter α with which the height profile is determined, we take the minimal width for $\alpha = 3$ as an estimate of the intrinsic width, yielding $\Delta_0 = 1.6$ Å. Using Eq. 5.12 we can obtain the short-wavelength cut-off b from the fit to the simulation data. We find $b = 4.8$ nm for the hyperbolic tangent fit and $b = 6.1$ nm for the error function fit, in agreement with recent X-ray reflectivity experiments [229]. These findings support the view that capillary wave theory breaks down at length scales larger than the molecular size of the liquid, in considerable contrast to the assumption in previous works [231].

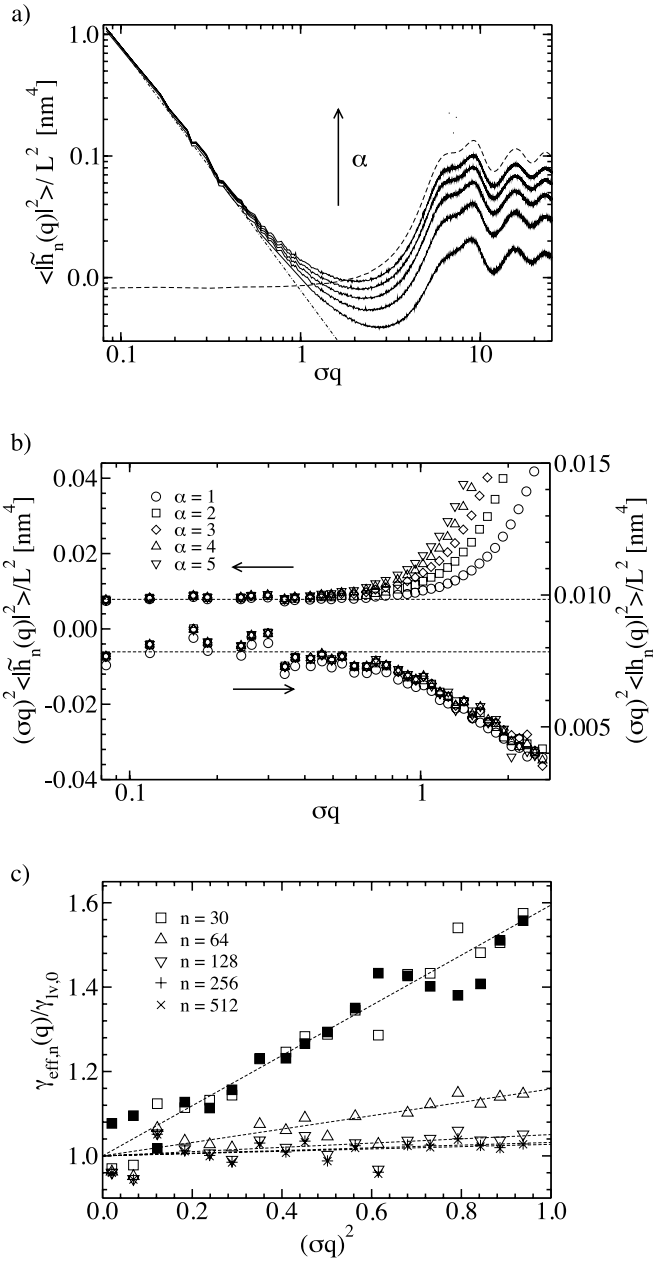

Figure 5.7.: a) Capillary wave spectra $\langle|\tilde{h}_n(q)|^2\rangle$ for $n = 1024$ and α ranging from 1 to 5 (from bottom to top, full lines). For comparison $S^b_{||}(\vec{q})$, the lateral bulk structure factor for a slab thickness $5w$, scaled by an arbitrary factor, (dashed line) and the CWT result with $\gamma_0 = \gamma_{\mathrm{lv},0}$ (dash-dotted line) are included. b) Bare capillary wave spectra $(\sigma q)^2\langle|\tilde{h}_n(q)|^2\rangle$ (upper data set, left scale) and $(\sigma q)^2\langle|h_n(q)|^2\rangle$ according to Eq. 5.20 (lower data set, right scale) for $n = 64$ and varying α. The dashed straight lines show the surface tension contribution determined independently. c) Rescaled effective surface tension $\gamma_{\mathrm{eff},n}/\gamma_{\mathrm{lv},0}$ for $\alpha = 3$ and varying n. Full squares for $n = 30$ correspond to a LJ cutoff $r_c = 1.6\,\mathrm{nm}$, all other data are for $r_c = 0.8\,\mathrm{nm}$. Dashed lines are fits of the form $\gamma_{\mathrm{eff},n}/\gamma_{\mathrm{lv},0} = 1 + \kappa_n/\gamma_{\mathrm{lv},0}q^2$. In all plots $L = 24\,\mathrm{nm}$ and q is rescaled by the water LJ diameter $\sigma = 3.166$ Å.

5.2.4. Lateral correlations

The lateral structure factor is defined as

$$S_{||}(q) = \int \frac{d^3r d^3r'}{N_{||}} f(z) f(z') e^{i\vec{q}\cdot(\vec{r}_{||}-\vec{r}'_{||})} \langle \hat{\rho}(\vec{r})\hat{\rho}(\vec{r}')\rangle^{c}, \tag{5.14}$$

with the microscopic density $\hat{\rho}(\vec{r}) = \sum_{i=1}^{N} \delta(\vec{r} - \vec{r}_i)$, the weight function $f(z)$ and the normalization factor

$$N_{||} = \int d^3r f^2(z) \langle \hat{\rho}(\vec{r})\rangle. \tag{5.15}$$

$S_{||}(\vec{q})$ is obtained from grazing angle X-ray diffraction below the critical angle for total reflection, in which case the weight function is $f(z) = \exp(-|z|/(2l))$ and l is the penetration depth, which depends on the wave vector transfer normal to the surface q_z. We write the microscopic density as

$$\hat{\rho}(\vec{r}) = \rho_l \theta(h(\vec{r}_{||}) - z) + \rho_v \theta(z - h(\vec{r}_{||})) + \delta\hat{\rho}(\vec{r}), \tag{5.16}$$

where $\delta\hat{\rho}$ accounts for all density fluctuations not captured by the sharp-kink approximation and $\theta(z) = 1$ for $z > 0$ and zero otherwise. Equation (5.14) leads to

$$S_{||}(q) \equiv (\Delta\rho)^2 \langle |h(q)|^2\rangle / N_{||} + \Delta S_{||}(q), \tag{5.17}$$

where the contribution due to density fluctuations is

$$\Delta S_{||}(q) = \int d^3r d^3r' f(z) f(z') e^{i\vec{q}\cdot(\vec{r}_{||}-\vec{r}'_{||})} \langle \delta\hat{\rho}(\vec{r})\delta\hat{\rho}(\vec{r}')\rangle. \tag{5.18}$$

In the limit $n \to \infty$, the relation

$$\lim_{n\to\infty} \langle |\tilde{h}_n(q)|^2\rangle \equiv \langle |\tilde{h}(q)|^2\rangle = N_{||} S_{||}(q)/(\Delta\rho)^2 \tag{5.19}$$

between the power spectrum of the local GDS and the lateral structure factor with a rectangular weight function $f(z) = \theta(z_+ - z)\theta(z - z_-)$ holds, where $N_{||} = \rho_l \alpha w L^2$, which is formally proven in App. A. Figure 5.7 a shows $\langle |\tilde{h}_n(q)|^2\rangle$ obtained by Fourier-transforming simulation data for $\tilde{h}_n(\vec{r}_{||})$ for different values of α and $n = 1024$. Comparison with the bulk structure factor for a slab (broken line) shows that bulk-like density fluctuations dominate at high wave vectors and are proportional to α. To extract the bare height spectrum $\langle |h(q)|^2\rangle$ one has to subtract $\Delta S_{||}$, ideally in an experimentally reproducible fashion. A meaningful subtraction is possible by using the structure factor $S_{||}^{b}(q)$ calculated analogously to Eq. (5.14) in a slab located in the bulk of the liquid. Note that $S_{||}^{b}(q)$ can be calculated for an arbitrary weight function $f(z)$ from the experimentally accessible 3D bulk structure factor, as shown in App. A. In our simulations we calculate $S_{||}^{b}(q)$ with the same block factor n for an interval of size αw centered

around the middle of a water slab. We furthermore use $S_{||}(q) = (\Delta\rho)^2\langle|\tilde{h}_n(q)|^2\rangle/N_{||}$ even for finite n and make the association $\Delta S_{||}(q) = S^b_{||}(q)$. These simplifications can be viewed as a definition of the interface profile $h(\vec{r}_{||})$. Using Eq. (5.17) we thus obtain

$$\langle|h_n(q)|^2\rangle = \langle|\tilde{h}_n(q)|^2)\rangle - N_{||}S^b_{||}(q)/(\Delta\rho)^2. \tag{5.20}$$

Writing the effective surface tension for the spectrum $\langle|\tilde{h}_n(q)|^2\rangle$ in analogy to Eq. 5.5 as

$$\tilde{\gamma}_{\mathrm{eff},n}(q) = \gamma_0 + \tilde{\kappa}_n q^2 + \mathcal{O}(q^4) \tag{5.21}$$

and defining the isothermal compressibility $\kappa_{\mathrm{T},||}$ of a slab,

$$S^b_{||}(q) = k_\mathrm{B}T\rho_l\kappa_{\mathrm{T},||} + \mathcal{O}(q^2), \tag{5.22}$$

we obtain in the low-q limit the relation

$$\kappa_n = \tilde{\kappa}_n + \gamma_0^2\alpha w\kappa_{\mathrm{T},||}. \tag{5.23}$$

This shows that correct subtraction of the bulk-like fluctuations is the key to extracting the correct interfacial bending rigidity κ_n.

In Fig. 5.7 b we show the spectra $q^2\langle|\tilde{h}_n(q)|^2\rangle \sim \tilde{\gamma}^{-1}_{\mathrm{eff},n}(q)$ (upper data points) and $q^2\langle|h_n(q)|^2\rangle \sim \gamma^{-1}_{\mathrm{eff},n}(q)$ (lower data points) for fixed $n = 64$ and different α. In contrast to a similar data analysis of colloid-polymer interfaces [99], we subtract the bulk structure factor $S^b_{||}$ of a corresponding slab of thickness αw without any fitting parameter. This is an important detail, since the functional form of $S^b_{||}(q)$ strongly depends on α (see App. A). As seen in Fig. 5.7 b, all data for $q^2\langle|h_n(q)|^2\rangle$ collapse onto a single curve, which shows that i) the parameter α does not influence the final result for κ_n, and ii) our method for subtracting bulk-like density fluctuations is consistent. Not surprisingly, for $\alpha = 1$ (circles) the data slightly deviate, indicating that this prism size is too small to entirely capture the interface fluctuations. The dashed lines in Fig. 5.7 b show the limiting behavior $\tilde{\gamma}_{\mathrm{eff},n}(q \to 0) = \gamma_{\mathrm{eff},n}(q \to 0) = \gamma_0$ with $\gamma_0 = \gamma_{\mathrm{lv},0} = 52.91\,\mathrm{mN/m}$ determined independently from the anisotropy of the pressure tensor [237]. In Fig. 5.7 c we plot $\gamma_{\mathrm{eff},n}(q)/\gamma_{\mathrm{lv},0}$ as a function of q^2 for fixed $\alpha = 3$ and various n and compare with straight line fits of the form $\gamma_{\mathrm{eff},n}(q)/\gamma_{\mathrm{lv},0} = 1 + \kappa_n q^2/\gamma_{\mathrm{lv},0}$.

The resulting n-dependence of the κ_n values is introduced by the coarse-graining of the local GDS method. From Eq. (5.10) we obtain

$$\langle|\tilde{h}_n(\vec{q})|^2\rangle = |g_n(\vec{q})|^2\langle|\tilde{h}(\vec{q})|^2\rangle, \tag{5.24}$$

where

$$g_n(\vec{q}) = \frac{4}{(\Delta L)^2 q_x q_y}\sin(\frac{\Delta L q_x}{2})\sin(\frac{\Delta L q_y}{2}) \tag{5.25}$$

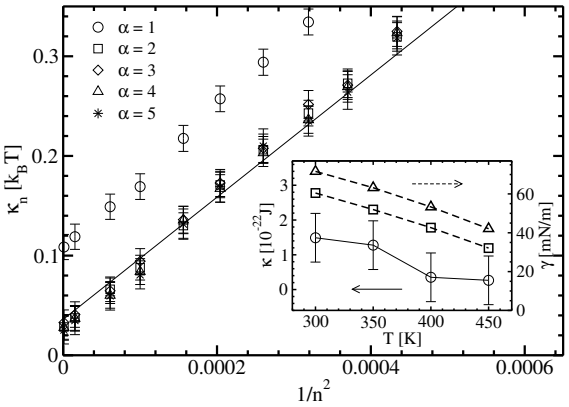

Figure 5.8.: Bending rigidity κ_n from fits in Fig. 5.7 c as a function of the inverse squared block factor $1/n^2$ for different α. The line denotes a fit of Eq. (5.26) to the data for $\alpha = 2-5$ yielding a value of $\kappa = 0.04\ k_B T$ as $n \to \infty$. The inset shows the temperature dependence of κ (circles), the simulated surface tension (squares, including a tail correction) and the experimental surface tension (triangles, [237]).

is the Fourier transform of the rectangular coarse-graining function $g_n(\vec{r}_{||})$. For small q we have $g_n(\vec{q}) \simeq 1 - (\Delta L)^2 q^2/24$. Combining this with Eq. 5.5 we obtain $\gamma_{\mathrm{eff},n} = \gamma_0 + \kappa q^2 + \gamma_0 L^2 q^2/(12n^2)$, where we have used that $\Delta L = L/n$. The asymptotic bending rigidity κ is thus related to κ_n as

$$\kappa_n = \kappa + \gamma_0 L^2/(12n^2). \tag{5.26}$$

In Fig. 5.8 we show κ_n for different α as a function of $1/n^2$. Except for $\alpha = 1$, the data for different slabthickness αw collapse, reinforcing our earlier statement that we have separated density and interface fluctuations in a consistent way. From Eq. (5.26), shown by the solid line, the bending rigidity follows by extrapolation to $n \to \infty$ as $\kappa = (0.04 \pm 0.02)\ k_B T$ at $T = 300$ K for a Lennard-Jones cut-off $r_c = 0.8$ nm. The temperature dependence of κ (inset in Fig. 5.8, circles) is similar to that of the surface tension from simulations (squares) or experiments (triangles). As a consequence, the cross-over length scale between bending and tension, $\sqrt{\kappa/\gamma_0}$, is of the order of about 0.5 Å and rather independent of temperature.

Our results, yielding a monotonously increasing effective surface tension, i.e., a positive bending rigidity, on first glance conflict with previous calculations including the long-ranged VDW tail that predict a negative slope of $\gamma_{\mathrm{eff}}(q)$ for small q [91]. In MD simulations, however, the VDW interaction is truncated at a finite cutoff length

r_c. The contribution of an attractive intermolecular interaction $w(r)$ to the bending rigidity is given in the sharp-kink approximation by [91]

$$\kappa_{\text{attr}} = \frac{\pi}{32}(\Delta\rho)^2 \int_{\sigma}^{r_c} dr r^5 w(r). \tag{5.27}$$

For the attractive part of the Lennard-Jones potential in the simulations, $w(r) = -4\epsilon(\sigma/r)^6$ with $\epsilon = 0.65\,\text{kJ/mol}$ and $\sigma = 0.317\,\text{nm}$, we obtain for the upper cut-offs $r_c = 0.8\,\text{nm}$ and $1.6\,\text{nm}$ the contributions $\kappa_{\text{attr}} = -0.11\,k_BT$ and $-0.19\,k_BT$ at $T = 300\,\text{K}$, yielding a difference of $-0.08\,k_BT$. In the limit $r_c = \infty$ Eq. 5.27 predicts a divergent contribution. In reality, retardation effects change the VDW distance dependence from $1/r^6$ to $1/r^7$ at a cross-over length on the order of $r_{\text{ret}} = 100\,\text{nm}$ [238]. Using $w(r) = -4\epsilon(\sigma/r)^6$ for $r < r_{\text{ret}}$ and matching continuously a function $w(r) \sim -1/r^7$ for $r > r_{\text{ret}}$, we obtain $\kappa_{\text{attr}} = -0.67\,k_BT$. Assuming simple additivity of the long-ranged contribution κ_{attr} to the simulation result would result in a negative value $\kappa = (-0.63 \pm 0.02)\,k_BT$. In fact, the same analysis as in Fig. 5.8 for simulations with a cut-off $r_c = 1.6$ nm yields a slightly smaller bending rigidity of $\kappa = (0.03 \pm 0.02)\,k_BT$, so it seems plausible that in the infinite cut-off limit κ becomes negative.

5.3. Solvation of spheres and cylinders

5.3.1. Curvature expansion of free energies

In this section we determine the elastic constants of the water surface by considering the solvation of spherical and cylindrical hydrophobic solutes. For a sphere with radius R one obtains from Eq. 5.3

$$\Delta F_{\text{SPH}}/A = \gamma_0 - \frac{4\kappa c_0}{R} + (2\kappa + \bar{\kappa})\frac{1}{R^2}, \tag{5.28}$$

with $\gamma_0 \equiv \tilde{\gamma} + 2\kappa c_0^2$. Comparison of the leading terms in Eqs. 5.1 and 5.28 shows that the Tolman length is given by $\delta = 2\kappa c_0/\gamma_0$. For a cylinder of radius R Helfrich's curvature expansion yields

$$\Delta F_{\text{CYL}}/A = \gamma_0 - \frac{2\kappa c_0}{R} + \frac{\kappa}{2}\frac{1}{R^2}, \tag{5.29}$$

and therefore the equivalent of Eq. 5.1 is

$$\gamma_{\text{CYL}} = \gamma_0 \left(1 - \frac{\delta}{R}\right). \tag{5.30}$$

By considering the full radius range from zero to $R = 2$ nm, we cover the crossover between the regimes where the solvation free energy scales as the cavity volume (for $R < R^*$) and where it scales as the surface area (for $R > R^*$). Simultaneously considering spherical and cylindrical geometries allows an additional consistency check on Eqs.

5.1 and 5.30 (which is essential in light of the pronounced crossover effects present, as will be shown below) and to reliably extract the Tolman length.

The range of applicability of Eqs. 5.28 and 5.29 can be extended by including higher order terms. If we include terms up to third order in the curvature, the Helfrich free energy is given by

$$\begin{aligned}\Delta F = \int dA\Big[\tilde{\gamma} + 2\kappa\left(\frac{1}{2}\left(\frac{1}{R_1}+\frac{1}{R_2}\right)-c_0\right)^2 + \bar{\kappa}\frac{1}{R_1R_2} \\ + \eta\left(\frac{1}{R_1^3}+\frac{1}{R_2^3}\right)+\bar{\eta}\left(\frac{1}{R_1R_2^2}+\frac{1}{R_1^2R_2}\right)\Big],\end{aligned} \tag{5.31}$$

where we have introduced the moduli η and $\bar{\eta}$. For a spherical solute Eq. 5.31 yields,

$$\Delta F_{\mathrm{SPH}}/A = \gamma_0 - \frac{4\kappa c_0}{R} + (2\kappa+\bar{\kappa})\frac{1}{R^2} + 2(\eta+\bar{\eta})\frac{1}{R^3}, \tag{5.32}$$

for a cylindrical solute,

$$\Delta F_{\mathrm{CYL}}/A = \gamma_0 - \frac{2\kappa c_0}{R} + \frac{\kappa}{2}\frac{1}{R^2} + \eta\frac{1}{R^3}. \tag{5.33}$$

Unless specified otherwise, the radius of the solutes, R, is defined as the distance where the interaction is k_BT_0, $V_{\mathrm{SOL-OW}}(R) = k_{\mathrm{B}}T_0$, where k_{B} is the Boltzmann constant and $T_0 = 300\,\mathrm{K}$, alternative radius definitions lead to minor modifications, as is discussed below.

5.3.2. Small scale solvation regime and crossover

The radial distribution functions in Fig. 5.2 c and f and the solvation entropy ΔS in Fig. 5.9 clearly display the gradual crossover from small-scale solvation (negative solvation entropy, strong density peak in the first solvation shell) to large-scale solvation characterized by a monotonic density distribution around the solute, positive ΔS and constant free energy per area $\Delta F/A$. Depending on the observable one looks at, this crossover occurs around $R^* \simeq 0.5 - 1.0$ nm and at a significantly smaller radius for a cylinder compared to a sphere (which makes cylinders particularly suited for determining the Tolman length, as shown later on). Note that $\Delta F/A$ does not quite reach the independently determined planar liquid vapour surface tension $\gamma_{\mathrm{lv},0}$, dotted horizontal line in Fig. 5.9 a, as will be discussed below.

For small radii the solvation free energy of hard-sphere solutes scales proportional to the volume [40, 41], whereas our Buckingham solutes exhibit for very small R a divergence in $\Delta F/V$. This is due to the finite $r \to 0$ limit of the Buckingham potential. It vanishes for a potential shape, that diverges with $r \to 0$, as is seen in Fig. 5.10, where we plot the solvation free energy for spherical solutes that interact with the water oxygen atoms via a purely repulsive Lennard-Jones (LJ) potential of the form

$$V^{\mathrm{LJ}}_{\mathrm{SPH-SOL}}(r) = \frac{E}{r^{12}}. \tag{5.34}$$

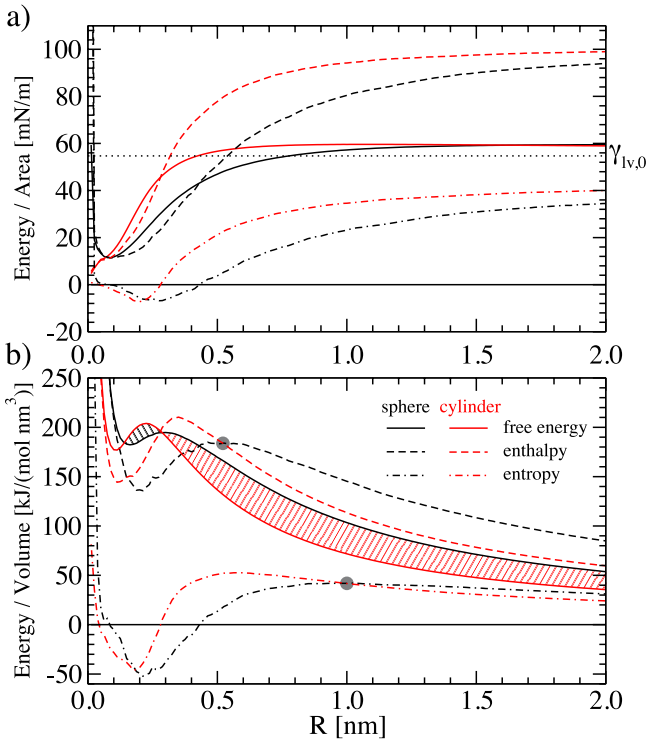

Figure 5.9.: Solvation free energy ΔF (full), enthalpy ΔH (dashed) and entropy ΔS (dash-dotted lines) of spherical (black) and cylindrical (red lines) solutes as a function of the solute radius R, plotted (a) per unit surface area and (b) per unit volume of the solutes. The dotted horizontal line shows the independently determined surface tension of a planar liquid vapour interface $\gamma_{lv,0}$.

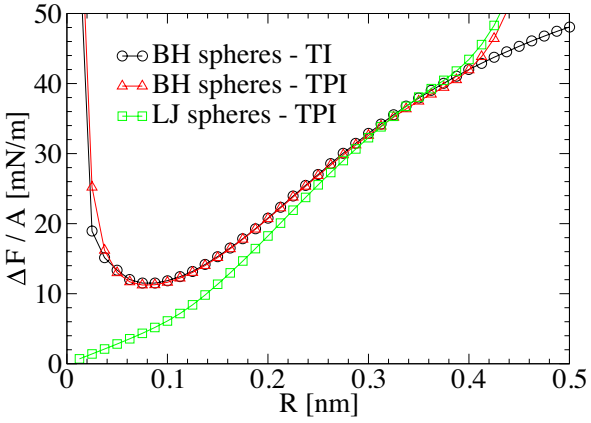

Figure 5.10.: Solvation free energy ΔF per solute surface area A as a function of the solute radius R for purely repulsive spherical solutes interacting with the water oxygen atoms either by a Buckingham (BH) (see Eq. 2.1) or by a Lennard-Jones (LJ) potential (see Eq. 5.34) obtained by either the test particle insertion (TPI) or the thermodynamic integration (TI) method. All data is obtained in SPC/E water at $T = 300\,\mathrm{K}$ and $p = 1\,\mathrm{bar}$.

Solute radii R are defined analogously to the Buckingham potential by $V^{\mathrm{LJ}}_{\mathrm{SPH-SOL}}(R) = k_{\mathrm{B}}T_0$. The solvation free energy of the LJ-spheres are obtained by the test particle insertion method. They are shown in Fig. 5.10 together with solvation free energies for Buckingham spheres obtained by both TI and TPI. The solvation free energy per unit area of the LJ-spheres smoothly goes to 0 for $R \to 0$, while it converges with the solvation free energy of the Buckingham-spheres for radii $R > 0.2\,\mathrm{nm}$. The TPI data for the Buckingham-spheres agree perfectly with the Buckingham TI data for small radii. Deviations from the TI data for $R > 0.4\,\mathrm{nm}$ are due to insufficient sampling, which shows that the TPI method is not applicable for solutes of too large size. We note that the solvation free energy ΔF of the Buckingham solutes of course goes to zero for $R \to 0$, only slower than the area A.

The difference between $\Delta F/V$ for spheres and cylinders in Fig. 5.9 b gives the free energy change per volume upon an aggregation of spheres into a cylinder with the same radius, which is an idealized model for linear hydrophobic aggregation. Surprisingly, only for $R > 0.3$ nm is this aggregation favored (red shaded region), for smaller R the cylindrical free energy per volume is higher than the spherical one (black shaded region). This transition is driven by complex crossovers in the enthalpic and entropic differences [44], which change sign at $R \simeq 0.5$ nm and $R \simeq 1.0$ nm, respectively, as indicated by filled circles: For $R > 1.0$ nm cylinders are enthalpically favored (and entropically disfavored), while for $R < 0.5$ nm cylinders are entropically favored (and enthalpically disfavored).

5.3.3. Large scale solvation regime

To extract the Tolman length, in Fig. 5.11 a we plot $\Delta F/A$ for $T = 300$ K as a function of the inverse radius $1/R$ as solid lines. The data are strongly curved and fits according to Eqs. 5.1 and 5.30 are obviously impossible: The slopes for cylinders and spheres at $1/R = 0.5\ \mathrm{nm}^{-1}$ have opposite signs, so extrapolation to the limit $1/R \to 0$ and extraction of the Tolman length (which is the slope in this plot) is not obvious. The situation for higher temperature $T = 360$ K in Fig. 5.11 b is more favorable, since here crossovers are shifted to smaller radii [44]. Indeed, now a maximum in $\Delta F/A$ is clearly resolved in both data sets, although a linear fit according to Eqs. 5.1 and 5.30 is still not feasible. The dashed-dotted lines in Fig. 5.11 a and b show a simultaneous fit to both spherical and cylindrical data according to Eqs. 5.32 and 5.33 with γ_0, δ, κ, $\bar{\kappa}$, η and $\bar{\eta}$ as free parameters (fits are performed on the interval $0.5\ \mathrm{nm}^{-1} < 1/R < 1.4\ \mathrm{nm}^{-1}$). The influence of the cubic term and the dependence on the fitting range is discussed below.

The fit parameters are summarized in Tab. 5.1. The resulting Tolman length is negative, on the order of $\delta \approx -1$ Å and decreasing with temperature, implying that the spontaneous curvature is such that water favors droplets over cavities. The maximum of $\Delta F/A$ for spheres occurs at $1/R_{\mathrm{max}} \simeq 0.7\ \mathrm{nm}^{-1}$ for $T = 360$ K and extrapolated at $1/R_{\mathrm{max}} \simeq 0.5\ \mathrm{nm}^{-1}$ for $T = 300$ K, consistent with previous simulations [42] for spheres and for $1/R > 1\ \mathrm{nm}^{-1}$ that were interpreted in terms of a positive Tolman

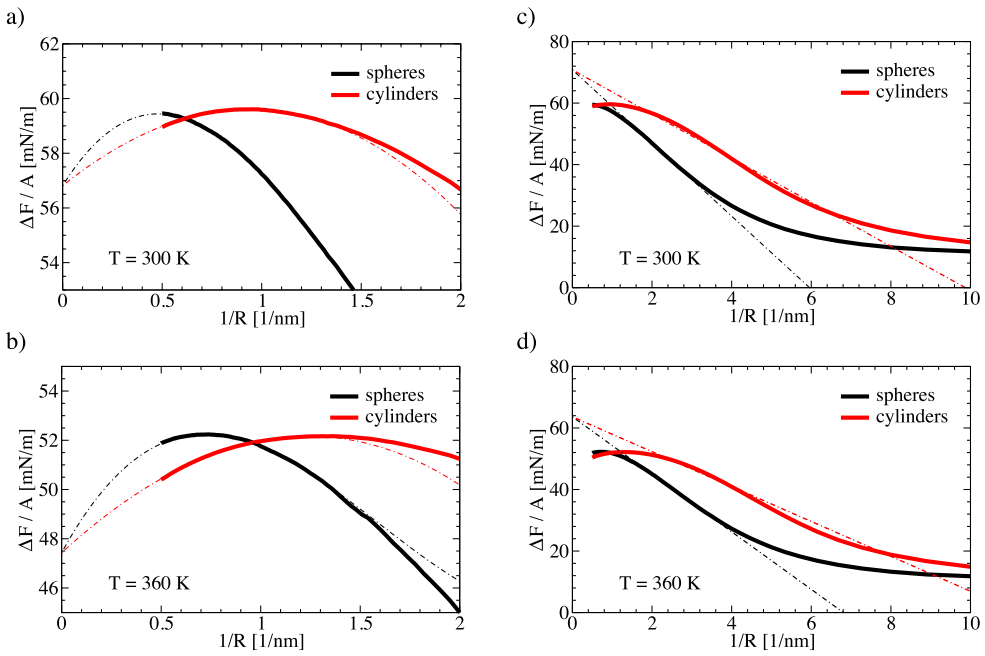

Figure 5.11.: Solvation free energies ΔF (full lines) per unit area of spherical (black) and cylindrical (red lines) solutes as a function of the inverse radius $1/R$ at temperatures (a) $T = 300$ K and (b) $T = 360$ K. Dashed-dotted lines are cubic fits in the range $0.5\ \mathrm{nm}^{-1} < 1/R < 1.4\ \mathrm{nm}^{-1}$, where Eqs. 5.32 and 5.33 are fit simultaneously to the data for spherical and cylindrical solutes. The resulting best-fit parameters are listed in Tab. 5.1. [(c),(d)] Same data as in (a) and (b) but for a larger range of $1/R$. Linear fits in the region $1.5\ \mathrm{nm}^{-1} < 1/R < 3\ \mathrm{nm}^{-1}$ for spheres and $3\ \mathrm{nm}^{-1} < 1/R < 5\ \mathrm{nm}^{-1}$ for cylinders (dashed-dotted lines) with the constraint of an equal surface tension are included.

Table 5.1.: Best fit parameters γ_0, κ, $\bar{\kappa}$, c_0, δ, η and $\bar{\eta}$ obtained from fitting Eqs. 5.32 and 5.33 to the spherical and cylindrical data in Fig. 5.11 a and b. The independently determined planar surface tension of the free water/vapour interface, $\gamma_{\mathrm{lv},0}$, is included for comparison.

T [K]	$\gamma_{\mathrm{lv},0}$ [mN/m]	γ_0 [mN/m]	c_0 [nm^{-1}]	δ [nm]
280	58.1	59.7	0.41	-0.092
300	54.7	56.8	0.50	-0.10
320	52.0	53.8	0.53	-0.12
360	45.5	47.4	0.69	-0.16

T [K]	κ [10^{-21} J]	$\bar{\kappa}$ [10^{-21} J]	η [10^{-32}Jm]	$\bar{\eta}$ [10^{-32}Jm]
280	-6.7	-2.4	0.018	3.2
300	-5.8	-2.8	-0.23	3.0
320	-6.2	-2.3	-0.23	3.2
360	-5.4	-2.5	-0.35	3.3

length. The increased radius range up to $R = 2$ nm in conjunction with the cylindrical data, that show the crossover at considerably smaller radii, allows to clearly resolve the maximum in $\Delta F/A$ and thus to reliably extract the Tolman length. The best-fit values for γ_0 are slightly larger than the surface tension $\gamma_{\mathrm{lv},0}$ of the planar liquid/ vapour interface. Similar behaviour for a Lennard-Jones liquid [80] was rationalized by suppressed interfacial fluctuations near a hard wall [239], as we will show in the following this can also be interpreted as a finite-size crossover.

Figure 5.12 shows fits according to Eqs. 5.32 and 5.33 including (dashed-dotted lines) and neglecting (dotted lines) the cubic term. The fitting is performed over the interval 0.5 nm^{-1} $< 1/R < (1/R)_{\mathrm{upper}}$, where $(1/R)_{\mathrm{upper}} = 0.6$ and 1.4 nm^{-1}. The dependence of the fitted surface tension and Tolman length on the fitting range is shown in Fig. 5.13.

As can be seen from Fig. 5.12, for small curvature $1/R$ the deviations between the quadratic and cubic fit are quite small. For larger curvature the cubic function fits the data better than the quadratic one, since higher order corrections become more important in this region. The planar surface tension and the Tolman length obtained from the fits show only a slight dependence on the fitting range (see Fig. 5.13). The planar surface tension γ_0 decreases with decreasing $(1/R)_{\mathrm{upper}}$, suggesting that the discrepancy between the γ_0 obtained from the fit and the surface tension obtained from simulations of a planar air/water interface $\gamma_{\mathrm{lv},0}$ can be explained by the finite minimal curvature that is accessible by these simulations. Indeed, if we extrapolate γ_0 to $(1/R)_{\mathrm{upper}} = 0$ it agrees within the statistical errors with $\gamma_{\mathrm{lv},0}$ which is indicated by a dotted horizontal line.

For the bending rigidities we find negative values on the order of $\kappa, \bar{\kappa} \approx -1$ to $-10\ k_{\mathrm{B}}T$ with only small dependencies on the LJ cutoff length (see App. B), consistent

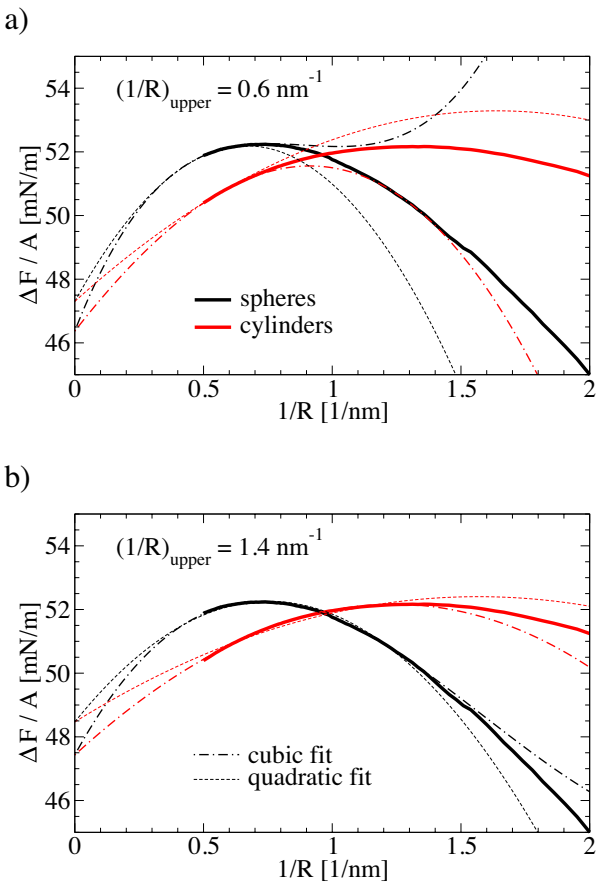

Figure 5.12.: Solvation free energies per area for spherical and cylindrical solutes at $T = 360$ K and $p = 1$ bar, simultaneously fit by Eqs. 5.32 and 5.33 either neglecting (dashed lines) or including (dashed-dotted lines) the cubic term. The fit is restricted to the range 0.5 $nm^{-1} < 1/R < (1/R)_{upper}$, where (a) $(1/R)_{upper} = 0.6$ nm^{-1} and (b) $(1/R)_{upper} = 1.4$ nm^{-1}.

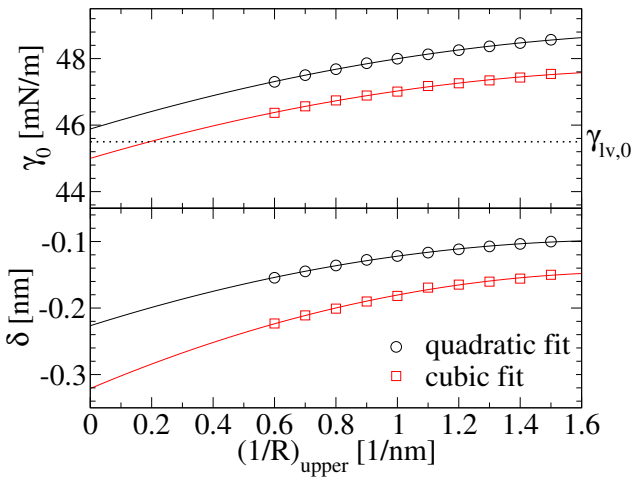

Figure 5.13.: Dependence of the best fit parameters of the fits to the solvation free energies per area of spherical and cylindrical solutes at $T = 360$ K and $p = 1$ bar for a quadratic (black circles) or cubic (red squares) fitting function (see Fig. 5.12) on the fitting range 0.5 $nm^{-1} < 1/R < (1/R)_{upper}$. Solid lines are quadratic fits to the data, the dotted line indicates $\gamma_{lv,0} = 45.5$ mN/m.

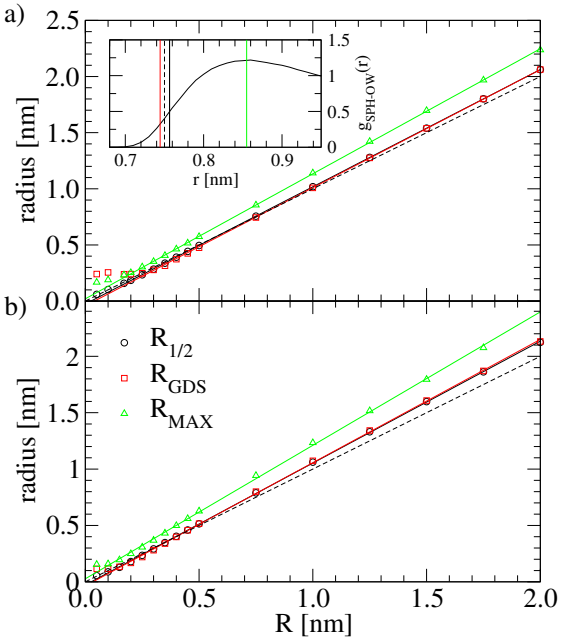

Figure 5.14.: Comparison of various definitions for the radius of (a) spherical and (b) cylindrical solutes in SPC/E water at $T = 300\,\mathrm{K}$. Shown are the radii $R_{1/2}$, defined by $g_{X-OW}(R_{1/2}) = 1/2$, R_{GDS}, the radius of the Gibbs dividing surface (GDS) and R_{MAX}, the radius of the maximum of the radial distribution function $g_{X-OW}(r)$, as a function of the reference radius R, defined by $V_{X-OW}(R) = k_B T_0$, with X = SPH or CYL. Solid lines are linear fits to the data. The dashed line marks the identity. In the inset the radial distribution function $g_{SPH-OW}(r)$ for a spherical solute with $R = 0.75\,\mathrm{nm}$ is shown and the different definitions of the radius are indicated by vertical lines.

with the estimates from the capillary wave fluctuations, that included a long-range LJ correction.

The elastic coefficients in Eqs. 5.3 and 5.31 depend on the definition of the radius R, for which there are several common choices: (i) the radius $R_{1/2}$, defined by $g_{X-OW}(R_{1/2}) = 1/2$, (ii) the radius R_{GDS}, defined by the Gibbs dividing surface (GDS), that is defined by

$$\int d^3r \left[g_{X-OW}(r) - \theta(r - R_{GDS}) \right] = 0, \tag{5.35}$$

where $\theta(x) = 1$ if $x \geq 0$ and $\theta(x) = 0$ if $x < 0$, in accordance with the interface definition in Sec. 5.2, and (iii) the radius R_{MAX}, defined as the first maximum of the radial distribution function $g_{X-OW}(r)$. In Fig. 5.14 we compare alternative definitions. It is seen that, except for R_{MAX}, all other radii differ only slightly from R. For radii $R > 0.2\,\mathrm{nm}$ the curves are well fit by a linear function, if we allow for a non-zero offset. For small radii $R < 0.2\,\mathrm{nm}$, there are deviations from the linear dependence, which are caused by the finite $r \to 0$ limit of the Buckingham potential as discussed above. Note that the GDS based radius definition is thermodynamically the most sound definition, but requires extensive additional simulations for accurate determination. The heuristic radius definition we use in most parts of Sec. 5.3 is the most practical one, since it does not require additional simulations; this is the reason why we used it.

If we generally assume a linear relationship between an alternative definition of the solute radius, R', and R, $R = R'(1+\epsilon)+\Delta$, then we obtain to linear order in $1/R'$ for a sphere,

$$\begin{aligned} \Delta F &= 4\pi R^2\gamma_0\left(1-\frac{2\delta}{R}+\mathcal{O}(\frac{1}{R^2})\right)= \\ &= 4\pi R'^2\gamma_0(1+\epsilon)^2\left(1-\frac{2(\delta-\Delta)}{R'(1+\epsilon)}+\mathcal{O}(\frac{1}{R'^2})\right). \end{aligned} \tag{5.36}$$

The Tolman length associated with R' is therefore given by

$$\delta' = \frac{\delta-\Delta}{1+\epsilon}. \tag{5.37}$$

For R_{GDS} and $R_{1/2}$ we obtain $\epsilon = -0.049$ and -0.042 and $\Delta = 0.040$ nm and 0.025 nm, leading to $\delta' = -0.14$ nm and -0.12 nm at $T = 300$ K. From a direct fit using the same fitting procedure as described in the main paper, but taking R_{GDS} as dividing surface, we obtain $\gamma_0 = 52.6$ mN/m, $c_0 = 2.73$ nm^{-1}, $\kappa = -0.98\times10^{-21}$ J, $\bar{\kappa} = -6.49\times10^{-21}$ J and $\delta = -0.10$ nm at $T = 300$ K. While the Tolman length does not change significantly, the bending rigidities, which constitute higher-order curvature corrections, not surprisingly do. So our results for the bending rigidities should only be regarded as indicative. The Tolman lengths obtained from the direct fit and from Eq. 5.37 differ slightly, since the fit range is restricted by the finite minimum curvature.

Finally, we stress that the expressions in Eqs. 5.1 and 5.30 strictly only apply to the asymptotic small-curvature regime, i.e. to radii $R > R_{\mathrm{max}}$, because otherwise higher-order curvature terms take over. Curiously, as can be seen in Fig. 5.11 c and d, there is an intermediate range where $\Delta F/A$ scales linear in $1/R$ with effective Tolman lengths $\tilde{\delta}_{\mathrm{SPH,CYL}}$ that are positive and on the order of 1 Å (see Tab. 5.2), in rough agreement with previous estimates [42, 43, 83, 85]. It is clear that such a fit at intermediate radii is incompatible with a surface free energy functional in terms of local curvatures and rather illustrates the subtleties of analyzing simulation data.

5.4. Conclusion

We have presented a thorough analysis of the curvature dependence of the free energy of a water surface, taking into account both, fluctuations of an planar air/water interface and surfaces forced to curve due to the presence of a solute.

Considering the free air/water interface, we have introduced a method to consistently separate surface and bulk contributions to the interfacial structure factor of large scale water simulations. It is found that in the limit of small q the effective surface tension is well described by a small but positive bending rigidity on the order of $\kappa = (0.04\pm0.02)\ k_{\mathrm{B}}T$ at $T = 300$ K. Considering the long-ranged and retarded

Table 5.2.: Best fit parameters $\tilde{\delta}_{\mathrm{SPH}}$ and $\tilde{\delta}_{\mathrm{CYL}}$ from Eqs. 5.1 and 5.30 in the intermediate radius range in Fig. 5.11 c and d. The Tolman length δ as obtained from the fit to the asymptotic region is also included for comparison (see Tab. 5.1).

T [K]	δ [nm]	$\tilde{\delta}_{\mathrm{SPH}}$ [nm]	$\tilde{\delta}_{\mathrm{CYL}}$ [nm]
280	-0.092	0.087	0.11
300	-0.10	0.084	0.10
320	-0.12	0.080	0.097
360	-0.16	0.073	0.089

van-der-Waals contribution (which is not fully accounted for in MD simulations) negative values of κ are suggested in agreement with coarse-grained theories [91] and X-ray scattering experiments [95]. The broadening of the water interface exhibits a crossover at a lateral length scale of ≈ 0.8 nm: On smaller scales the interface is intrinsically rough due to surface reconstruction of the hydrogen bonding network, for larger scales capillary waves are dominant.

We have further found a maximum in the solvation free energy per area, $\Delta F/A$, for hydrophobes in water, which implies that both the Tolman length and the bending rigidities characterizing the water-hydrophobe interface are negative. This maximum occurs between radii of $R_{\mathrm{max}} = 2$ nm (for spheres at $T = 300$ K) and $R_{\mathrm{max}} = 0.8$ nm (for cylinders at $T = 360$ K). A simultaneous fit of sphere and cylinder data yields a negative Tolman length of $\delta = -0.1$ nm at $T = 300$ K for a hydrophobic surface, which means that droplets are favored over cavities, with important implications for current coarse-grained modelling [219]. For cylinders in water at room temperature, the Tolman length $\delta \simeq -0.1$ nm, the radius $R_{\mathrm{max}} \simeq 1$ nm where $\Delta F/A$ shows an extremum (which scales like the inverse spontaneous curvature, $R_{\mathrm{max}} \simeq c_0^{-1}$), and the crossover radius $R^* \simeq 0.5$ nm between small-scale (where $\Delta F \sim V$) and large-scale solvation (where $\Delta F \sim A$) are quite similar, which requires a careful numerical analysis. Still, our results suggest that for curvature radii $R > R_{\mathrm{max}}$, a curvature-based local interface free energy functional is valid for arbitrarily shaped solutes and the linear Tolman correction is dominant. For smaller radii, corrections have to be accounted for, either in the form of higher-order curvature terms (involving additional independent elastic constants) or in terms of effective functionals that correctly account for the crossover to the small-scale solvation regime.

It appears that the thermodynamic crossover seen in the solvation of hydrophobes is paralleled by the structural crossover seen at the water surface, which suggests that both are of the same origin, that is the relatively open structure of the hydrogen bonding network of water.

CHAPTER 6

WATER DYNAMICS NEAR HYDROPHOBIC AND HYDROPHILIC SOLUTES AND INTERFACES

6.1. Introduction

6.1.1. Motivation

In this final chapter we turn to the investigation of the dynamics of single water molecules near interfaces. Water dynamics is important not only in its own right but also because it influences the kinetics of many other processes that take place in an aqueous environment, for example protein folding [102]. The modeling of water dynamics in bulk and at surfaces steadily progressed over the least years. A prominent goal in recent water research has been to relate macroscopic dynamic properties, such as the viscosity, to microscopic kinetic events and thus to the hydrogen bonding dynamics between individual water molecules [16]. Yet, even for the most elementary kinetic process of breaking a single hydrogen bond between two water molecules that are embedded in the bulk liquid matrix, no clear picture exists. One particular problem is to disentangle the influence of the free energy profile and the local friction on the kinetics of processes that involve water.

6.1.2. Outline

In this chapter we study the dynamics of single water molecules at interfaces and solutes using molecular dynamics simulations. Special attention is paid to differences between hydrophobic and hydrophilic solutes and interfaces. We report recent progress on the interpretation of simulation data using a Fokker-Planck based formalism that allows to extract and disentangle the free energy and diffusivity profiles of various dynamic processes, an important distinction previously drawn using a similar approach for systems of hard-spheres [122].

We first study the water dynamics at planar boundaries and derive water diffusivity profiles at hydrophilic and hydrophobic surfaces. Here we see a dramatic slowing down of water diffusion close to a hydrophilic surface that is distinct from the strong binding of water to such surfaces. We next study the water dynamics in bulk between two water molecules and close to a non-polar solute which is taken as a methane molecule. Similar to the surface case, we see substantial slowing down of water diffusion in the first solvation shell of a water-water hydrogen bond, the effect close to the methane molecule is less pronounced.

This chapter is organized as follows: The diffusional analysis is introduced in Sec. 6.2. Results for the dynamics of single water molecules at interfaces and close to solutes are presented and discussed in Sec. 6.3 and Sec. 6.4, respectively. Finally, based on our results, conclusions are drawn in Sec. 6.5.

6.2. Diffusional dynamics and analysis

In our analysis we assume that the dynamics of water molecules is accurately captured by an overdamped Fokker-Planck (FP) or Smoluchowski equation

$$\frac{\partial}{\partial t}\psi(q,t) = \frac{\partial}{\partial q}\left(D(q)\mathrm{e}^{-\beta F(q)}\frac{\partial}{\partial q}\left(\psi(q,t)\mathrm{e}^{\beta F(q)}\right)\right), \tag{6.1}$$

which describes diffusive motion along a general coordinate q. In the FP Eq. 6.1, where the inverse thermal energy is denoted by $\beta \equiv 1/\left(k_\mathrm{B}T\right)$, the time evolution of the probability density ψ of observing a value q at time t is subject to the free energy landscape F and the q-dependent diffusivity D. While the free energy $F(q) \equiv -k_\mathrm{B}T\log\psi_{\mathrm{eq.}}(q)$, the Boltzmann inverse of the equilibrium probability $\psi_{\mathrm{eq.}}(q)$, is a purely static quantity, dynamic time scales are set by the diffusivity profile $D(q)$.

In the following, free energies and diffusivity profiles are resolved for water dynamics in various contexts: water dynamics parallel ($q = x, y$) and perpendicular ($q = z$) to a planar interface as well as relative dynamics of pairs of water molecules and pairs of water and methane molecules, where $q = r$ denotes the radial separation between both molecules. While translation invariance parallel to an (unstructured) confining surface ensures a constant free energy $F(x) = F(y) = \text{const.}$, the free energy profile in direction perpendicular to the interface is given (up to arbitrary constant shifts) by

$$F(z) = -k_\mathrm{B}T\log\left(\rho(z)/\rho_{\mathrm{bulk}}\right), \tag{6.2}$$

where ρ denotes the density profile perpendicular to the interface. For the radial case of relative diffusion of molecule pairs the free energy is

$$F(r) = -2k_\mathrm{B}T\log r - k_\mathrm{B}T\log g(r), \tag{6.3}$$

i.e., the ideal entropic free energy is modified by the radial pair correlation function $g(r)$.

In the past, different approaches have been taken for determining (spatially varying) diffusion coefficients in various contexts ranging from simple liquids in confinement [122], dynamics of nano-confined water [115, 116], water dynamics at the air-water interface [240, 241] and the protein-water interface [242, 243] to protein dynamics [244–247]. While the Bayesian approach of Ref. [122] optimizes the diffusivity profile to maximize the likelihood of the series of transitions at fixed lag time observed in the simulation, we choose a complementary route which allows to extract the diffusivity based on two dynamic observables: mean square displacements and MFPTs. The methods used hereafter for characterizing water dynamics in bulk and at solid interfaces are described in the following.

6.2.1. Variance method

In cases, where both free energy $F(q) = \text{const.}$ and diffusivity $D(q) = \text{const.}$ are q-independent, the FP Eq. 6.1 reduces to the simple equation for free diffusion

$$\frac{\partial}{\partial t}\psi(q,t) = D\frac{\partial^2}{\partial q^2}\psi(q,t), \tag{6.4}$$

which is readily solved in terms of the Green's function

$$\psi(q,t) = \frac{1}{\sqrt{4\pi D t}}\exp -\frac{(q-q_0)^2}{4Dt}, \tag{6.5}$$

specifying the probability of observing q a time t after a given start in q_0. In these cases either the direct comparison of histograms from trajectory data with Eq. 6.5 or the evaluation of the second central moment or variance

$$\left\langle (q-q_0)^2 \right\rangle = 2Dt, \tag{6.6}$$

allows to determine the value of the diffusion coefficient D. Note, that because of non-Markovian (ballistic) effects at short time scales, the diffusive description of Eq. 6.1 and thus also the linear temporal scaling of the variance in Eq. 6.6 generally only applies in the long time limit. This approach, hereafter named "variance method", is used for resolving the distance dependence of the water molecule diffusion coefficients parallel to planar interfaces in Sec. 6.3.2.

6.2.2. Mean first-passage time method

In cases where the Green's function solution to the FP Eq. 6.1 is not known analytically, an alternative approach [246] based on the evaluation of mean first-passage times (MFPTs) proves to be useful. For a diffusive process described by the FP Eq. 6.1, the MFPT τ_{fp} of first reaching a target value q_{t} when starting off from q [248] is given by

$$\tau_{\text{fp}}(q,q_{\text{t}}) = \int_q^{q_{\text{t}}} \mathrm{d}q' \, \frac{\mathrm{e}^{\beta F(q')}}{D(q')} \int_{q_{\text{min}}}^{q'} \mathrm{d}q'' \mathrm{e}^{-\beta F(q'')}, \tag{6.7}$$

where q_{min} denotes the position of a reflective (zero-flux) boundary. Differentiating Eq. 6.7, one readily obtains [246]

$$D(q) = -\frac{\mathrm{e}^{\beta F(q)}}{\partial \tau_{\mathrm{fp}}(q, q_{\mathrm{t}})/\partial q} \int_{q_{\mathrm{min}}}^{q} \mathrm{d}q' \mathrm{e}^{-\beta F(q')}. \tag{6.8}$$

Extracting MFPT curves τ_{fp} from simulation trajectories thus allows to determine the q-dependent diffusivity $D(q)$ governing the dynamics in an arbitrary free energy landscape $F(q)$. This approach, named "MFPT method" below, is used for determining various q-dependent diffusivity profiles: results for the dynamics of single water molecules perpendicular to planar interfaces are presented in Sec. 6.3.1 and relative diffusivity profiles in bulk are resolved in Sec. 6.4.

6.3. Water dynamics at interfaces

6.3.1. Diffusivity perpendicular to the interface

Diffusivity profiles perpendicular to the wall are resolved by the MFPT method described in Sec. 6.2.2. Using a spatial resolution $\Delta z = 0.01$ nm, all trajectories starting at a separation within $\Delta z/2$ from z and crossing $z_{\mathrm{t}} - \Delta z/2$ for the first time a time t_{fp} later contribute to the MFPT $\tau_{\mathrm{fp}} = \left\langle t_{\mathrm{fp}} \right\rangle$. The derivative $\partial \tau_{\mathrm{fp}}(z, z_{\mathrm{t}})/\partial z$ needed in Eq. 6.8 is determined by fitting a linear function to the MFPT values τ_{fp} within a small region of magnitude δz around z, where $\delta z = 0.07$ nm; this approach allows to smooth out the statistical noise in the MFPT curves without hiding the relevant features of the diffusivity profiles. For the evaluation of the integral in Eq. 6.8, the equilibrium distribution $\psi_{\mathrm{eq.}}(z) = \exp\left(-\beta F(z)\right)$ is linearly interpolated; results are shown together with the corresponding free energy profiles and MFPT curves in Fig. 6.1. The origin of the z axis is set to the Gibbs dividing surface, that is the dividing surface for which the excess density of the water vanishes.

Near the hydrophobic substrate the diffusivity shows several oscillations and then converges towards the bulk diffusivity, indicated by a horizontal broken line, for separations of $z \approx 0.7$ nm. Next to the surface the diffusivity drops to about 40% of the bulk value. Diffusivity minima and maxima are located in between maxima and minima of the free energy profile. Similar behaviour has been observed for a hard-sphere liquid in confinement [122], implying that layering effects are the cause for the oscillations. Note, that the water diffusivity in the "bulk" region of the slab, $D_{\mathrm{H_2O}} \approx 2.7$ nm^2/ns, is slightly larger than the diffusivity obtained from the bulk simulations (see below), since due to the lack of a long-range correction for the Lennard-Jones interaction in the interfacial geometry the water density is slightly smaller than in the bulk case.

The diffusivity near the hydrophilic walls (Fig. 6.1 b and c) shows a dramatic drop to roughly 4% and 1% of the bulk value for 12% and 25% OH coverage, respectively. This drop can be attributed to water molecules forming relatively long-lived hydrogen bonds with the surface OH groups and is in qualitative agreement with previous results

of Sendner et al. [34]. We emphasize that the drop in the diffusivity is not caused by the deep minimum in the free energy profile, which is also related to the formation of hydrogen bonds with the surface, since the free energy profile is a strictly static quantity. In other words, the water molecules near the hydrophilic wall are tightly bound and slow. However, we cannot rule out that there are other locally varying static quantities that do correlate with dynamic properties, such as the local available volume in the case of hard spheres in confinement [122]. The increase towards the bulk diffusivity, indicated by a horizontal broken line, which is reached at separations of $z \approx 1.1$ nm, is modulated by oscillations similar to the hydrophobic surface, but, for the case of 25% OH coverage, with different phase relations with respect to the free energy profile. This suggests that the mechanism behind the pronounced diffusivity profile variations is different at hydrophobic and hydrophilic substrates.

We note that very close to the substrates, the MFPT profiles exhibit a positive slope due to ballistic (i.e. non-Markovian) effects, and the analysis based on Eq. 6.8 breaks down.

6.3.2. Diffusivity parallel to the interface

Diffusion coefficients of water molecules parallel to planar interfaces are resolved using the variance method described in Sec. 6.2.1. Results are shown in the bottom panels of Fig. 6.1. Solid lines are obtained by determining the variance of the lateral displacement in Eq. 6.6 for an ensemble of water molecules with an initial z-position in the range $[z-\Delta z; z+\Delta z]$ and by fitting the variance over the time interval $[t-\delta t; t+\delta t]$, where we use $\Delta z = 0.01$ nm and $\delta t = 0.5$ ps. Dashed lines are obtained by analyzing a restricted ensemble of water molecules that stay in the slice $[z-\Delta z; z+\Delta z]$ for the entire time interval t and by solving Eq. 6.6 for D, with $\Delta z = 0.025$ nm. The first method allows to study the diffusion on longer time scales, where linear time scaling is valid, which comes at the price that the diffusivity profile is smeared out, since water molecules might cross several slices along the z-direction.

Fig. 6.2 shows several variance curves for water molecules starting at different initial separations from the hydrophilic diamond substrate with 25% OH coverage. On small time scales $t \lesssim 1.0$ ps the dynamics are dominated by ballistic motions and the variance scales with t^2; on longer time scales the motion becomes diffusive and the variance assumes a linear time dependence.

The lateral diffusivity profile near the hydrophobic wall in the bottom panel of Fig. 6.1 a is relatively featureless. There is a slight decrease towards the bulk diffusivity with increasing separation form the wall and one can discern two small peaks located at the first two minima of the free energy profile. Mittal et al. [122] have explained this effect by the fact that in inhomogeneous fluids the local available volume and therefore the diffusivity is higher in regions of higher density.

Near the hydrophilic substrates the lateral diffusivity decreases drastically, see the bottom panel of Figs. 6.1 b and c, however, the lateral diffusivity at the surface is still much larger than the perpendicular diffusivity. This suggests, that although the water

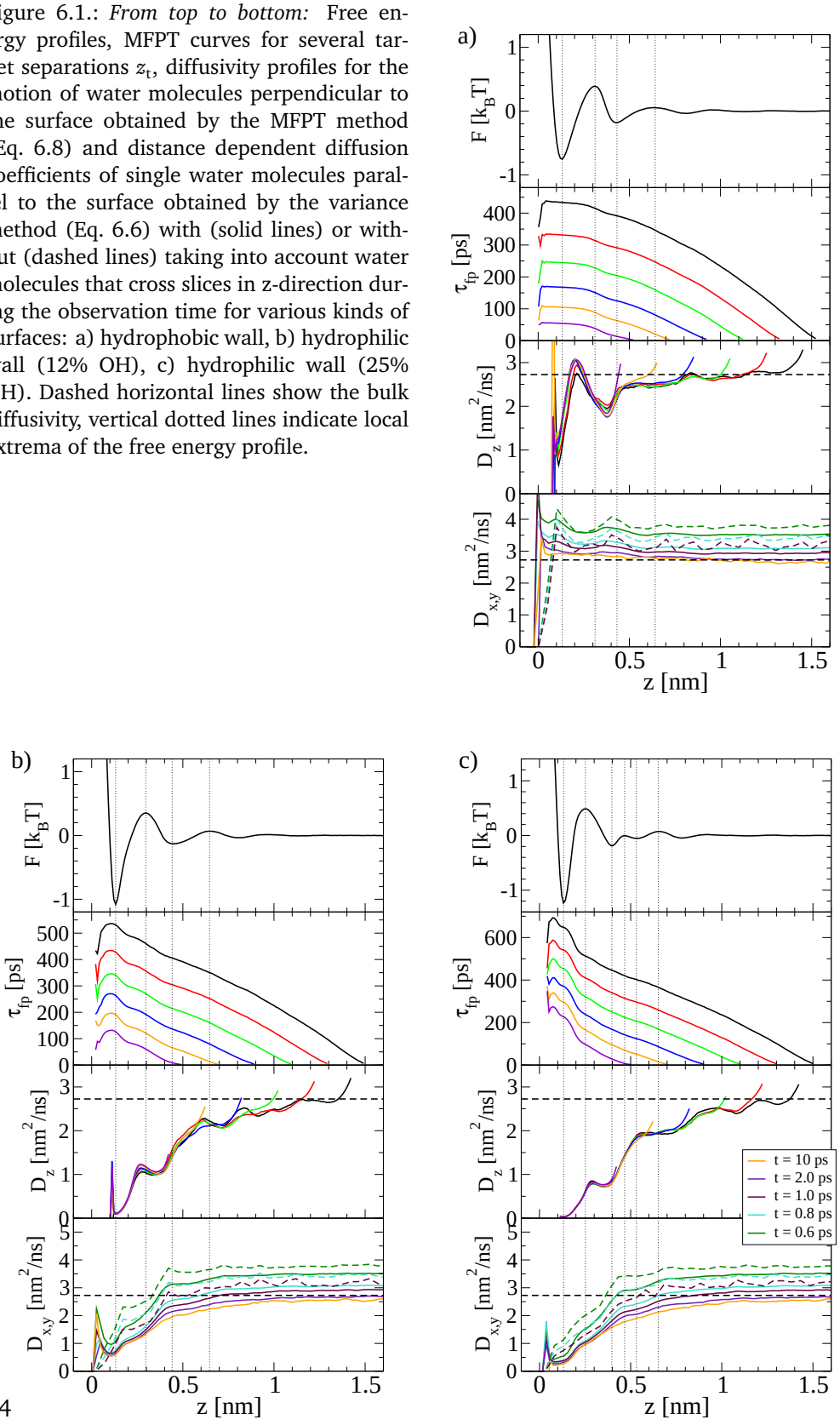

Figure 6.1.: *From top to bottom:* Free energy profiles, MFPT curves for several target separations z_t, diffusivity profiles for the motion of water molecules perpendicular to the surface obtained by the MFPT method (Eq. 6.8) and distance dependent diffusion coefficients of single water molecules parallel to the surface obtained by the variance method (Eq. 6.6) with (solid lines) or without (dashed lines) taking into account water molecules that cross slices in z-direction during the observation time for various kinds of surfaces: a) hydrophobic wall, b) hydrophilic wall (12% OH), c) hydrophilic wall (25% OH). Dashed horizontal lines show the bulk diffusivity, vertical dotted lines indicate local extrema of the free energy profile.

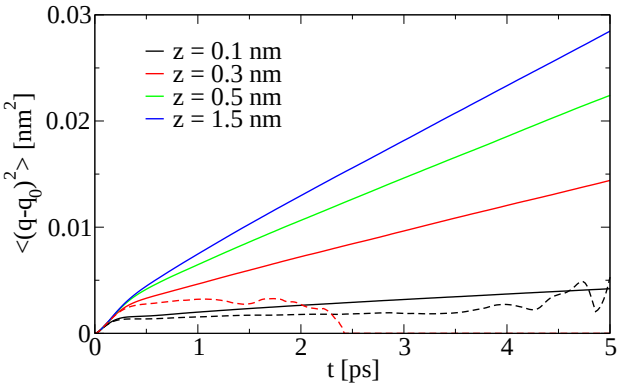

Figure 6.2.: Mean variance of the lateral diffusion (q=x,y) for water molecules starting at various separations $z = 0.1, 0.3, 0.5$ and 1.5 nm from a hydrophilic diamond substrate with 25% OH coverage (*solid lines*) and for water molecules staying in the interval $[z - \Delta z; z + \Delta z]$ with $\delta z = 0.025$ nm (*dashed lines*).

mobility perpendicular to the substrate is strongly reduced, water molecules can still move laterally to some extent. The fact, that the diffusivity profiles for all but the smallest analysis duration times t more or less coincide near the surface, shows again that the residence time of the water molecules is quite long [34], that is on average the water molecules do not cross the boundary of their initial bin during the observation interval t.

In a previous study Feng et al. [249] used the variance method to determine the parallel and perpendicular water diffusivity profiles at a substrate made of acetylated aminosilane linkers grafted on a silica surface. They also found a strongly oscillating perpendicular diffusivity with a decrease towards the surface but whose oscillations are in antiphase with the density profile. The shift in the phase relation might be caused by the use of the variance method in a situation with a non-uniform free energy profile, where the entanglement of free energetic and diffusivity effects requires a stochastic approach as used in this work; in fact, we observe a similar shift when employing the variance method instead of the MFPT method (data not shown). The parallel diffusivity profiles found by Feng et al. [249] are in qualitative agreement with our results.

6.3.3. Water orientation relative to the interface

As is illustrated in Fig. 6.3, the projections of the (unit) dipole vector $\hat{\mu}$ and of the unit vector along a water OH-bond $\hat{\eta}_{\mathrm{OH}}$ define two angles

$$\cos(\alpha) \equiv \hat{\mu} \cdot \hat{z}, \qquad \cos(\beta) \equiv \hat{\eta}_{\mathrm{OH}} \cdot \hat{z}. \tag{6.9}$$

where $\hat{z}$ denotes the unit vector in z-direction pointing into the water (see Fig. 6.3). Free energy landscapes in the $(z, \cos\alpha)$- and in the $(z, \cos\beta)$-plane are shown in the left column of the Figs. 6.4 and 6.5, taken from Ref. [2]. Near the hydrophobic surface the water molecules dipole is preferentially oriented parallel to the surface ($\cos(\alpha) \approx 0$), while one of its OH vectors either points directly towards the surface ($\cos(\beta) \approx -1$,

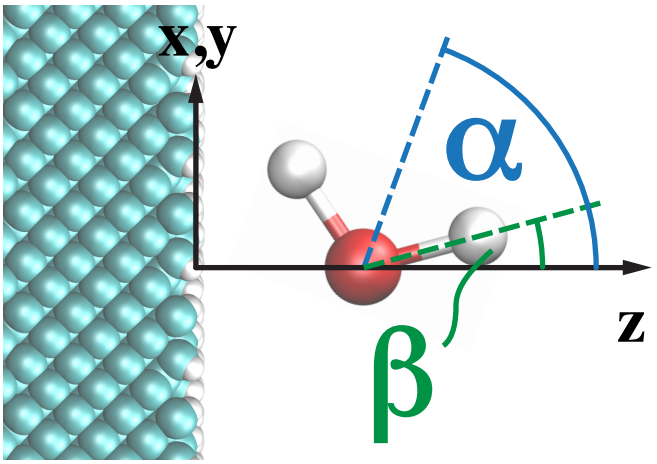

Figure 6.3.: Definition of angles α and β specifying the orientation of the water dipole vector and of the OH-bond with respect to the z-axis.

around $z \approx 0.10$ nm) or away from the surface ($\cos(\beta) \approx 1$, around $z \approx 0.16$ nm). Correspondingly, the other OH vector points either slightly away from ($\cos(\beta) \gtrsim 0$) or slightly towards ($\cos(\beta) \lesssim 0$) the surface. With such an orientation, which emulates the configuration in hexagonal ice, the water minimizes the number of broken hydrogen bonds at the surface [9, 27].

Near the hydrophilic substrates the orientational distribution is dominated by the tendency of the water molecules to form hydrogen bonds with the surface OH groups. The water molecules can either act as hydrogen bond donors and therefore point one of their OH bonds towards the surface ($\cos(\beta) \approx -0.75$), the other OH bond pointing consequently away from the surface ($\cos(\beta) \approx 1.0$), or as hydrogen bond acceptors in which case both OH bonds are oriented more or less parallel to the surface ($\cos(\beta) \approx 0.0$).

Whether however orientations towards the wall are relevant for the separation dynamics of the binding partners, can not be inferred from these free energy landscapes alone. Average first-passage times to cross a given separation z_t are therefore evaluated in the $(z, \cos\alpha)$- and the $(z, \cos\beta)$-plane; results are shown in the right columns of the Figs. 6.4 and 6.5. The water dynamics perpendicular to the hydrophobic wall is rather insensitive to the initial orientation of the water relative to the interface, while a strong dependence on the initial orientation is observed for the hydrophilic walls. Note, that the above-mentioned non-monotonicity of the MFPT curves in Fig. 6.1 is reflected in the two-dimensional MFPT landscapes, but more detail is contained in the MFPT data in the angle-distance plane. Especially on the hydrophilic surfaces, very long-lived configurational states close to the wall are discerned, which do not seem to be simply correlated with the free-energy landscape. These long-lived states are presumably related to the kinetics of hydrogen bonding to polar surface groups and possibly also collective water hydrogen-bonding effects.

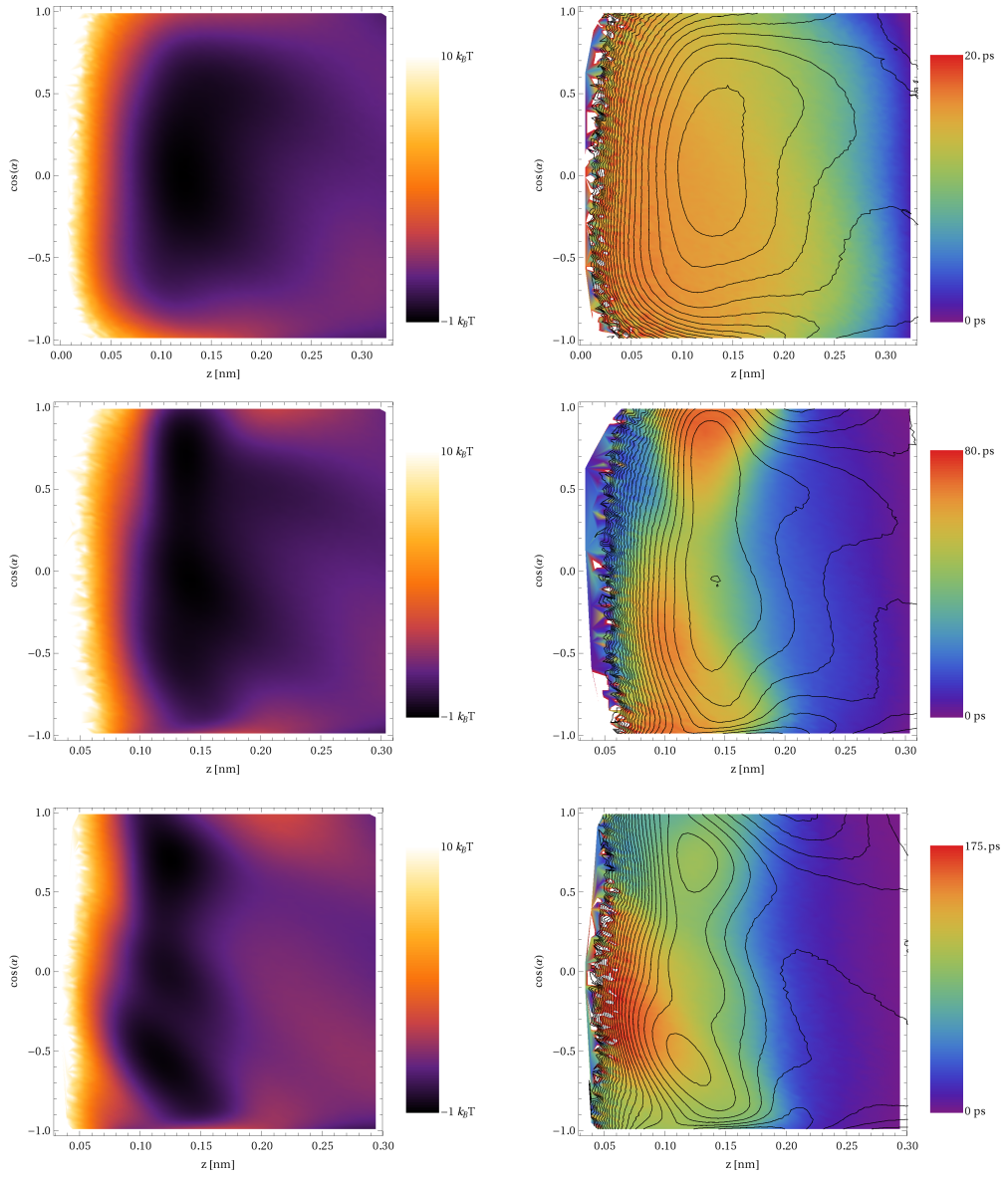

Figure 6.4.: *From top to bottom*: hydrophobic wall, hydrophilic wall (12% OH), and hydrophilic wall (25% OH). *Left column*: Free energy landscape in the $(z, \cos\alpha)$-plane for water molecules near planar interfaces. *Right column*: Average first-passage times to reach the right boundary of the plots ($z_t \approx 0.3$ nm) for water molecules starting from a distance r and an initial orientation of the water dipole moment $\cos\alpha$. *Colors* display average first-passage times, the *black lines* denote contour lines of constant free-energy (0.5 $k_B T$ per line) as shown in the *left column*.

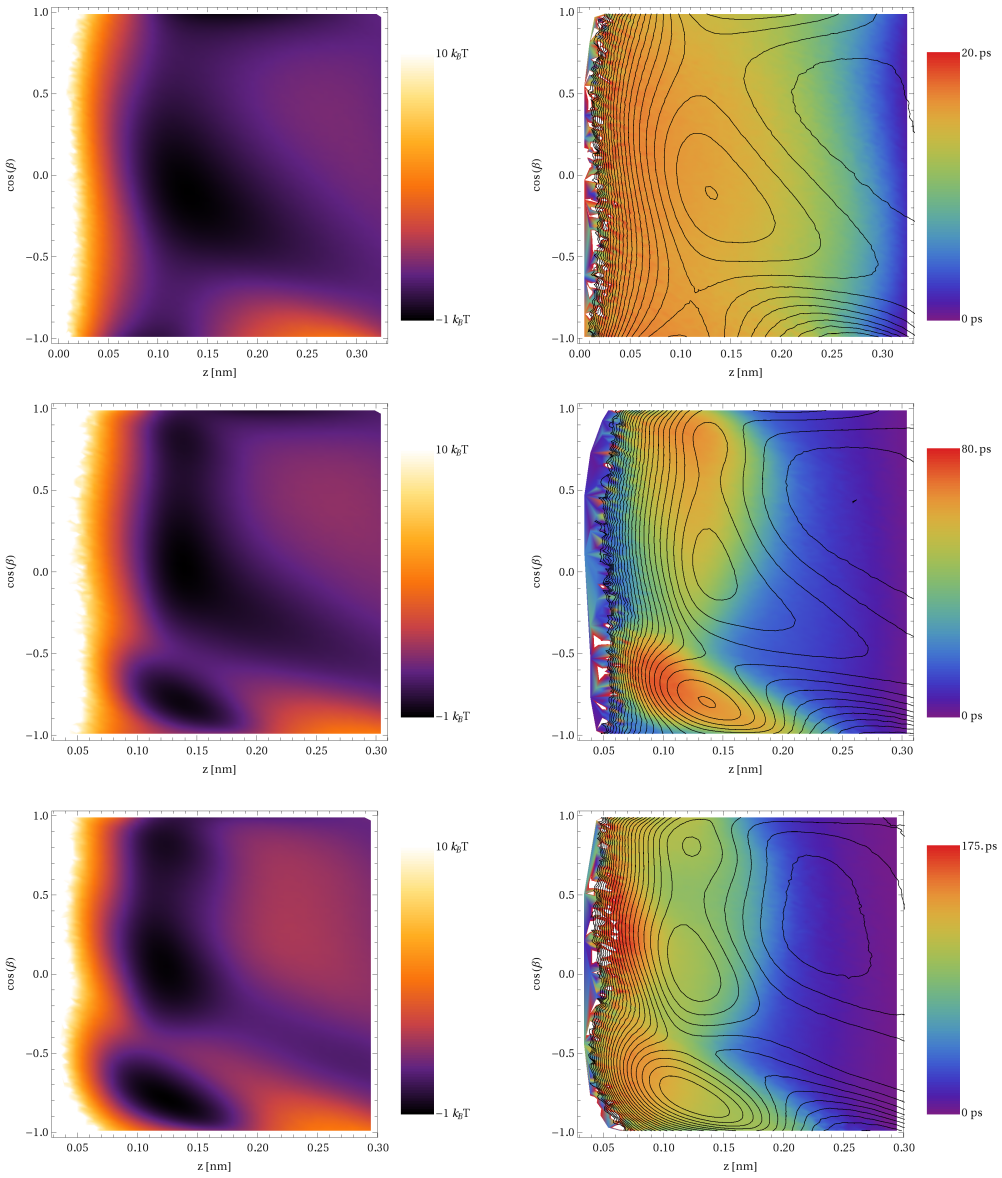

Figure 6.5.: Same as Fig. 6.4, but involving the orientation of the OH-bond $\cos\beta$ defined in Eq. 6.9 and Fig. 6.3.

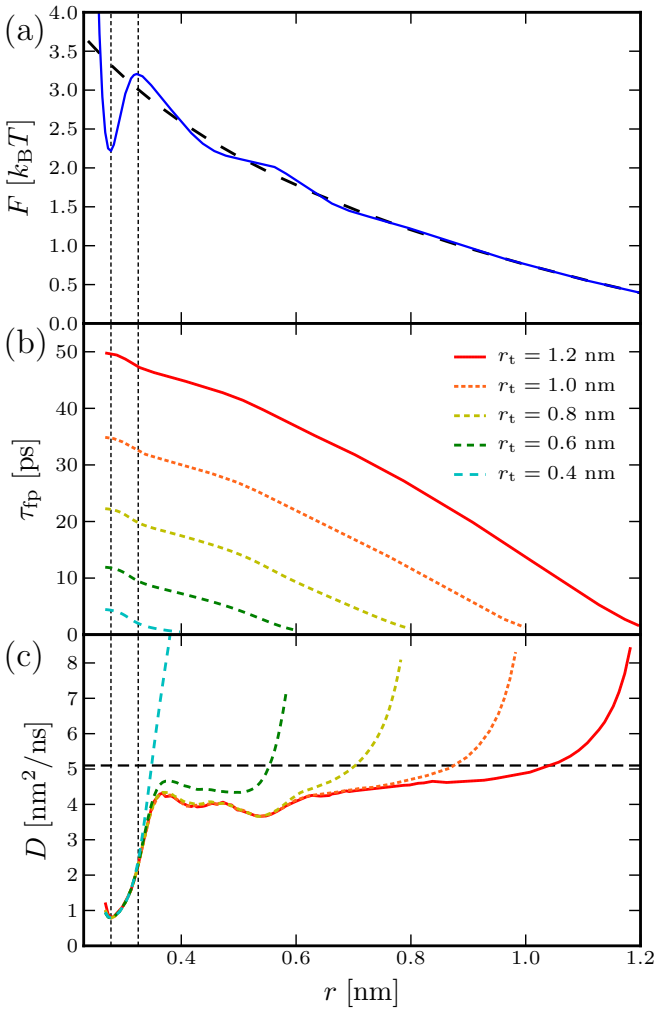

Figure 6.6.: (a) Radial free energy profile for pairs of water molecules (*solid blue line*) and ideal free energy (*broken black line*). (b) MFPT curves for water pair dynamics for several target separations r_t. (c) Relative diffusivity profiles resulting from the curves in panel b) (*same color coding*) using the MFPT method (see Eq. 6.8). The *dashed horizontal line* denotes the value of the diffusivity at large separations $2D_{\mathrm{H_2O}} \approx 5.1\ \mathrm{nm}^2/\mathrm{ns}$. *Vertical lines* indicate the positions of the first local minimum and maximum in the free energy profile.

6.4. Water dynamics near solutes

Based on MD simulation trajectories of pure SPC/E bulk water and of a single methane molecule in SPC/E bulk water, relative separation trajectories between pairs of water molecules and water methane pairs are generated. Using a spatial resolution $\Delta r = 0.005$ nm, all paths starting within a distance $\Delta r/2$ from r and crossing $r_\mathrm{t} - \Delta r/2$ for the first time a time t_fp later contribute to the MFPT $\tau_\mathrm{fp} = \left\langle t_\mathrm{fp} \right\rangle$. Due to the periodicity of the system we only consider target distances $r_\mathrm{t} < L/2$, where $L \approx 3$ nm denotes the edge length of the simulation box. The fitting range used to determine $\partial \tau_\mathrm{fp}(r, r_\mathrm{t})/\partial r$ is $\delta r = 0.06$ nm for the water pairs and $\delta r = 0.1$ nm for the water methane dynamics. For the evaluation of the integral in Eq. 6.8, the equilibrium distribution $\psi_\mathrm{eq.} = \exp\left(-\beta F\right)$ is linearly interpolated; the integral is calculated numerically

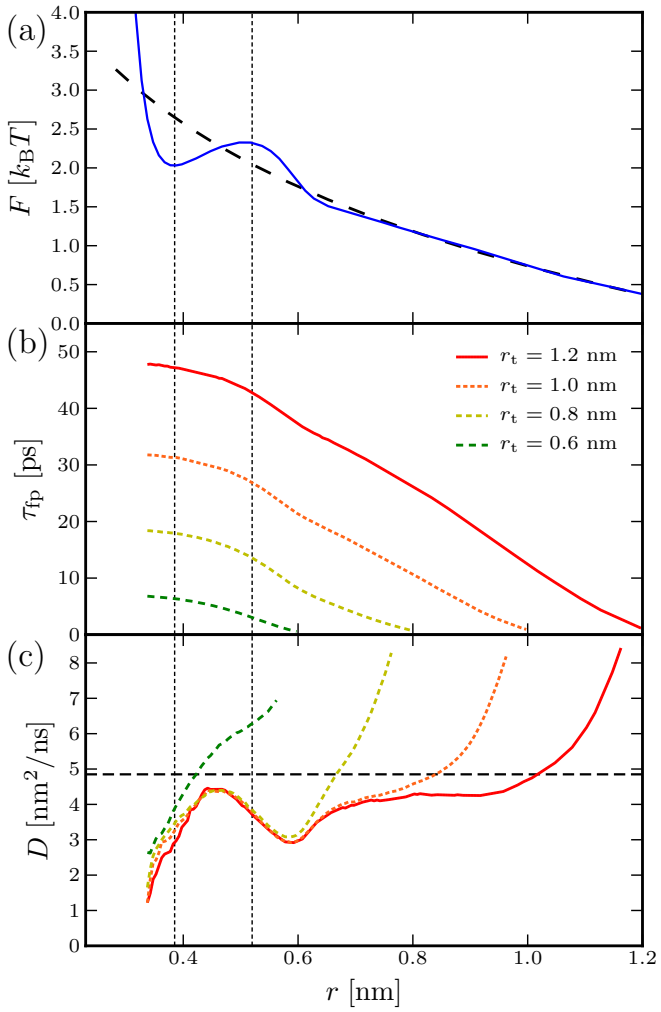

Figure 6.7.: Same as Fig. 6.6, but for water methane pair dynamics. In the limit $r \to \infty$ the relative diffusivity reaches $D_{\mathrm{H_2O}} + D_{\mathrm{CH_4}} \approx 4.85\ \mathrm{nm}^2/\mathrm{ns}$ (*dashed horizontal line* in panel c).

using reflective boundaries $r_\mathrm{min} = 0.235$ nm for water pairs and to $r_\mathrm{min} = 0.28$ nm for water methane pairs.

Free energy profiles for water-water and for water methane pairs are shown in the panels a of Figs. 6.6 and 6.7, taken from Ref. [2]: While the free energy barrier for water pairs is $\approx 1\ k_\mathrm{B}T$, water methane pairs only encounter a barrier $\lesssim 0.5\ k_\mathrm{B}T$.

MFPT curves τ_fp are shown in the central panels b of the corresponding figures. Diffusivity profiles obtained by the MFPT method (see Sec. 6.2.2) are shown in the panels c of the Figs. 6.6 and 6.7: profiles obtained from MFPT curves belonging to distinct target separations r_t mainly fall on top of each other, clearly demonstrating the validity of our approach (see Sec. 6.2). Deviations between the profiles obtained from distinct MFPT curves occur for transitions covering separations $r_\mathrm{t} - r \lesssim 0.2$ nm and taking place on time scales on the order of 1 ps: they are caused by ballistic

(non-Markovian) contributions to the dynamics which can not be captured by our overdamped description.

For large separations where molecules move independently from each other, the diffusivity profiles tend towards the values $2D_{H_2O}$ and $D_{H_2O} + D_{CH_4}$ (dashed horizontal lines in the Figs. 6.6 c and 6.7 c, where these diffusion coefficients obtained from the long time mean square displacement of single molecules are $D_{H_2O} \approx 2.55$ nm^2/ns and $D_{CH_4} \approx 2.3$ nm^2/ns.

Note that the diffusivities in the first coordination shells show pronounced differences: while the relative diffusivity for water pairs exhibits a clear drop down to $\approx$ 15 % of the values at large separations, the diffusivity profile for water methane pair dynamics is rather characterized by smooth oscillations and does not drop below $\approx$ 40%, similar to the empiric results obtained for simple two dimensional fluids [250, 251] and to the diffusivity near the hydrophobic wall. Also the diffusivity profiles of methane-water dissociation and of water at the hydrophobic wall both exhibit a very pronounced second minimum at a separation of $r \approx 0.6$ nm and $z \approx 0.4$ nm.

Note, that differences in the dissociation times between the water-water and the water-methane cases are caused both by differences in the F and D profiles. To be specific, the dissociation time for the water-water case is distinctly higher, most pronounced for the curve reaching a target separation of $r_t = 0.6$ nm. This is due to the higher free energy barrier for water-water in Fig. 6.6 a but also due to the low diffusivity below distances $r < 0.3$ nm, seen in Fig. 6.6 c. The higher diffusivity of the methane-water separation coordinate at small separation presumably is related to the absence of hydrogen bonds between methane and water. The pronounced dip in D at $r = 0.6$ nm in Fig. 6.7 c must have to do with water restructuring of the second solvation shell. Interestingly, while the methane-water diffusion is faster than water-water at small separation, it becomes slower at large separations. This explains that the MFPTs with $r_t = 1.2$ nm are rather similar for the two systems. The smaller CH_4-H_2O diffusivity at large separations is caused by the larger hydrodynamic radius of the CH_4 molecule. This behavior reflects that the diffusivity of objects is influenced both by their bare size but also by their ability to form hydrogen bonds with water.

6.5. Conclusion

Based on the Fokker-Planck description of the diffusion of individual water molecules subject to a free energy landscape and a spatially dependent diffusivity profile, we have determined diffusivity profiles at solid surfaces of varying hydrophilicity. We have also determined diffusivity profiles governing the diffusion of the distance coordinate between two water molecules and between a methane and a water molecule. The variation in the diffusivity profiles are pronounced, especially at the hydrophilic surface and for water-water diffusion. We conclude that the neglect of diffusivity profiles for predicting water kinetics in these situations can lead to gross inaccuracies. Our protocol for extracting D profiles is based on mean first passage time profiles, by

construction our approach thus gets the long-time dynamics right. We note that the same procedure can in principle be applied to experimental time series data.

In summary, there is no simple or direct relation between the free energy and diffusivity profiles, but both are needed for predicting the kinetics of single water molecules. On hydrophilic surfaces the water molecules are strongly bound, but in addition they are also slow, which presumably is due to a coupling between translational and rotational degrees of freedom. The layer where the diffusivity is reduced has a width of roughly 0.5 to 1 nm and thus matches the width over which the viscosity was found to be reduced in MD Couette shearing simulations [34].

The same difference is seen when comparing the water dynamics at a non-polar solute (methane in the present case) and a polar "solute" (taken to be a water molecule). These results point to pronounced and quite universal differences of the dynamics of individual water molecules close to hydrophobic and hydrophilic objects.

CHAPTER 7

SUMMARY AND OUTLOOK

In this work the structure and dynamics of water and the solvation of hydrophobic solutes has been studied by means of extensive molecular dynamics simulations. We have shown that molecular dynamics simulations in conjunction with current water models are capable to give an accurate description of water's properties in various situations.

In chapter 3 we have presented evidence, that the water models we use in this work can reproduce the water structure quite well. Even subtle features, such as the experimentally observed enhancement of the static structure factor at low wave vectors are not missed. We have further shown that at ambient conditions spatial correlations between order parameters describing the tetrahedral ordering of water are rather weak and decay after a few Å. That means, that no extended clusters of highly ordered water exist under these conditions [20]. It also adds to the doubts on theories that build on the idea of the propagation of structural order in water, like the structure-making/structure-breaking explanations of Hofmeister [252–254] and osmolyte [255, 256] effects. We have also seen that correlations between density and structural fluctuations are rather weak, which tells us that one has to be very careful to interpret scattering experiments, that probe density fluctuations, in terms of water order.

In chapter 4 we determined the dependence of the solvation thermodynamics of small non-polar solutes on the solute water interaction potential and its implications for the interpretation of entropy convergence. We found that for solutes with similar interactions but varying size, entropy and enthalpy convergence exists, but that the convergence temperature changes with changing interaction parameters: For increasing stiffness as well as for increasing depth of the interaction potential the convergence temperature increases, while it does not change for increasing range of the interaction. The meaning of this finding is, that there is no universality in the temperature dependence of hydrophobic solvation. As a consequence, for a set of solutes with similar interactions but differing size, which with restrictions might apply for the rare gases, as well as for homologous series of solutes, entropy convergence is expected, while for

proteins in general it is not in accordance with recent experimental findings [69]. It might be interesting to extend the study of the temperature dependence to the solvation of polar solutes, which could further clarify the denaturation thermodynamics of proteins. Unfortunately, this comes at the cost of a drastic increase in the computational effort, since the particle insertion method cannot be used efficiently any more if the solute carries partial charges.

In chapter 5 we investigated the fluctuations of a free air/water interface on the one hand and the solvation of spherical and cylindrical hydrophobic solutes on the other hand and described both phenomena based on a Helfrich type local surface free energy functional. It could be shown, that after successfully separating bulk-like and interfacial contributions, the fluctuation spectrum of the air/water interface is well described by an effective surface tension including a bending term. Using the width of the intrinsic density profile to disentangle the capillary wave contribution to the total interfacial width, we find cutoff lengths in agreement with recent experiments [229].

From the comparison of the solvation free energies of spherical and cylindrical solutes we inferred the free energy of the isochoric aggregation of spheres to form a cylinder, which is unfavourable below a threshold radius of ≈ 0.3 nm. It is further found that the solvation free energies for spheres and cylinders exhibit a maximum as a function of the inverse radius, which is equivalent with a negative Tolman length on the order of -0.1 nm at room temperature, meaning that water prefers to form droplets over cavities. From fitting the solvation free energies of spheres and cylinders simultaneously we obtain estimates for the elastic constants of the water surface, the bending rigidity beeing in qualitative agreement with the result form the air/water interface, if the latter is corrected for the effect of a finite Lennard-Jones cutoff. Although we extended the solute size to radii of 2 nm there is still a dependence of the fit parameters on the fitting range seen, which means that the asymptotic regime is not yet sufficiently reached. Increased computational capacities in the future will permit to reach even larger length scales and to yield more accurate results. Also, the extension of this study to other solute shapes might give another stringent test on the validity of the Helfrich description of the water surface. It is notable, that the cross-over length scale $R^* \approx 0.5$ nm seen in the size dependence of solvation free energies is found to be similar to the characteristic length of the intrinsic roughness of the air/water interface. It transpires, that this is the relevant length scale separating a change in the behaviour of an aqueous interface. Below that scale the discreteness of the hydrogen bonding network is dominant, while on larger scales the overall shape of the surface prevails.

Finally, in chapter 6 we applied a Fokker-Planck based formalism to the dynamics of single water molecules near hydrophobic and hydrophilic surfaces and solutes. We found a strongly varying diffusivity profile with a pronounced slow-down of the dynamics near the hydrophilic surface and near another water molecule. Near the hydrophobic surface and a methane solute the drop in the diffusivity is less pronounced. Nonetheless it should be emphasized, that in order to model the dynamics of water near a surface or solute, both the diffusivity and the free energy profile needs to be taken into account.

Chapter 8

Danksagung

An dieser Stelle möchte ich mich bei allen bedanken, die mich bei der Entstehung dieser Arbeit unterstützt haben. Besonderer Dank gebührt meinem Betreuer Herrn Prof. Roland Netz für interessante Forschungsprojekte, stete Unterstützung und nicht zuletzt die Ermöglichung vieler Konferenzbesuche und Forschungsaufenthalte in aller Welt. Insbesondere die Trips nach Boston, Istanbul und die Zeit in Santa Barbara werden mir immer in guter Erinnerung bleiben. Nie zu kurz kamen auch die vielen gemeinsamen Lehrstuhlaktivitäten: Winterschulen, Wandertage, Oktoberfestbesuche, Weihnachtsfeiern und Grillfeste. Auch dafür herzlichsten Dank.

Des weiteren bedanke ich mich bei Herrn Prof. Dominik Horinek, dafür dass er mich in die Kunst der MD Simulation eingeführt hat und dass er für alle wissenschaftlichen, technischen und sonstigen Fragen stets zur Verfügung stand.

Nicht unerwähnt bleiben darf auch unsere Sektretärin Frau Sonja Ortner, ohne die am Lehrstuhl gar nichts funktionieren würde. Für stete Hilfe und Unterstützung in allen organisatorischen Dingen ein herzliches Dankeschön.

Und schließlich möchte ich mich auch bei allen übrigen T37'lern bedanken, für die hervorragende Arbeitsathmosphäre, viele wissenschaftliche und nichtwissenschaftliche Diskussionen und auch die ein oder andere BZFlag und Kickerrunde. Besonders hervorheben möchte ich meinen Bürokollegen Herrn Aykut Erbaş. Für unzählige Diskussionen, eine schöne Zeit in Istanbul trotz Vulkanausbruchs und viel Spaß bei der täglichen Arbeit, *teşekkürler*.

Für gute und erfolgreiche Zusammenarbeit in vielen Projekten während meiner Doktorarbeit danke ich Herrn Prof. Thorsten Hugel, Herrn Prof. Lydéric Bocquet, Frau Kerstin Falk, Herrn Prof. Laurent Joly und Herrn Dr. Markus Mezger.

Bei Herrn Dr. Joseph Homolka und Herrn Dr. Stefan Recksiegel bedanke ich mich für die Zurverfügungstellung von Speicherplatz auf dem NAS System der Fakultät und für die Hilfe beim Umzug unseres Rechenclusters.

Für die großzügige Förderung im Rahmen des Graduiertenkollegs "Materials Science of Complex Interfaces" bedanke ich mich beim Elitenetzwerk Bayern und für die Rechenzeit auf dem Höchstleistungrechner HLRB-II beim Leibnitz-Rechenzentrum München.

Ganz besonders bedanken möchte ich mich bei meiner Freundin Emö und bei meiner Familie, meinen Eltern und Geschwistern. Ihre bedingungslose Unterstützung ist mir stets ein großer Rückhalt.

Chapter 9

List of Publications

This thesis is mainly based on the following articles, that have been published in or submitted to peer-reviewed journals:

F. Sedlmeier and R. R. Netz: *The Tolman length of water.* under review by Physical Review Letters, submitted August 24, 2011

F. Sedlmeier, Y. von Hansen, L. Mengyu, D. Horinek and R. R. Netz: *Water Dynamics at Interfaces and Solutes: Disentangling Free Energy and Diffusivity Contributions.* J. Stat. Phys. **145 (2)**, 240 (2011)

F. Sedlmeier, D. Horinek and R. R. Netz: *Entropy and enthalpy convergence of hydrophobic solvation beyond the hard-sphere limit.* J. Chem. Phys. **134 (5)**, 055105 (2011)

F. Sedlmeier, D. Horinek and R. R. Netz: *Spatial Correlations of Density and Structural Fluctuations in Liquid Water: A Comparative Simulation Study.* J. Am. Chem. Soc. **133 (5)**, 1391 (2011)

F. Sedlmeier, D. Horinek and R. R. Netz: *Nanoroughness, Intrinsic Density Profile, and Rigidity of the Air-Water Interface.* Phys. Rev. Lett. **103 (13)**, 136102 (2009)

Further publications, which are not directly related to this thesis:

Y. von Hansen, F. Sedlmeier, M. Hinczewski and R. R. Netz: *Friction contribution to water-bond breakage kinetics.* Phys. Rev. E **84 (5)**, 051501 (2011)

K. Falk, F. Sedlmeier, L. Joly, R. R. Netz and L. Bocquet: *Molecular Origin of Fast Water Transport in Carbon Nanotube Membranes: Superlubricity versus Curvature Dependent Friction.* Nano Lett. **10 (10)**, 4067 (2010)

M. Mezger, F. Sedlmeier, D. Horinek, H. Reichert, D. Pontoni and H. Dosch: *On the Origin of the Hydrophobic Water Gap: An X-ray Reflectivity and MD Simulation Study.* J. Am. Chem. Soc. **132 (19)**, 6735 (2010)

D. Horinek, A. Herz, L. Vrbka, F. Sedlmeier, S. Mamatkulov and R. R. Netz: *Specific ion adsorption at the air/water interface: The role of hydrophobic solvation.* Chem. Phys. Lett. **479 (4-6)**, 173 (2009)

F. Sedlmeier, J. Janecek, C. Sendner, L. Bocquet, R. R. Netz and D. Horinek: *Water at polar and nonpolar solid walls.* Biointerphases **3 (3)**, FC23-FC39 (2008)

Appendix A

Appendix - Lateral Structure Factor

In this appendix we derive the relation between the lateral structure factor, defined by (see Eq. 5.14)

$$S_{||}(\vec{q}) = \frac{1}{N_{||}} \int d^3r d^3r' f(z) f(z') e^{i\vec{q}(\vec{r_{||}} - \vec{r'_{||}})} \langle \hat{\rho}(\vec{r}) \hat{\rho}(\vec{r}') \rangle^{\mathrm{c}}, \tag{A.1}$$

and the 3D structure factor given by

$$S(\vec{Q}) = \int d^3r d^3r' e^{i\vec{Q}(\vec{r}-\vec{r}')} \langle \hat{\rho}(\vec{r}) \hat{\rho}(\vec{r}') \rangle^{\mathrm{c}}, \tag{A.2}$$

where $\vec{q} = (q_x, q_y)$ and $\vec{Q} = (Q_x, Q_y, Q_z)$ are lateral and 3D wave vectors and

$$N_{||} = \int d^3r f^2(z) \langle \hat{\rho}(\vec{r}) \rangle. \tag{A.3}$$

We also show that the power spectrum of the local GDS profile in the limit of an infinite block factor, $n \to \infty$, is proportional to the lateral structure factor with a rectangular weight function $f(z) = \theta(z_+ - z)\theta(z - z_-)$.

A.1. Equivalence of the local GDS power spectrum and the lateral structure factor

To prove the equivalence of the GDS power spectrum and the lateral structure factor, we start from the definition of the height profile using the local GDS method, given in Eq. 5.9. The number of molecules in a prism $M_{r_{||}}$ can be written in terms of the microscopic density $\hat{\rho}(\vec{r})$ as

$$\begin{aligned} M_{r_{||}} = \int_{z_-}^{z_+} dz' \int d^2 r'_{||} \theta(x' - (x - \Delta L/2)) \theta((x + \Delta L/2) - x') \\ \times \theta(y' - (y - \Delta L/2) \theta((y + \Delta L/2) - y') \hat{\rho}(\vec{r}'), \end{aligned} \tag{A.4}$$

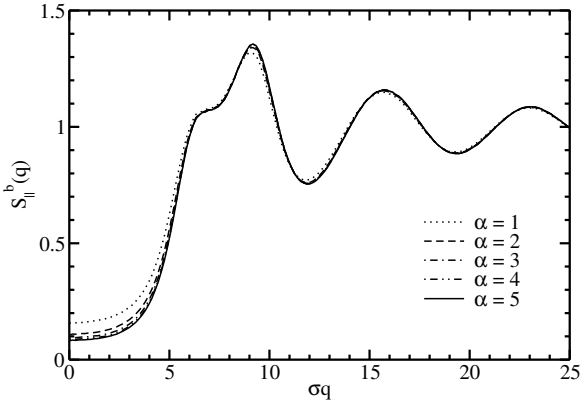

Figure A.1.: Lateral structure factor $S_{||}^b(q)$ for a weight function $f(z) = \theta(z_+ - z)\theta(z - z_-)$ and for different slab sizes $\Delta z = \alpha w$, determined from simulations. The slabs are located in the bulk region of a system of lateral size $24.0 \times 24.0\,\mathrm{nm}^2$ containing ≈ 115000 water molecules, simulated at $T = 300\,\mathrm{K}$. The wave vector q is plotted in units of the Lennard-Jones parameter $\sigma = 3.166$ Å of a SPC/E water molecule.

and the Fourier transform on the finite grid is given by

$$\tilde{h}_n(\vec{q}) = (\Delta L)^2 \sum_{\vec{r}_{||}} \tilde{h}_n(\vec{r}_{||}) e^{i\vec{q}\vec{r}_{||}}, \tag{A.5}$$

where the sum runs over all vectors $\vec{r}_{||}$ on the grid. Inserting Eqs. 5.9 and A.4 into Eq. A.5 one obtains in the limit of $n \to \infty$,

$$\tilde{h}(\vec{q}) = \frac{1}{\Delta\rho} \int d^2 r_{||} e^{i(\vec{q}\cdot\vec{r}_{||})} \int_{z_-}^{z_+} dz \hat{\rho}(\vec{r}), \tag{A.6}$$

where we have neglected the constant term. Comparison with Eq. 5.14 immediately yields

$$\langle \tilde{h}(\vec{q}) \tilde{h}(-\vec{q}) \rangle = \frac{N_{||}}{\Delta\rho^2} S_{||}(\vec{q}). \tag{A.7}$$

A.2. Relation between lateral and bulk structure factor

Next, we derive the relation between the lateral structure factor (Eq. 5.14) and the 3D structure factor (Eq. A.2). For a general weight function $f(z)$ the lateral structure factor can only be obtained from the 3D one if the system is homogeneous, because $S(\vec{Q})$ does not contain any information about the absolute position of the density distribution $\hat{\rho}(\vec{r})$ in space. Since we are interested in the lateral structure factor of the bulk

region of the simulation, we can safely assume homogeneity. In that case the correlation function depends only on the relative distance, $\langle\hat{\rho}(\vec{r})\hat{\rho}(\vec{r}')\rangle^{\mathrm{c}} = \langle\hat{\rho}(\vec{0})\hat{\rho}(\vec{r}'-\vec{r})\rangle^{\mathrm{c}}$, and we can write it as the inverse Fourier transform of the structure factor

$$\langle\hat{\rho}(\vec{0})\hat{\rho}(\vec{r}'-\vec{r})\rangle^{\mathrm{c}} = \bar{\rho}\int\frac{d^3Q}{(2\pi)^3}e^{-i\vec{Q}(\vec{r}'-\vec{r})}S(\vec{Q}), \tag{A.8}$$

where $\bar{\rho} = N/V$ is the mean density. Inserting this into Eq. 5.14 and carrying out the integration over the lateral coordinates yields

$$S_{||}(\vec{q}) = \frac{1}{L_{\mathrm{f}}}\int\frac{dQ_z}{2\pi}f(Q_z)f(-Q_z)S(\vec{q},Q_z), \tag{A.9}$$

where $f(Q_z) = \int dz e^{iQ_z z}f(z)$ is the Fourier transform of the weight function and we have defined $L_{\mathrm{f}} = \int dz f^2(z)$. We evaluate this first for the special choice of $f(z) = \theta(z_+ - z)\theta(z - z_-)$, we used in our simulations. The Fourier transform is then given by

$$f(Q_z)f(-Q_z) = \left(\frac{\sin(Q_z\Delta z/2)}{Q_z/2}\right)^2, \tag{A.10}$$

and $L_{\mathrm{f}} = \Delta z$, with $\Delta z = z_+ - z_-$. Inserting this into Eq. A.9 yields

$$S_{||}(\vec{q}) = \frac{1}{\Delta z}\int\frac{dQ_z}{2\pi}\left(\frac{\sin(Q_z\Delta z/2)}{Q_z/2}\right)^2 S(\vec{q},Q_z) \tag{A.11}$$

In the limit of an infinite slab thickness, $\Delta z \to \infty$, we have

$$\lim_{\Delta z\to\infty}\frac{2\sin^2(Q_z\Delta z/2)}{\pi\Delta z Q_z^2} = \delta(Q_z), \tag{A.12}$$

and the lateral structure factor reduces to $S_{||}(\vec{q}) = S(\vec{q},0)$ as expected. For a finite slab thickness Δz, however, the lateral structure factor differs from the three dimensional one. This is illustrated in Fig. A.1, where we plot the lateral structure factor $S_{||}^b(q)$ for slabs of different thickness $\Delta z = \alpha w$ located in the bulk region of the simulation system. Especially in the low q limit there is a pronounced dependence on the slab thickness. The corresponding compressibilities, defined by $S_{||}^{\mathrm{b}}(0) = \rho k_{\mathrm{B}}T\kappa_{\mathrm{T},||}$, are given in Tab. A.1.

Next, we evaluate Eq. A.9 for the experimentally relevant case of an exponential weight function $f(z) = \exp(-|z|/(2l))$, for $z < 0$, and $f(z) = 0$ for $z > 0$, with a penetration depth l. The Fourier transform is then found to be

$$f(Q_z)f(-Q_z) = \frac{4l^2}{1+(2lQ_z)^2}, \tag{A.13}$$

Table A.1.: Isothermal compressibility $\kappa_{T,||}$ defined by the limit of the lateral bulk structure factor $S^{b}_{||}(q)$ for $q \to 0$, $S^{b}_{||}(0) = \rho k_B T \kappa_{T,||}$, for varying slab size $\Delta z = \alpha w$. The compressibilities are derived from the data presented in Fig. A.1.

α	$\kappa_{T,||}[10^{-11}\mathrm{Pa}^{-1}]$
1	115.7
2	78.8
3	69.3
4	64.1
5	60.4
∞	45.5[1]

[1] bulk compressibility of SPC/E water at $T = 298$ K (see Tab. 3.1), in good agreement with the experimental value of $45.8 \times 10^{-11}\mathrm{Pa}^{-1}$ [257].

and $L_f = l$. With Eq. A.9 we obtain

$$S_{||}(\vec{q}) = \int \frac{dQ_z}{\pi} \frac{2l}{1+(2lQ_z)^2} S(\vec{q}, Q_z). \tag{A.14}$$

Again, in the limit of an infinite penetration depth, $l \to \infty$, we can use the relation

$$\lim_{l\to\infty} \frac{1}{\pi} \frac{2l}{1+(2lQ_z)^2} = \delta(Q_z), \tag{A.15}$$

and the lateral structure factor reduces to $S_{||}(\vec{q}) = S(\vec{q}, 0)$.

APPENDIX B

APPENDIX - ACCURACY CHECKS FOR SOLVATION FREE ENERGY CALCULATIONS

In this appendix we present several checks concerning the accuracy of the solvation free energy calculations with the thermodynamic integration method. We first show, that the employed integration procedure and the number of λ-points used is sufficient to yield accurate results. Next, we demonstrate that finite size effects are negligible and finally we investigate the dependence of the solvation free energy on the Lennard-Jones cutoff length r_c.

B.1. Integration error

We first evaluate the integration error, i. e., the error made due to the usage of a finite number of λ-values at which the derivative $\langle \partial U^{R^{\mathrm{I}} \to R^{\mathrm{II}}} / \partial \lambda \rangle$ is evaluated. For that purpose, we double the number of λ-values, corresponding to a radius increment of $\Delta R = 0.00625$ nm, for the integration step $R^{\mathrm{I}} = 1.75$ nm $\to R^{\mathrm{II}} = 2.0$ nm for the spherical solute at $T = 300$ K. Figure B.1 a shows a plot of the derivative $\langle \partial U^{R^{\mathrm{I}} \to R^{\mathrm{II}}} / \partial \lambda \rangle$ as a function of λ for the different step sizes including the interpolating function. The interpolation for the coarser resolution coincides very well with the additional data points at finer resolution. In Fig. B.1 b we plot the free energy difference obtained either by simple trapezoidal integration of $\langle \partial U^{R^{\mathrm{I}} \to R^{\mathrm{II}}}(\lambda) / \partial \lambda \rangle$ (symbols and full lines) or by using the spline interpolation (dashed lines) for both data sets. It can be seen that for the trapezoidal integration there is a systematically increasing difference between the two data sets. This difference is caused by the systematic integration error due to the concave shape of the integrand. The two curves obtained by integrating the spline interpolation lie almost perfectly on top of each other indicating that using the spline interpolation the smaller resolution of $\Delta R = 0.0125$ nm is sufficient for obtaining accurate results.

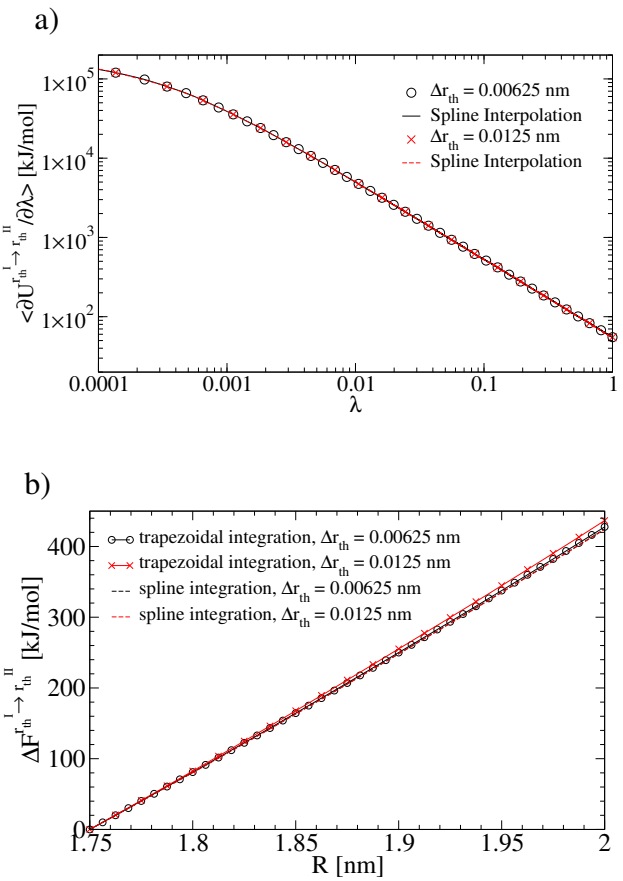

Figure B.1.: (a) Average of the derivative $\langle \partial U^{R^{\mathrm{I}} \rightarrow R^{\mathrm{II}}} / \partial \lambda \rangle$ as a function of λ for the integration step from $R^{\mathrm{I}} = 1.75\,\mathrm{nm}$ to $R^{\mathrm{I}} = 2.0\,\mathrm{nm}$ for a spherical solute at $T = 300\,\mathrm{K}$. Red squares and black circles indicate λ-values corresponding to equidistant radii with an increment of $\Delta R = 0.0125\,\mathrm{nm}$ and $\Delta R = 0.00625\,\mathrm{nm}$, respectively. The black full and red dashed lines are spline interpolations to the data sets. (b) Free energy difference with respect to the initial state $R^{\mathrm{I}} = 1.75\,\mathrm{nm}$ obtained by simple trapezoidal integration of $\langle \partial U^{R^{\mathrm{I}} \rightarrow R^{\mathrm{II}}} / \partial \lambda \rangle$ for an increment of $\Delta R = 0.0125\,\mathrm{nm}$ (red cirlces/ full line) and $\Delta R = 0.00625\,\mathrm{nm}$ (black squares / full line) and by integrating the spline interpolation of both data sets (red and black dashed lines).

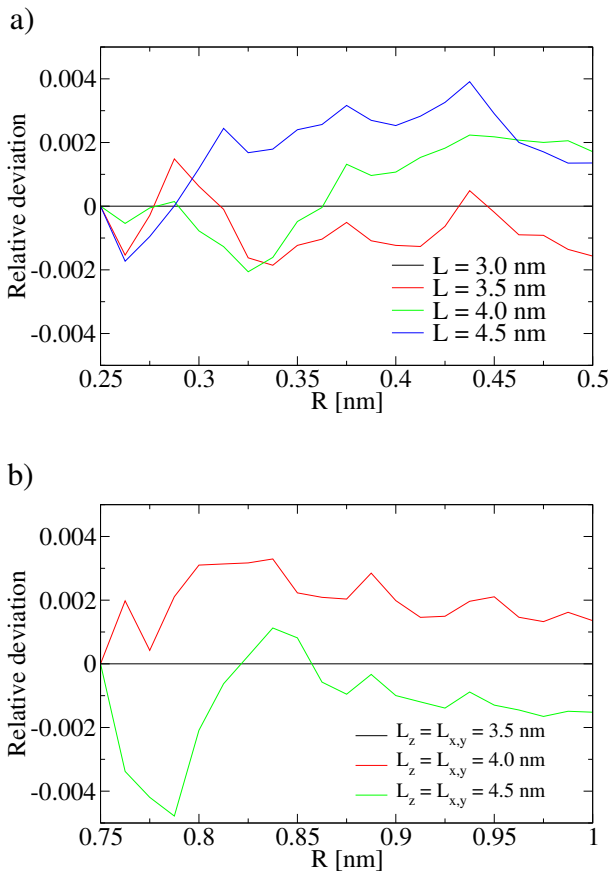

Figure B.2.: Relative differences of the free energies of solvation (a) for the integration step from $R^{\mathrm{I}} = 0.25$ nm to $R^{\mathrm{II}} = 0.5$ nm for a spherical solute for different box sizes $L = 3.0$, 3.5, 4.0 and 4.5 nm and (b) for the integration step from $R^{\mathrm{I}} = 0.75$ nm to $R^{\mathrm{II}} = 1.0$ nm for a cylindrical solute for box sizes of $L_z = L_{x,y} =$ 3.5, 4.0 and 4.5 nm. The differences are taken with respect to the smallest box. For the case of the cylinders the free energy per unit length is considered. No systematic deviation is observed with increasing box size. All simulations are done at $T = 300$ K and $p = 1$ bar.

B.2. Finite size effects

We further check the sensitivity of the free energy calculation to finite size effects by comparing the solvation free energies for the integration step from $R^{\mathrm{I}} = 0.25$ nm to $R^{\mathrm{II}} = 0.5$ nm for a spherical solute for different box sizes of $L \approx 3.0$, 3.5, 4.0 and 4.5 nm and for the integration step from $R^{\mathrm{I}} = 0.75$ nm to $R^{\mathrm{II}} = 1.0$ nm for cylindrical solutes for box sizes of $L_z \approx L_{x,y} \approx 3.5$, 4.0 and 4.5 nm. Figure B.2 shows the relative free energy differences with respect to the smallest box size in each case. No significant trend is seen with the system size and the relative deviations for all cases are quite small, which again evidences the high accuracy of the method. Since the simulations are done at fixed pressure, the box size L (spheres) and $L_{x,y}$ (cylinders) vary slightly during each simulation. The actual box sizes at the final integration step are $L^{\mathrm{II}} = 2.98$, 3.54, 4.06 and 4.54 nm for the spherical solute and $L^{\mathrm{II}}_{x,y} = 3.48$, 4.02 and 4.48 nm for the cylindrical solute, while $L_z = 3.5$, 4.0 and 4.5 nm is fixed.

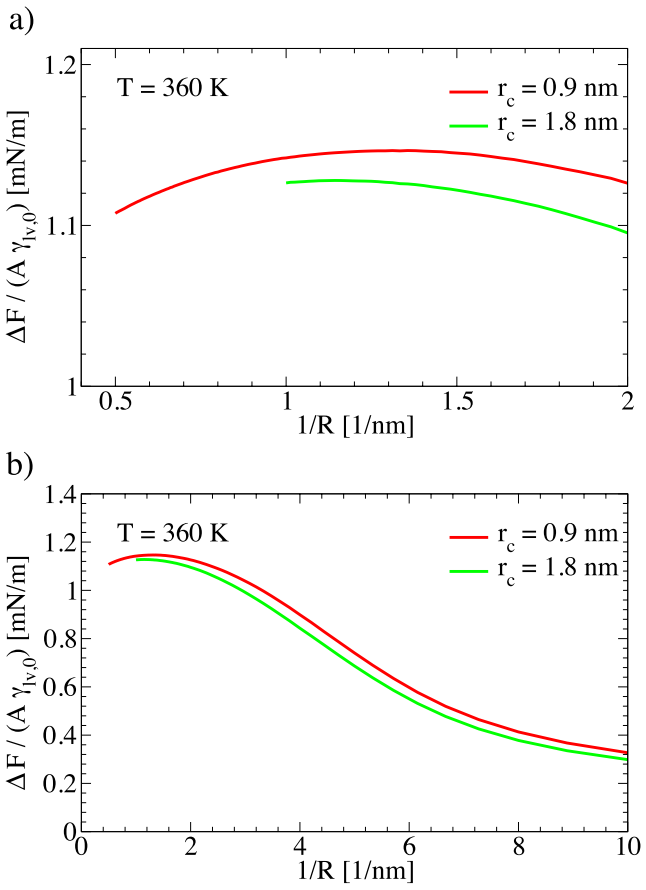

Figure B.3.: (a) Solvation free energy ΔF per area A of a cylindrical solute obtained using a cutoff radius of $r_c = 0.9$ nm (red curves) and $r_c = 1.8$ nm (green curves) for the nonbonded water water interactions as a function of the inverse radius R. The solvation free energies per area are rescaled by the planar surface tension $\gamma_{lv,0}$ of the free air/water interface obtained with the respective cutoff radii. Simulations are done at a temperature of $T = 360$ K and a pressure of $p = 1$ bar.

B.3. Cutoff effects

Finally, we discuss the dependence of the solvation free energy on the cutoff length of the Lennard-Jones interactions, which is set to $r_c = 0.9$ nm in most of our simulations. Since we only study solutes up to a radius of 2.0 nm, which is on the same order as r_c, no strong influence of the finite cutoff length would be expected. We check this explicitly by determining the solvation free energy of a cylindrical solute at $T = 360$ K using a Lennard-Jones cutoff length of $r_c = 1.8$ nm. In Fig. B.3 we show the solvation free energies for both cutoff lengths rescaled by the planar air/water surface tension, which is $\gamma_{lv,0} = 50.9$ mN/m for $r_c = 1.8$ nm and $\gamma_{lv,0} = 45.5$ mN/m for $r_c = 0.9$ nm. The slight shift, that is seen in Fig. B.3, can be attributed to the statistical uncertainty of the planar surface tension, which is on the order of 2%. Apart from this small deviation the shape of both curves is very similar, which in particular means that the Tolman length extracted from the data does not depend significantly on the Lennard Jones cutoff length.

BIBLIOGRAPHY

[1] Y. von Hansen, F. Sedlmeier, M. Hinczewski, et al. Friction contribution to water-bond breakage kinetics. Phys. Rev. E **84 (5)**, 051501 (2011)

[2] F. Sedlmeier, Y. von Hansen, L. Mengyu, et al. Water Dynamics at Interfaces and Solutes: Disentangling Free Energy and Diffusivity Contributions. J. Stat. Phys. **145 (2)**, 240 (2011)

[3] F. Sedlmeier, D. Horinek, R. R. Netz. Entropy and enthalpy convergence of hydrophobic solvation beyond the hard-sphere limit. J. Chem. Phys. **134 (5)**, 055105 (2011)

[4] F. Sedlmeier, D. Horinek, R. R. Netz. Spatial Correlations of Density and Structural Fluctuations in Liquid Water: A Comparative Simulation Study. J. Am. Chem. Soc. **133 (5)**, 1391 (2011)

[5] K. Falk, F. Sedlmeier, L. Joly, et al. Molecular Origin of Fast Water Transport in Carbon Nanotube Membranes: Superlubricity versus Curvature Dependent Friction. Nano Lett. **10 (10)**, 4067 (2010)

[6] M. Mezger, F. Sedlmeier, D. Horinek, et al. On the Origin of the Hydrophobic Water Gap: An X-ray Reflectivity and MD Simulation Study. J. Am. Chem. Soc. **132 (19)**, 6735 (2010)

[7] F. Sedlmeier, D. Horinek, R. R. Netz. Nanoroughness, Intrinsic Density Profile, and Rigidity of the Air-Water Interface. Phys. Rev. Lett. **103 (13)**, 136102 (2009)

[8] D. Horinek, A. Herz, L. Vrbka, et al. Specific ion adsorption at the air/water interface: The role of hydrophobic solvation. Chem. Phys. Lett. **479 (4-6)**, 173 (2009)

[9] F. Sedlmeier, J. Janecek, C. Sendner, et al. Water at polar and nonpolar solid walls. Biointerphases **3 (3)**, FC23 (2008)

[10] F. Franks. *Water: a matrix of life*. 2nd edition (Royal Society of Chemistry, Cambridge, 2000)

[11] P. Ball. *Life's matrix: a biography of water*. 1st edition (University of California Press, Berkeley, 2001)

[12] S. Jackson. *Anatomy & Physiology for Nurses. Nurses' Aids Series*. 9th edition (Bailliere Tindall, London, 1985)

[13] P. Ball. Water as an Active Constituent in Cell Biology. Chem. Rev. **107 (1)**, 74 (2008)

[14] G. S. Kell. Density, thermal expansivity, and compressibility of liquid water from 0° to 150°: Correlations and tables for atmospheric pressure and saturation reviewed and expressed on 1968 temperature scale. J. Chem. Eng. Data **20 (1)**, 97 (1975)

[15] F. Franks. *Water. A Comprehensive Treatise.* 1st edition (Ed. Plenum, New York, 1973)

[16] F. Stillinger. Water revisited. Science **209 (4455)**, 451 (1980)

[17] A. K. Soper, M. G. Phillips. A new determination of the structure of water at 25° C. Chem. Phys. **107 (1)**, 47 (1986)

[18] T. Head-Gordon, G. Hura. Water Structure from Scattering Experiments and Simulation. Chem. Rev. **102 (8)**, 2651 (2002)

[19] R. Kumar, J. R. Schmidt, J. L. Skinner. Hydrogen bonding definitions and dynamics in liquid water. J. Chem. Phys. **126 (20)**, 204107 (2007)

[20] C. Huang, K. T. Wikfeldt, T. Tokushima, et al. The inhomogeneous structure of water at ambient conditions. Proc. Natl. Acad. Sci. U.S.A. **106 (36)**, 15214 (2009)

[21] O. Mishima, H. E. Stanley. The relationship between liquid, supercooled and glassy water. Nature **396 (6709)**, 329 (1998)

[22] A. K. Soper, J. Teixeira, T. Head-Gordon. Is ambient water inhomogeneous on the nanometer-length scale? Proc. Natl. Acad. Sci. U.S.A. **107 (12)**, E44 (2010)

[23] G. N. I. Clark, G. Hura, J. Teixeira, et al. Small-angle scattering and the structure of ambient liquid water. Proc. Natl. Acad. Sci. U.S.A. **107 (32)**, 14003 (2010)

[24] P. G. de Gennes, F. Brochard-Wyart. *Capillarity and wetting phenomena: drops, bubbles, pearls, waves*. 1st edition (Springer Science+Business Media, Inc., New York, 2004)

[25] X. Li, J. Li, M. Eleftheriou, et al. Hydration and dewetting near fluorinated superhydrophobic plates. J. Am. Chem. Soc **128 (38)**, 12439 (2006)

[26] J. Janecek, R. R. Netz. Interfacial Water at Hydrophobic and Hydrophilic Surfaces: Depletion versus Adsorption. Langmuir **23 (16)**, 8417 (2007)

[27] C. Y. Lee, J. A. McCammon, P. J. Rossky. The structure of liquid water at an extended hydrophobic surface. J. Chem. Phys. **80 (9)**, 4448 (1984)

[28] D. A. Doshi, E. B. Watkins, J. N. Israelachvili, et al. Reduced water density at hydrophobic surfaces: Effect of dissolved gases. Proc. Natl. Acad. Sci. U.S.A. **102 (27)**, 9458 (2005)

[29] M. Maccarini, R. Steitz, M. Himmelhaus, et al. Density depletion at solid-liquid interfaces: A neutron reflectivity study. Langmuir **23 (2)**, 598 (2007)

[30] R. Steitz, T. Gutberlet, T. Hauss, et al. Nanobubbles and Their Precursor Layer at the Interface of Water Against a Hydrophobic Substrate. Langmuir **19 (6)**, 2409 (2003)

[31] D. Schwendel, T. Hayashi, R. Dahint, et al. Interaction of Water with Self-Assembled Monolayers: Neutron Reflectivity Measurements of the Water Density in the Interface Region. Langmuir **19 (6)**, 2284 (2003)

[32] M. Mezger, H. Reichert, S. Schöder, et al. High-resolution in situ x-ray study of the hydrophobic gap at the water-octadecyl-trichlorosilane interface. Proc. Natl. Acad. Sci. U.S.A. **103 (49)**, 18401 (2006)

[33] D. M. Huang, C. Sendner, D. Horinek, et al. Water Slippage versus Contact Angle: A Quasiuniversal Relationship. Phys. Rev. Lett. **101 (22)**, 226101 (2008)

[34] C. Sendner, D. Horinek, L. Bocquet, et al. Interfacial Water at Hydrophobic and Hydrophilic Surfaces: Slip, Viscosity, and Diffusion. Langmuir **25 (18)**, 10768 (2009)

[35] S. Leikin, V. Parsegian, D. Rau, et al. Hydration forces. Annu. Rev. Phys. Chem. **44 (1)**, 369 (1993)

[36] R. Rand, V. Parsegian. Hydration forces between phospholipid bilayers. Biochim. Biophys. Acta **988 (3)**, 351 (1989)

[37] D. Leneveu, R. Rand, V. Parsegian. Measurement of forces between lecithin bilayers. Nature **259 (5544)**, 601 (1976)

[38] J. N. Israelachvili, R. Pashley. The hydrophobic interaction is long-range, decaying exponentially with distance. Nature **300 (5890)**, 341 (1982)

[39] R. Pashley, J. N. Israelachvili. A comparison of surface forces and interfacial properties of mica in purified surfactant solutions. Colloid Surface **2 (2)**, 169 (1981)

[40] K. Lum, D. Chandler, J. D. Weeks. Hydrophobicity at small and large length scales. J. Phys. Chem. B **103 (22)**, 4570 (1999)

[41] D. Chandler. Interfaces and the driving force of hydrophobic assembly. Nature **437 (7059)**, 640 (2005)

[42] D. M. Huang, P. L. Geissler, D. Chandler. Scaling of hydrophobic solvation free energies. J. Phys. Chem. B **105 (28)**, 6704 (2001)

[43] H. S. Ashbaugh, L. R. Pratt. Colloquium: Scaled particle theory and the length scales of hydrophobicity. Rev. Mod. Phys. **78 (1)**, 159 (2006)

[44] H. S. Ashbaugh. Entropy crossover from molecular to macroscopic cavity hydration. Chem. Phys. Lett. **477 (1-3)**, 109 (2009)

[45] W. Blokzijl, J. B. F. N. Engberts. Hydrophibic effects - opinion and facts. Angew. Chem. Int. Ed. **32 (11)**, 1545 (1993)

[46] K. Dill. The meaning of hydrophobicity. Science **250 (4978)**, 297 (1990)

[47] E. Wilhelm, R. Battino, R. Wilcock. Low-pressure solubility of gases in liquid water. Chem. Rev. **77 (2)**, 219 (1977)

[48] S. Dec, S. J. Gill. Enthalpies of aqueous solutions of noble gases at 25° C. J. Solution Chem. **14 (6)**, 417 (1985)

[49] G. Olofson, A. Oshodj, E. Qvarnström, et al. Calorimetric measurements on slightly soluble gases in water. Enthalpies of solution of helium, neon, argon, krypton, xenon, methane, ethane, propane, n-butane, and oxygen at 288.15, 298.15, and 308.15 K. J. Chem. Thermodyn. **16 (11)**, 1041 (1984)

[50] F. Diederich. Complexation of neutral molecules by cyclophane hosts. Angew. Chem. Int. Ed. **27 (3)**, 362 (1988)

[51] H. Schneider. Mechanisms of molecular recognition: investigations of organic host–guest complexes. Angew. Chem. Int. Ed. **30 (11)**, 1417 (1991)

[52] C. Tanford. *The Hydrophobic Effect: Formation of Micelles and Biological Membranes*. 1st edition (Wiley-Interscience, New York, 1973)

[53] K. A. Dill. Dominant forces in protein folding. Biochemistry **29 (31)**, 7133 (1990)

[54] F. Chiti, C. M. Dobson. Amyloid formation by globular proteins under native conditions. Nat. Chem. Biol. **5 (1)**, 15 (2009)

[55] G. Reddy, J. Straub, D. Thirumalai. Dry amyloid fibril assembly in a yeast prion peptide is mediated by long-lived structures containing water wires. Proc. Natl. Acad. Sci. U.S.A. **107 (50)**, 21459 (2010)

[56] W. Kauzmann. Some factors in the interpretation of protein denaturation. Adv. Protein Chem. **14**, 1 (1959)

[57] H. Frank, M. Evans. Free volume and entropy in condensed systems III. Entropy in binary liquid mixtures; partial molal entropy in dilute solutions; structure and thermodynamics in aqueous electrolytes. J. Chem. Phys. **13**, 507 (1945)

[58] E. Sloan. *Clathrate Hydrates of Natural Gases*. 2nd edition (Marcel Dekker, New York, 1998)

[59] F. H. Stillinger. *Water in Polymers*. 1st edition (ACS Symposium Series, Washington DC, 1980)

[60] N. Southall, K. A. Dill, A. D. J. Haymet. A view of the hydrophobic effect. J. Phys. Chem. B **106 (3)**, 521 (2002)

[61] R. L. Baldwin. Temperature dependence of the hydrophobic interaction in protein folding. Proc. Natl. Acad. Sci. U.S.A. **83 (21)**, 8069 (1986)

[62] K. P. Murphy, S. J. Gill. Group additivity thermodynamics for dissolution of solid cyclic dipeptides. Thermochim. Acta **172**, 11 (1990)

[63] K. P. Murphy, S. J. Gill. Solid model compounds and the thermodynamics of protein unfolding. J. Mol. Biol. **222 (3)**, 699 (1991)

[64] P. L. Privalov, N. N. Khechinashvili. Thermodynamic approach to the problem of stabilization of globular protein structure: A calorimetric study. J. Mol. Biol. **86 (3)**, 665 (1974)

[65] P. L. Privalov. Stability of Proteins - Small Globular Proteins. Adv. Protein Chem. **33**, 167 (1979)

[66] P. L. Privalov, S. J. Gill. Stability of protein structure and hydrophobic interaction. Adv. Protein Chem. **39**, 191 (1988)

[67] K. P. Murphy, P. L. Privalov, S. J. Gill. Common features of protein unfolding and dissolution of hydrophobic compounds. Science **247 (4942)**, 559 (1990)

[68] B. Lee. Isoenthalpic and isoentropic temperatures and the thermodynamics of protein denaturation. Proc. Natl. Acad. Sci. U.S.A. **88 (12)**, 5154 (1991)

[69] A. D. Robertson, K. P. Murphy. Protein structure and the energetics of protein stability. Chem. Rev. **97 (5)**, 1251 (1997)

[70] D. Chandler. Two faces of water. Nature **417 (6888)**, 491 (2002)

[71] S. Garde, A. E. Garcia, L. R. Pratt, et al. Temperature dependence of the solubility of non-polar gases in water. Biophys. Chem. **78 (1-2)**, 21 (1999)

[72] S. Garde, G. Hummer, A. E. Garcia, et al. Origin of entropy convergence in hydrophobic hydration and protein folding. Phys. Rev. Lett. **77 (24)**, 4966 (1996)

[73] G. Hummer, S. Garde, A. E. Garcia, et al. Hydrophobic effects on a molecular scale. J. Phys. Chem. B **102 (51)**, 10469 (1998)

[74] G. Hummer, S. Garde, A. E. Garcia, et al. An information theory model of hydrophobic interactions. Proc. Natl. Acad. Sci. U.S.A. **93 (17)**, 8951 (1996)

[75] G. Hummer, S. Garde, A. E. Garcia, et al. New perspectives on hydrophobic effects. Chem. Phys. **258 (2-3)**, 349 (2000)

[76] G. Hummer, S. Garde. Cavity expulsion and weak dewetting of hydrophobic solutes in water. Phys. Rev. Lett. **80 (19)**, 4193 (1998)

[77] W. Still, A. Tempczyk, R. Hawley, et al. Semianalytical treatment of solvation for molecular mechanics and dynamics. J. Am. Chem. Soc. **112 (16)**, 6127 (1990)

[78] C. Tanford. Interfacial free energy and the hydrophobic effect. Proc. Natl. Acad. Sci. U.S.A. **76 (9)**, 4175 (1979)

[79] R. C. Tolman. The Effect of Droplet Size on Surface Tension. J. Chem. Phys. **17 (3)**, 333 (1949)

[80] H. S. Ashbaugh. Blowing bubbles in Lennard-Jonesium along the saturation curve. J. Chem. Phys. **130 (20)**, 204517 (2009)

[81] A. van Giessen, E. Blokhuis. Direct determination of the Tolman length from the bulk pressures of liquid drops via molecular dynamics simulations. J. Chem. Phys. **131 (16)**, 164705 (2009)

[82] F. H. Stillinger. Structure in Aqueous Solutions of Nonpolar Solutes from the Standpoint of Scaled-Particle Theory. J. Solution Chem. **2 (2-3)**, 141 (1973)

[83] F. Floris. Modeling the cavitation free energy. J. Phys. Chem. B **109 (50)**, 24061 (2005)

[84] F. Floris, M. Selmi, A. Tani, et al. Free energy and entropy for inserting cavities in water: Comparison of Monte Carlo simulation and scaled particle theory results. J. Chem. Phys. **107**, 6353 (1997)

[85] H. S. Ashbaugh, M. E. Paulaitis. Effect of solute size and solute-water attractive interactions on hydration water structure around hydrophobic solutes. J. Am. Chem. Soc. **123 (43)**, 10721 (2001)

[86] A. Wallqvist, B. Berne. Molecular dynamics study of the dependence of water solvation free energy on solute curvature and surface area. J. Phys. Chem. **99 (9)**, 2885 (1995)

[87] F. Grigoriev, M. Basilevsky, S. Gabin, et al. Cavitation free energy for organic molecules having various sizes and shapes. J. Phys. Chem. B **111 (49)**, 13748 (2007)

[88] C. Fennell, C. Kehoe, K. Dill. Oil/Water Transfer Is Partly Driven by Molecular Shape, Not Just Size. J. Am. Chem. Soc. **132 (1)**, 234 (2009)

[89] W. Helfrich. Elastic properties of lipid bilayers - theory and possible experiments. Z. Naturforsch., C: Biosci. **28 (11-1)**, 693 (1973)

[90] E. M. Blokhuis, J. Groenewold, D. H. Bedeaux. Fluctuation route to the bending rigidity. Mol. Phys. **96 (3)**, 397 (1999)

[91] K. R. Mecke, S. Dietrich. Effective Hamiltonian for liquid-vapor interfaces. Phys. Rev. E **59 (6)**, 6766 (1999)

[92] E. Chacón, P. Tarazona. Characterization of the intrinsic density profiles for liquid surfaces. J. Phys. Condens. Matter **17 (45)**, S3493 (2005)

[93] J. Stecki. Extended capillary wave theory and the ellipsometric coefficient. J. Chem. Phys. **109 (12)**, 5002 (1998)

[94] J. Stecki. An effective Hamiltonian for correlations in interfaces. J. Chem. Phys. **114 (17)**, 7574 (2001)

[95] C. Fradin, A. Braslau, D. Luzet, et al. Reduction in the surface energy of liquid interfaces at short length scales. Nature **403 (6772)**, 871 (2000)

[96] D. X. Li, B. Yang, B. H. Lin, et al. Wavelength dependence of liquid-vapor interfacial tension of Ga. Phys. Rev. Lett. **92 (13)**, 136102 (2004)

[97] D. Vaknin, W. Bu, A. Travesset. Extracting the pair distribution function of liquids and liquid-vapor surfaces by grazing incidence x-ray diffraction mode. J. Chem. Phys. **129 (4)**, 044504 (2008)

[98] P. Tarazona, R. Checa, E. Chacón. Critical analysis of the density functional theory prediction of enhanced capillary waves. Phys. Rev. Lett. **99 (19)**, 196101 (2007)

[99] E. M. Blokhuis, J. Kuipers, R. L. C. Vink. Description of the fluctuating colloid-polymer interface. Phys. Rev. Lett. **101 (8)**, 086101 (2008)

[100] M. Paulus, C. Gutt, M. Tolan. Static structure factor of capillary waves at large momentum transfer. Phys. Rev. B **78 (23)**, 235419 (2008)

[101] Y. Rhee, E. Sorin, G. Jayachandran, et al. Simulations of the role of water in the protein-folding mechanism. Proc. Natl. Acad. Sci. U.S.A. **101 (17)**, 6456 (2004)

[102] P. Fenimore, H. Frauenfelder, B. McMahon, et al. Slaving: solvent fluctuations dominate protein dynamics and functions. Proc. Natl. Acad. Sci. U.S.A. **99 (25)**, 16047 (2002)

[103] P. Geissler, C. Dellago, D. Chandler. Kinetic pathways of ion pair dissociation in water. J. Phys. Chem. B **103 (18)**, 3706 (1999)

[104] B. de Groot, H. Grubmuller. Water permeation across biological membranes: Mechanism and dynamics of aquaporin-1 and GlpF. Science **294 (5550)**, 2353 (2001)

[105] L. Bocquet, J.-L. Barrat. Flow boundary conditions from nano- to micro-scales. Soft Matter **3 (6)**, 685 (2007)

[106] P. Thompson, M. Robbins. Shear flow near solids: Epitaxial order and flow boundary conditions. Phys. Rev. A **41 (12)**, 6830 (1990)

[107] H. Stone, A. Stroock, A. Ajdari. Engineering flows in small devices: Microfluidics toward a lab-on-a-chip. Annu. Rev. Fluid. Mech. **36**, 381 (2004)

[108] F. Csajka, D. Chandler. Transition pathways in a many-body system: Application to hydrogen-bond breaking in water. J. Chem. Phys. **109 (3)**, 1125 (1998)

[109] D. Laage, J. T. Hynes. On the molecular mechanism of water reorientation. J. Phys. Chem. B **112 (45)**, 14230 (2008)

[110] D. Laage, J. T. Hynes. A molecular jump mechanism of water reorientation. Science **311 (5762)**, 832 (2006)

[111] D. Zichi, P. J. Rossky. Solvent molecular dynamics in regions of hydrophobic hydration. J. Chem. Phys. **84 (5)**, 2814 (1986)

[112] F. Sciortino, P. Poole, H. Stanley, et al. Lifetime of the bond network and gel-like anomalies in supercooled water. Phys. Rev. Lett. **64 (14)**, 1686 (1990)

[113] A. Luzar, D. Chandler. Hydrogen-bond kinetics in liquid water. Nature **379 (6560)**, 55 (1996)

[114] M. O. Jensen, O. G. Mouritsen, G. H. Peters. The hydrophobic effect: Molecular dynamics simulations of water confined between extended hydrophobic and hydrophilic surfaces. J. Chem. Phys. **120 (20)**, 9729 (2004)

[115] S. Han, P. Kumar, H. E. Stanley. Absence of a diffusion anomaly of water in the direction perpendicular to hydrophobic nanoconfining walls. Phys. Rev. E **77 (3)**, 030201 (2008)

[116] S. R.-V. Castrillon, N. Giovambattista, I. A. Aksay, et al. Evolution from Surface-Influenced to Bulk-Like Dynamics in Nanoscopically Confined Water. J. Phys. Chem. B **113 (23)**, 7973 (2009)

[117] M. Odelius, M. Bernasconi, M. Parrinello. Two dimensional ice adsorbed on mica surface. Phys. Rev. Lett. **78 (14)**, 2855 (1997)

[118] W. Cantrell, G. Ewing. Thin film water on muscovite mica. J. Phys. Chem. B **105 (23)**, 5434 (2001)

[119] T.-D. Li, J. Gao, R. Szoszkiewicz, et al. Structured and viscous water in subnanometer gaps. Phys. Rev. B: Condens. Matter **75 (11)**, 115415 (2007)

[120] T.-D. Li, E. Riedo. Nonlinear Viscoelastic Dynamics of Nanoconfined Wetting Liquids. Phys. Rev. Lett. **100 (10)**, 106102 (2008)

[121] R. Zangi, A. Mark. Monolayer ice. Phys. Rev. Lett. **91 (2)**, 025502 (2003)

[122] J. Mittal, T. M. Truskett, J. R. Errington, et al. Layering and position-dependent diffusive dynamics of confined fluids. Phys. Rev. Lett. **100 (14)**, 145901 (2008)

[123] L. Bosio, J. Teixeira, M.-C. Bellissent-Funel. Enhanced density fluctuations in water analyzed by neutron scattering. Phys. Rev. A **39 (12)**, 6612 (1989)

[124] Y. Xie, K. F. L. Jr, G. Morales, et al. Noncritical behavior of density fluctuations in supercooled water. Phys. Rev. Lett. **71 (13)**, 2050 (1993)

[125] J. R. Errington, P. G. Debenedetti. Relationship between structural order and the anomalies of liquid water. Nature **409 (6818)**, 318 (2001)

[126] D. Frenkel, B. Smit. *Understanding Molecular Simulation*. 2nd edition (Academic Press, Amsterdam, 2002)

[127] M. P. Allen, D. J. Tildesley. *Computer Simulation of Liquids*. 1st edition (Oxford University Press, Oxford, 1987)

[128] R. Gillilan, K. Wilson. Shadowing, rare events, and rubber bands. A variational Verlet algorithm for molecular dynamics. J. Chem. Phys. **97**, 1757 (1992)

[129] D. G. Quinlan, S. Tremaine. On the reliability of gravitational N-body integrations. Mon. Not. R. Astron. Soc. **259**, 505 (1992)

[130] D. Marx, J. Hutter. *In Modern methods and algorithms of quantum chemistry*. 1st edition (NIC Series, Jülich, 2000)

[131] R. Car, M. Parrinello. Unified approach for molecular dynamics and density-functional theory. Phys. Rev. Lett. **55 (22)**, 2471 (1985)

[132] B. Hess, C. Kutzner, D. van der Spoel, et al. GROMACS 4: Algorithms for highly efficient, load-balanced, and scalable molecular simulation. J. Chem. Theory Comput. **4 (3)**, 435 (2008)

[133] D. van der Spoel, E. Lindahl, B. Hess, et al. GROMACS: Fast, flexible, and free. J. Comput. Chem. **26 (16)**, 1701 (2005)

[134] H. J. C. Berendsen, J. Postma, W. F. van Gunsteren, et al. Molecular dynamics with coupling to an external bath. J. Chem. Phys. **81 (8)**, 3684 (1984)

[135] D. Bonthuis, K. Falk, C. Kaplan, et al. Comment on "Pumping of Confined Water in Carbon Nanotubes by Rotation-Translation Coupling". Phys. Rev. Lett. **105 (20)**, 209401 (2010)

[136] U. Essmann, L. Perera, M. L. Berkowitz, et al. A smooth particle mesh ewald method. J. Chem. Phys. **103 (19)**, 8577 (1995)

[137] T. Darden, D. York, L. Pedersen. Particle mesh ewald - an N log(N) method for ewald sums in large systems. J. Chem. Phys. **98 (12)**, 10089 (1993)

[138] B. Hess, H. Bekker, H. J. C. Berendsen, et al. LINCS: A linear constraint solver for molecular simulations. J. Comput. Chem. **18 (12)**, 1463 (1997)

[139] S. Miyamoto, P. A. Kollmann. SETTLE: An analytical version of the SHAKE and RATTLE algorithm for rigid water molecules. J. Comput. Chem. **13 (8)**, 952 (1992)

[140] J. A. Barker, R. O. Watts. Structure of water; A Monte Carlo calculation. Chem. Phys. Lett. **3 (3)**, 144 (1969)

[141] A. Rahman, F. H. Stillinger. Molecular dynamics study of liquid water. J. Chem. Phys. **55 (7)**, 3336 (1971)

[142] B. Guillot. A reappraisal of what we have learnt during three decades of computer simulations on water. J. Mol. Liq. **101 (1-3)**, 219 (2002)

[143] W. L. Jorgensen, J. Tirado-Rives. Potential energy functions for atomic-level simulations of water and organic and biomolecular systems. Proc. Natl. Acad. Sci. U.S.A. **102 (19)**, 6665 (2005)

[144] J. Gregory, D. Clary, K. Liu, et al. The water dipole moment in water clusters. Science **275 (5301)**, 814 (1997)

[145] H. J. C. Berendsen, J. Postma, W. F. van Gunsteren, et al. *in Intermolecular Forces* (Reidel, Dordrecht, 1981)

[146] H. J. C. Berendsen, J. R. Grigera, T. P. Straatsma. The missing term in effective pair potentials. J. Phys. Chem. **91 (24)**, 6269 (1987)

[147] J. Abascal, C. Vega. A general purpose model for the condensed phases of water: TIP4P/2005. J. Chem. Phys. **123 (23)**, 234505 (2005)

[148] M. Mahoney, W. L. Jorgensen. A five-site model for liquid water and the reproduction of the density anomaly by rigid, nonpolarizable potential functions. J. Chem. Phys. **112 (20)**, 8910 (2000)

[149] H. L. Pi, J. L. Aragones, C. Vega, et al. Anomalies in water as obtained from computer simulations of the TIP4P/2005 model: density maxima, and density, isothermal compressibility and heat capacity minima. Mol. Phys. **107 (4-6)**, 365 (2009)

[150] J. R. Errington, A. Z. Panagiotopoulos. A fixed point charge model for water optimized to the vapor-liquid coexistence properties. J. Phys. Chem. B **102 (38)**, 7470 (1998)

[151] W. L. Jorgensen, J. D. Madura, C. J. Swenson. Optimized intermolecular potential functions for liquid hydropcarbons. J. Am. Chem. Soc. **106 (22)**, 6638 (1984)

[152] W. R. P. Scott, P. H. Hünenberger, I. G. Tironi, et al. The GROMOS Biomolecular Simulation Program Package. J. Phys. Chem. A **103 (19)**, 3596 (1999)

[153] B. Widom. Some topics in the theory of fluids. J. Chem. Phys. **39 (11)**, 2808 (1963)

[154] P. Sindzingre, G. Ciccotti, C. Massobrio, et al. Partial enthalpies and related quantities in mixtures from computer simulations. Chem. Phys. Lett. **136 (1)**, 35 (1987)

[155] M. R. Shirts, J. W. Pitera, W. C. Swope, et al. Extremely precise free energy calculations of amino acid side chain analogs: Comparison of common molecular mechanics force fields for proteins. J. Chem. Phys. **119 (11)**, 5740 (2003)

[156] T. C. Beutler, A. E. Mark, R. C. Vanschaik, et al. Avoiding singularities and numerical instabilities in free energy calculations based on molecular simulations. Chem. Phys. Lett. **222 (6)**, 529 (1994)

[157] C. Angell, J. Shuppert, J. Tucker. Anomalous properties of supercooled water. Heat capacity, expansivity, and proton magnetic resonance chemical shift from 0° to -38°. J. Phys. Chem. **77 (26)**, 3092 (1973)

[158] A. Saul, W. Wagner. A Fundamental Equation for Water Covering the Range from the Melting Line to 1273 K at Pressures up to 25 000 MPa. J. Phys. Chem. Ref. Data **18 (4)**, 1537 (1989)

[159] R. Speedy, C. Angell. Isothermal compressibility of supercooled water and evidence for a thermodynamic singularity at -45° C. J. Chem. Phys. **65 (3)**, 851 (1976)

[160] P. Poole, F. Sciortino, U. Essmann, et al. Phase behaviour of metastable water. Nature **360 (6402)**, 324 (1992)

[161] R. Speedy. Stability-limit conjecture. An interpretation of the properties of water. J. Phys. Chem. **86 (6)**, 982 (1982)

[162] H. E. Stanley, J. Teixeira. Interpretation of the unusual behaviour of H_20 and D_20 at low temperatures: Tests of a percolation model. J. Chem. Phys. **73 (7)**, 3404 (1980)

[163] P. G. Debenedetti. Supercooled and glassy water. J. Phys. Condens. Matter **15 (45)**, 1669 (2003)

[164] S. Sastry, P. G. Debenedetti, F. Sciortino, et al. Singularity-free interpretation of the thermodynamics of supercooled water. Phys. Rev. E **53 (6)**, 6144 (1996)

[165] L. Bosio, J. Teixeira, H. E. Stanley. Enhanced Density Fluctuations in Supercooled H_2O, D_2O, and Ethanol-Water Solutions: Evidence from Small-Angle X-Ray Scattering. Phys. Rev. Lett. **46 (9)**, 597 (1981)

[166] J. R. Errington, P. G. Debenedetti, S. Torquato. Cooperative origin of low-density domains in liquid water. Phys. Rev. Lett. **89 (21)**, 215503 (2002)

[167] E. B. Moore, V. Molinero. Growing correlation length in supercooled water. J. Chem. Phys. **130 (24)**, 244505 (2009)

[168] M. Matsumoto. Why Does Water Expand When It Cools? Phys. Rev. Lett. **103 (1)**, 017801 (2009)

[169] V. Molinero, E. Moore. Water Modeled As an Intermediate Element between Carbon and Silicon. J. Phys. Chem. B **113 (13)**, 4008 (2009)

[170] P. Chau, A. Hardwick. A new order parameter for tetrahedral configurations. Mol. Phys. **93 (3)**, 511 (1998)

[171] P. Kumar, S. Buldyrev, H. Stanley. A tetrahedral entropy for water. Proc. Natl. Acad. Sci. U.S.A. **106 (52)**, 22130 (2009)

[172] L. Baez, P. Clancy. Existence of a density maximum in extended simple point charge water. J. Chem. Phys. **101 (11)**, 9837 (1994)

[173] N. Giovambattista, H. E. Stanley, F. Sciortino. Phase diagram of amorphous solid water: Low-density, high-density, and very-high-density amorphous ices. Phys. Rev. E **72 (3)**, 031510 (2005)

[174] I. Brovchenko, A. Geiger, A. Oleinikova. Liquid-liquid phase transitions in supercooled water studied by computer simulations of various water models. J. Chem. Phys. **123 (4)**, 044515 (2005)

[175] S. Harrington, P. H. Poole, F. Sciortino, et al. Equation of state of supercooled water simulated using the extended simple point charge intermolecular potential. J. Chem. Phys. **107 (18)**, 7443 (1997)

[176] M. Lísal, J. Kolafa, I. Nezbeda. An examination of the five-site potential (TIP5P) for water. J. Chem. Phys. **117 (19)**, 8892 (2002)

[177] L. Xu, P. Kumar, S. V. Buldyrev, et al. Relation between the Widom line and the dynamic crossover in systems with a liquid–liquid phase transition. Proc. Natl. Acad. Sci. U.S.A. **102 (46)**, 16558 (2005)

[178] W. L. Jorgensen, J. Chandrasekhar, J. D. Madura, et al. Comparison of simple potential functions for simulating liquid water. J. Chem. Phys. **79 (2)**, 926 (1983)

[179] J. Waser, V. Schomaker. The Fourier inversion of diffraction data. Rev. Mod. Phys. **25 (3)**, 671 (1953)

[180] J. P. Hansen, I. R. McDonald. *Theory of simple liquids*. 3rd edition (Academic Press, Amsterdam, 2006)

[181] J. M. Sorenson, G. Hura, R. M. Glaeser, et al. What can x-ray scattering tell us about the radial distribution functions of water? J. Chem. Phys. **113 (20)**, 9149 (2000)

[182] K. A. Motakabbir, M. L. Berkowitz. Isothermal compressibility of SPC/E water. J. Phys. Chem. **94 (21)**, 8359 (1990)

[183] G. Hura, J. M. Sorenson, R. M. Glaeser, et al. A high-quality x-ray scattering experiment on liquid water at ambient conditions. J. Chem. Phys. **113 (20)**, 9140 (2000)

[184] J. Wang, A. N. Tripathi, V. H. Smith. Chemical binding and electron correlation effects in x-ray and high energy electron scattering. J. Chem. Phys. **101 (6)**, 4842 (1994)

[185] A. Savitzky, M. Golay. Smoothing and differentiation of data by simplified least squares procedures. Anal. Chem. **36 (8)**, 1627 (1964)

[186] J. D. Weeks, D. Chandler, H. Andersen. Role of repulsive forces in determining the equilibrium structure of simple liquids. J. Chem. Phys. **54 (12)**, 5237 (1971)

[187] J. Buchner, T. Kiefhaber. *Protein Folding Handbook*. 1st edition (Wiley-VCH, Weinheim, 2005)

[188] C. Anfinsen. Principles that govern folding of protein chains. Science **181 (4096)**, 223 (1973)

[189] W. Kauzmann. Protein stabilization - thermodynamics of unfolding. Nature **325 (6107)**, 763 (1987)

[190] S. J. Gill, N. Nichols, I. Wadsö. Calorimetric determination of enthalpies of solution of slightly soluble liquids. II. Enthalpy of solution of some hydrocarbons in water and their use in establishing the temperature dependence of their solubilities. J. Chem. Thermodyn. **8 (5)**, 445 (1976)

[191] S. Dec, S. J. Gill. Heats of solution of gaseous hydrocarbons in water at 25° C. J. Solution Chem. **13 (1)**, 27 (1984)

[192] H. Naghibi, S. Dec, S. J. Gill. Heat of solution of methane in water from 0 to 50° C. J. Phys. Chem. **90 (19)**, 4621 (1986)

[193] H. Naghibi, S. Dec, S. J. Gill. Heats of solution of ethane and propane in water from 0 to 50° C. J. Phys. Chem. **91 (1)**, 245 (1987)

[194] H. Naghibi, D. Ownby, S. J. Gill. Enthalpies of solution of butanes in water from 5 to 45° C. J. Chem. Eng. Data **32 (4)**, 422 (1987)

[195] K. P. Murphy, S. J. Gill. Thermodynamics of dissolution of solid cyclic dipeptides containing hydrophobic side groups. J. Chem. Thermodyn. **21 (9)**, 903 (1989)

[196] K. P. Murphy. Hydration and convergence temoeratures - on the use and interpretation of correlation plots. Biophys. Chem. **51 (2-3)**, 311 (1994)

[197] A. Yang, K. A. Sharp, B. Honig. Analysis of the heat capacity dependence of protein folding. J. Mol. Biol. **227 (3)**, 889 (1992)

[198] L. Fu, E. Freire. On the origin of the enthalpy and entropy convergence temperatures in protein folding. Proc. Natl. Acad. Sci. U.S.A. **89 (19)**, 9335 (1992)

[199] B. Guillot, Y. Guissani. A computer simulation study of the temperature dependence of hydrophobic hydration. J. Chem. Phys. **99 (10)**, 8075 (1993)

[200] D. M. Huang, D. Chandler. Temperature and length scale dependence of hydrophobic effects and their possible implications for protein folding. Proc. Natl. Acad. Sci. U.S.A. **97 (15)**, 8324 (2000)

[201] S. Garde, H. S. Ashbaugh. Temperature dependence of hydrophobic hydration and entropy convergence in an isotropic model of water. J. Chem. Phys. **115 (2)**, 977 (2001)

[202] H. S. Ashbaugh, T. M. Truskett, P. G. Debenedetti. A simple molecular thermodynamic theory of hydrophobic hydration. J. Chem. Phys. **116 (7)**, 2907 (2002)

[203] D. M. Huang, D. Chandler. The Hydrophobic Effect and the Influence of Solute-Solvent Attractions. J. Phys. Chem. B **106 (8)**, 2047 (2002)

[204] G. Graziano, B. Lee. Entropy convergence in hydrophobic hydration: A scaled particle theory analysis. Biophys. Chem. **105 (2-3)**, 241 (2003)

[205] B. Widom, P. Bhimalapuram, K. Koga. The hydrophobic effect. Phys. Chem. Chem. Phys. **5 (15)**, 3085 (2003)

[206] D. Paschek. Temperature dependence of the hydrophobic hydration and interaction of simple solutes: An examination of five popular water models. J. Chem. Phys. **120 (14)**, 6674 (2004)

[207] G. Graziano. Entropy convergence in the hydration thermodynamics of n-alcohols. J. Phys. Chem. B **109 (24)**, 12160 (2005)

[208] H. S. Ashbaugh, N. J. Collett, H. W. Hatch, et al. Assessing the thermodynamic signatures of hydrophobic hydration for several common water models. J. Chem. Phys. **132 (12)**, 124504 (2010)

[209] W. Becktel, J. A. Schellman. Protein stability curves. Biopolymers **26 (11)**, 1859 (1987)

[210] J. Sturtevant. Heat capacity and entropy changes in processes involving proteins. Proc. Natl. Acad. Sci. U.S.A. **74 (6)**, 2236 (1977)

[211] K. P. Murphy, V. Bhakuni, D. Xie, et al. Molecular basis of co-operativity in protein folding. III. Structural identification of cooperative folding units and folding intermediates. J. Mol. Biol. **227 (1)**, 293 (1992)

[212] C. Chothia. Nature of accessible and buried surfaces in proteins. J. Mol. Biol. **105 (1)**, 1 (1976)

[213] S. J. Gill, I. Wadsö. Equation of state describing hydrophobic interactions. Proc. Natl. Acad. Sci. U.S.A. **73 (9)**, 2955 (1976)

[214] C. Hu, H. Kokubo, G. Lynch, et al. Backbone additivity in the transfer model of protein solvation. Protein Sci. **19 (5)**, 1011 (2010)

[215] E. Lemmon, M. McLinden, D. Friend. *NIST Chemistry WebBook, NIST Standard Reference Database Number 69* (Eds. P.J. Linstrom and W.G. Mallard, National Institute of Standards and Technology, Gaithersburg MD, 20899, http://webbook.nist.gov, 2010)

[216] A. J. Patel, P. Varilly, D. Chandler. Fluctuations of Water near Extended Hydrophobic and Hydrophilic Surfaces. J. Phys. Chem. B **114 (4)**, 1632 (2010)

[217] J. de Pablo, J. Prausnitz, H. Strauch, et al. Molecular simulation of water along the liquid–vapor coexistence curve from 25° C to the critical point. J. Chem. Phys. **93 (10)**, 7355 (1990)

[218] J. S. Rowlinson, B. Widom. *Molecular Theory of Capillarity*. 1st edition (Clarendon Press, Oxford, 1982)

[219] J. Dzubiella, J. Swanson, J. McCammon. Coupling hydrophobicity, dispersion, and electrostatics in continuum solvent models. Phys. Rev. Lett. **96 (8)**, 087802 (2006)

[220] J. Henderson. Statistical mechanics of fluids at spherical structureless walls. Mol. Phys. **50 (4)**, 741 (1983)

[221] A. Poniewierski, J. Stecki. Statistical mechanics of a fluid in contact with a curved wall. J. Chem. Phys. **106 (8)**, 3358 (1997)

[222] G. Graziano. Significance of the Tolman length at a molecular level. Chem. Phys. Lett. **497 (1-3)**, 33 (2010)

[223] M. Moody, P. Attard. Curvature dependent surface tension from a simulation of a cavity in a Lennard-Jones liquid close to coexistence. J. Chem. Phys. **115 (19)**, 8967 (2001)

[224] E. M. Blokhuis, J. Kuipers. On the determination of the structure and tension of the interface between a fluid and a curved hard wall. J. Chem. Phys. **126 (5)**, 054702 (2007)

[225] T. Yamamoto, S. Ohnishi. Molecular dynamics study on helium nanobubbles in water. Phys. Chem. Chem. Phys. **13 (36)**, 16142 (2011)

[226] A. E. van Giessen, E. M. Blokhuis. Determination of curvature corrections to the surface tension of a liquid-vapor interface through molecular dynamics simulations. J. Chem. Phys. **116 (1)**, 302 (2002)

[227] E. M. Blokhuis, D. H. Bedeaux. Derivation of microscopic expressions for the rigidity constants of a simple liquid-vapor interface. Physica A **184 (1-2)**, 42 (1992)

[228] M. Napiórkowski, S. Dietrich. Structure of the effective Hamiltonian for liquid-vapor interfaces. Phys. Rev. E **47 (3)**, 1836 (1993)

[229] D. Vaknin, W. Bu, J. Sung, et al. Thermally excited capillary waves at vapor/liquid interfaces of water-alcohol mixtures. J. Phys. Condens. Matter **21 (11)**, 115105 (2009)

[230] A. Braslau, M. Deutsch, P. Pershan, et al. Surface roughness of water measured by x-ray reflectivity. Phys. Rev. Lett. **54 (2)**, 114 (1985)

[231] A. Braslau, P. S. Pershan, G. Swislow, et al. Capillary waves on the surface of simple liquids measured by x-ray reflectivity. Phys. Rev. A **38 (5)**, 2457 (1988)

[232] D. K. Schwartz, M. L. Schlossman, E. H. Kawamoto, et al. Thermal diffuse x-ray-scattering studies of the water-vapor interface. Phys. Rev. A **41 (10)**, 5687 (1990)

[233] O. Shpyrko, M. Fukuto, P. S. Pershan, et al. Surface layering of liquids: The role of surface tension. Phys. Rev. B **69 (24)**, 245423 (2004)

[234] F. P. Buff, R. A. Lovett, F. H. Stillinger. Interfacial density profile for fluids in the critical region. Phys. Rev. Lett. **15 (15)**, 621 (1965)

[235] A. O. Parry, C. J. Boulter. Fluctuation theory for the wavevector expansion of the excess grand potential of a liquid-vapour interface and the theory of interfacial fluctuations. J. Phys. Condens. Matter **6 (36)**, 7199 (1994)

[236] R. L. C. Vink, J. Horbach, K. Binder. Capillary waves in a colloid-polymer interface. J. Chem. Phys. **122 (13)**, 134905 (2005)

[237] A. E. Ismail, G. S. Grest, M. J. Stevens. Capillary waves at the liquid-vapor interface and the surface tension of water. J. Chem. Phys. **125 (1)**, 014702 (2006)

[238] J. N. Israelachvili. *Intermolecular and Surface Forces*. 3rd edition (Academic Press, Oxford, 2011)

[239] H. Reiss, H. Frisch, E. Helfand, et al. Aspects of the statistical thermodynamics of real fluids. J. Chem. Phys. **32 (1)**, 119 (1960)

[240] P. Liu, E. Harder, B. Berne. On the calculation of diffusion coefficients in confined fluids and interfaces with an application to the liquid-vapor interface of water. J. Phys. Chem. B **108 (21)**, 6595 (2004)

[241] C. Wick, L. Dang. Diffusion at the liquid-vapor interface of an aqueous ionic solution utilizing a dual simulation technique. J. Phys. Chem. B **109 (32)**, 15574 (2005)

[242] I. Muegge, E. W. Knapp. Residence times and lateral diffusion of water at protein surfaces: application to BPTI. J. Phys. Chem. **99 (5)**, 1371 (1995)

[243] E. W. Knapp, I. Muegge. Heterogeneous diffusion of water at protein surfaces: application to BPTI. J. Phys. Chem. **97 (43)**, 11339 (1993)

[244] S. Yang, J. N. Onuchic, A. E. Garcia, et al. Folding time predictions from all-atom replica exchange simulations. J. Mol. Biol. **372 (3)**, 756 (2007)

[245] R. B. Best, G. Hummer. Coordinate-dependent diffusion in protein folding. Proc. Natl. Acad. Sci. U.S.A. **107 (3)**, 1088 (2010)

[246] M. Hinczewski, Y. von Hansen, J. Dzubiella, et al. How the diffusivity profile reduces the arbitrariness of protein folding free energies. J. Chem. Phys. **132 (24)**, 245103 (2010)

[247] Y. von Hansen, I. Kalcher, J. Dzubiella. Ion Specificity in α-Helical Folding Kinetics. J. Phys. Chem. B **114 (43)**, 13815 (2010)

[248] G. Weiss. First passage time problems in chemical physics. Adv. Chem. Phys. **13**, 1 (1967)

[249] J. Feng, K.-Y. Wong, K. Dyer, et al. Transport properties of water at functionalized molecular interfaces. J. Chem. Phys. **131 (12)**, 125102 (2009)

[250] P. Fehder, C. Emeis, R. Futrelle. Microscopic mechanism for self-diffusion and relative diffusion in simple liquids. J. Chem. Phys. **54 (11)**, 4921 (1971)

[251] C. Emeis, P. Fehder. The microscopic mechanism for diffusion and the rates of diffusion-controlled reactions in simple liquid solvents. J. Am. Chem. Soc. **92 (8)**, 2246 (1970)

[252] M. Cacace, E. Landau, J. Ramsden. The Hofmeister series: salt and solvent effects on interfacial phenomena. Q. Rev. Biophys. **30 (3)**, 241 (1997)

[253] A. Omta, M. Kropman, S. Woutersen, et al. Negligible effect of ions on the hydrogen-bond structure in liquid water. Science **301 (5631)**, 347 (2003)

[254] K. Collins. Ions from the Hofmeister series and osmolytes: effects on proteins in solution and in the crystallization process. Methods **34 (3)**, 300 (2004)

[255] H. Frank, F. Franks. Structural approach to the solvent power of water for hydrocarbons; urea as a structure breaker. J. Chem. Phys. **48 (10)**, 4746 (1968)

[256] D. Horinek, R. R. Netz. Can Simulations Quantitatively Predict Peptide Transfer Free Energies to Urea Solutions? Thermodynamic Concepts and Force Field Limitations. J. Phys. Chem. A **115**, 6125 (2011)

[257] Y. Wu, H. L. Tepper, G. A. Voth. Flexible simple point-charge water model with improved liquid-state properties. J. Chem. Phys. **124 (2)**, 024503 (2006)